UNIVERSITAT DE
BARCELONA

Kesterite Deposited by Spray Pyrolysis for Solar Cell Applications

Moises Espindola Rodriguez

KESTERITE DEPOSITED BY SPRAY PYROLYSIS FOR SOLAR CELL APPLICATIONS

Presented by

Espindola Rodriguez, Moises

Thesis supervisors:

Dr. Edgardo Saucedo Silva

Prof. Dr. Osvaldo Vigil Galán

Thesis tutor:

Prof. Dr. Alejandro Pérez Rodríguez

Thesis submitted May 2015 in completion of the requirements for the
Doctor of Philosophy in Engineering and Advanced Technologies

University of Barcelona
Faculty of Physics, Department of Electronics

Espindola Rodriguez, Moises

CONTENTS

ABSTRACT

Solar cells generate electrical power by direct conversion of solar radiation into electricity using semiconductors. Once produced, the solar cells do not require the use of water; operate in silence and can be easily installed almost everywhere, as solar panels with low technological risk. In this thesis new photovoltaic materials and solar cells are investigated.

From the beginning of the semiconductor era, silicon has been present; the semiconductor theory improved with the silicon technology, almost taking the idealized models to reality in within silicon. In the recent years plenty of new natural and artificially produced materials have seen the light; some of them are still waiting to be understood and explained by a new theory that has to be experimentally proved right. The clue for a better and faster progress is to work in a multidisciplinary frame; as this thesis shows, all research and knowledge has to have future protections and possibilities of been used in the benefit of our society.

Today, the photovoltaic technology (PV) based on silicon solar cells dominates the market. The thin film PV such as GaAs, $Cu(In,Ga)Se_2$ (CIGS) and CdTe have reached power conversion efficiencies above 20% which makes them industrially interesting despite the use of scare and/or very toxic elements. Researchers and investors are expectant for a new stable, eco-friendly, inexpensive, fast and easy to produce material that could be used in a big scale and long term for photovoltaic terrestrial applications.

Some years ago it was believed that this ideal material was near to be confirmed when the reflectors were on a new chalcogenide material: $Cu_2ZnSn(S_xSe_{1-x})_4$ (CZTSSe) called kesterite after its crystal structure. This semiconductor is very attractive due to its constituent elements, semiconductor properties. Its similarity with CIGS and compatibility with the already existing industrial processes made possible its rapid power conversion efficiency rise as absorber material in thin film solar cells. Through the years kesterite has been found to be a challenging material due to the energetically feasible mixture of stannite and kesterite structures, the high probability of defects, and the narrowness of the optimum compositional region (compared with that of chalcopyrites) that eases the formation of secondary phases limiting the efficiency of the solar cells.

Recently, CZTSSe thin film solar cells with certified efficiency of 12.6% were produced by IBM; synthesized by spin-coating using a hydrazine-based pure solution approach on a soda-lime glass (SLG) Mo coated substrate. The use of hydrazine is the key for the record as well its mayor drawback however it demonstrates the robustness of the solution-based techniques.

In this thesis the use of a *cool-wall vertical pneumatic spray pyrolysis system* (SP) is demonstrated as a synthesis technique of CZTS kesterite thin films from water and alcohol-based precursor solutions containing metal salts and thiourea. In the course of this thesis, the possibilities and limitations of this synthesis technique and the resulting films are explored in the frame of system- and solution-related parameters.

The SP system used in this thesis is sophisticate and advantageous; is able of reproduce the open-air conditions used in typical spray systems but also it is capable of grow films by spraying in an oxygen-free atmospheres such as Ar or $Ar-H_2$ or any other. It was completely new spray approach by the year of the publication of our first repot (2013)

with a 0.5% efficient working solar cell. A remarkable efficiency value by the time of publication if considered the combo challenge: material + deposition technique.

In this thesis, air, Ar and Ar-H_2 were used as carrier gas and atmosphere, where the so sprayed films were studied in combination with other system parameters (solution flux, time of spraying, substrate temperature, etc.) and some solution related parameters (solvent, metal precursors concentration, solution stability, etc.).

To obtain device grade films, the sprayed kesterite ought to be annealed; this annealing process is also subject of study in this thesis. One step annealing at high temperature (580°C) at room pressure in S-containing reactive atmosphere was optimized for the CZTS-based thin films with efficiencies of 1.4%. To synthesize CZTSSe films, different annealing approaches were tried; one step room pressure annealing (at 550°C) in Se-containing reactive atmosphere probed to be the optimum for sprayed kesterite from methanol-based precursor solutions for solar cells with the highest conversion efficiency of 1.9% obtained in this thesis. The results showed here open many new possibilities for the use of spray systems for the synthesis of PV quality materials for solar cells applications.

Espindola Rodriguez, Moises

RESUMEN

Las células solares generan energía eléctrica mediante la conversión directa de la radiación solar en electricidad utilizando semiconductores. Las células solares, una vez producidas, no requieren el uso de agua de refrigeración; operan en silencio y puede ser fácilmente instaladas en casi cualquier ambiente, en forma de paneles solares los cuales posen un bajo riesgo tecnológico. En esta tesis se investigan nuevos materiales fotovoltaicos basados en elementos abundantes en la corteza terrestre y las células solares producidas a partir de ellos.

Desde el comienzo de la era de los semiconductores el silicio ha sido el material de referencia; los grandes avances en la tecnología del silicio han contribuido al refinamiento de la teoría de los semiconductores al ser uno de los pocos materiales que en la realidad se aproximan a los modelos teóricos.

En los últimos años muchos nuevos materiales natural y artificialmente producidos han sido reportados; algunos de ellos todavía están a la espera de ser comprendidos y explicados por alguna nueva teoría que ha de ser verificada experimentalmente. La clave para progreso más rápido y significativo es trabajar en un marco multidisciplinario; como esta tesis muestra, la investigación y el conocimiento han de tener proyección de ser aplicadas en beneficio de nuestra sociedad.

Hoy en día, la tecnología fotovoltaica basada en el silicio domina el mercado. Sin embargo, tecnologías fotovoltaicas de película delgada como GaAs, $Cu(In,Ga)Se_2$ (CIGS) y CdTe han alcanzado eficiencias de conversión por encima del 20%, lo que las hace industrialmente interesantes a pesar de estar constituidas por elementos escasos y/o tóxicos. Por esta razón, los investigadores y los inversores están expectantes por la aparición de nuevos materiales que sean estables, respetuosos con el medio ambiente; cuya producción sea barata, rápida y fácil. Éstos materiales han de poder ser utilizados a gran escala y largo plazo en aplicaciones fotovoltaicas a gran escala.

Hace unos años se creía que el material idóneo estaba a punto de ser confirmado cuando una gran parte de la comunidad científica enfocó su atención en una nueva familia de calcogenuros: $Cu_2ZnSn(S_xSe_{1-x})_4$ (CZTSSe) llamada kesterita por su estructura cristalina. Estos semiconductores son tecnológicamente atractivos debido a la abundancia y baja toxicidad de sus elementos constitutivos. Su similitud con el CIGS y su compatibilidad con los procesos industriales ya existentes hicieron posible el rápido incremento de su eficiencia de conversión en células solares de películas delgadas; desde su aparición las kesteritas han demostrado ser un material con muchos retos tecnológicos, científicos y conceptuales.

Recientemente, IBM reporté células solares de película delgada basadas en CZTSSe con eficiencia certificada del 12.6%; la mayor eficiencia reportada hasta el momento. Estas células fueron producidas por spin-coating sobre substratos de vidrio (SLG) recubiertos de Mo; el uso de hidracina es la clave de esta eficiencia pero a su vez su mayor desventaja. Este sobresaliente resultado que no ha podido ser superado todavía, demuestra lo prometedoras que son las técnicas basadas en solución.

En esta tesis se demuestra el uso de un sistema de *spray pyrolysis* que es neumático vertical con paredes frías, utilizado para sintetizar kesterita de azufre puro (CZTS) a partir de soluciones a base de agua y alcohol, que contienen sales de metales y tiourea en

solución. Se exploran las posibilidades y limitaciones de este sistema como técnica de síntesis en el marco de los parámetros del sistema y de la solución.

El sistema de spray utilizado en esta tesis es sofisticado y presenta numerosas ventajas siendo la más importante de ellas que, en este sistema, es posible depositar películas de CZTS en atmosfera controlada de Ar, Ar-H_2 o de cualquier otro gas. Además, es posible utilizar condiciones de depósito que pueden ser consideradas como tradicionales utilizando aire como gas transportador en atmósfera de aire. La posibilidad de depositar por spray películas delgadas en atmósfera controlada era un concepto totalmente nuevo a la fecha de la publicación del primer reporte de esta tesis (2013), donde se reportaron unas de las primeras celdas solares con 0.5% de eficiencia de conversión obtenidas por ésta técnica. Un valor nada despreciable al tener en cuenta la complejidad del material y de la técnica de depósito.

En esta tesis, se estudiaron las propiedades de las películas en función de distintos parámetros del sistema (gas transportador, flujo de la solución, tiempo de depósito, temperatura del sustrato, etc.) y de la solución (solvente, concentración de precursores, estabilidad de la solución, etc.).

Para obtener películas que puedan ser usadas como capa absorbedora en dispositivos fotovoltaicos, las películas fueron sometidas a un tratamiento térmico, el cual también se estudia en esta tesis. La sulfurización de las películas en atmosfera reactiva de S permitió obtener CZTS de alta calidad en términos de cristalinidad y resistividad lo que condujo a eficiencias de conversión de 1.4%. Por otro lado para la síntesis de las películas de CZTSSe, se estudiaron selenizaciones en uno y dos pasos en atmosfera reactiva de Se. Las películas obtenidas a partir de soluciones basadas en metanol posteriormente selenizadas a 550°C condujeron a la eficiencia más prometedora reportada en esta tesis con 1.9%. Los resultados presentados aquí demuestran las posibilidades en el uso de sistemas de spray para la síntesis de materiales con aplicaciones fotovoltaicas.

Espindola Rodriguez, Moises

LIST OF TABLES

LIST OF FIGURES

Espindola Rodriguez, Moises

1 INTRODUCTION

Solar energy is the most abundant, direct, accessible and free source of energy. The rate at which solar energy is intercepted by the Earth is about 10,000 times greater than the rate at which humankind consumes energy. Even if not all countries are equally endowed with solar energy there are many different solar technologies that can be used almost everywhere on Earth to act as energy supply.

The generation of electricity using photovoltaic (PV) panels is nowadays a worldwide phenomenon; it is a technology used to directly convert solar radiation (visible light) into electricity. Assisted by supporting pricing policies, the annual grow rate for PV production in the last decade, was more than 50% making it one of the most fastest-growing energy technologies in percentage terms[1]. Some photovoltaic technologies are already competitive with market prices and in general their overall viability is improving; nevertheless, there is still room for novel materials, technology and visionary technologists.

The production of solar cells with reduced cost, high efficiency and environmental friendly processes is the current challenge for terrestrial PV. The most efficient thin film solar cells are based on amorphous silicon (a-Si), cadmium telluride (CdTe) and copper indium gallium selenide (CIS/CIGS) known as second generation polycrystalline thin films. In the last years, new materials with properties of interest for photovoltaic applications and formed by non toxic and relatively abundant elements, have been suggested as an alternative to the main second generation solar cell technologies. Semiconductor compounds with kesterite structure such as $Cu_2ZnSn(S_xSe_{1-x})_4$, $0 \leq x \leq 1$ (CZTSSe) have been proposed as new candidates for thin film solar cells. However, reported solar cell efficiencies for kesterite have not yet reached the expected industrial attractive value ($\eta > 15\%$).

In this chapter, we present a review of some of the limiting factors for achieving high photovoltaic conversion efficiency in kesterite thin film solar cells. Also here is presented the state of the art of the different deposition methods and their efficiencies.

1. Introduction

Solar cells are usually divided in to tree categories called generations; the different cells in each generation share some physical properties and production costs. The first generation of solar cells is composed by p-n homo-junctions devices that are relatively expensive to produce due to both, the high material usage (>180μm) and the need of defect-free materials (Si, Ge). Defect free materials are needed in indirect transition semiconductors to decrease the probability of recombination before carrier collection.

The second generation solar cells are cheaper to produce as they are made of direct transition semiconductors with high absorption coefficient requiring only some micrometers (<2μm) to absorb the visible part of the electromagnetic spectrum. They are usually formed by hetero-junctions of polycrystalline films with high flexibility in module fabrication, some challenges of this technology are related with the grain and inter grain recombination, homogeneous composition and thickness and the typically non ideal p-n junction formation.

Most of the cells in the third generation are still not commercial; they include non-semiconductor technologies (polymers and biomimetics), quantum dot, tandem/multi-junction cells, intermediate band solar cell, hot-carrier cells, photon up-conversion and down-conversion technologies, and solar thermal technologies. Duet to conceptual differences they are able to overcome the Shockley–Queisser limit[2] for single bandgap solar cells.

1.1 Second generation solar cells: Chalcogenides

As was mentioned, the most efficient second generation thin film solar cells are based on a-Si, CdTe and CIS/CIGS. The challenge of these materials is to reduce the cost per watt of solar energy conversion, but they are actually formed by expensive and/or scanty elements in the earth's crust such as In, Ga, Te and other that present toxicity issues like Cd. Specifically, the price of In has increased in the last few years because of its use by the fast-growing flat panel display industry; it could lead to a sever cost pressure that could increase the cost per watt. Among proposed substitute compounds for use in second generation solar cells, CZTSSe is considered the most promising semiconductor for future development.

In order to obtain an efficient solar cell two conditions related to the light absorbers must be taken into account:

i.   Effective absorption of incident photons to generate electron–hole pairs

ii.   Ability to collect the photo-generated charges before they recombine

Theoretical considerations predict maximum power conversion efficiency[2] in the 20–30 % range for absorber materials with a band gap between 1 and 2 eV (optimal overlap with the solar spectrum should occur for a band gap of 1.5 eV). A direct band gap also provides a large absorption coefficient (>10^4cm^{-1}) for photons with energy greater than the band gap energy. A direct band gap thereby allows effective absorption (higher than 80%) in a layer thinner than few microns, thus reducing significantly the materials need in comparison with indirect bandgap materials such as crystalline silicon (first generation).

On the other hand, from the electrical point of view, the absorber should be of p-type conductivity to ensure a greater diffusion length of the minority carriers (electrons) to the space charge region. The light absorber semiconductor CZTSSe mentioned above meet all these optical and electrical properties. At the same time, the named buffer layers (n-type), should have a band gap energy high enough to permit transmission of photons towards the absorber, increasing therefore the spectral response of solar cell in the ultraviolet region.

There are other aspects to take into account when solar cells are based on hetero-junction devices. The involved materials must have good lattice and dielectric constant coupling. The thermal expansion coefficients must be as close as possible to prevent breakage due to temperature increase under solar irradiation. Furthermore, band discontinuities between absorber and buffer materials are one of the biggest problems to be solved. Achieving all of these conditions in a device is a current challenge. As a trend, the majority of CZTSSe-based solar cells have been processed with CdS as buffer layer and Mo as back contact, which has been directly transferred from CIGS technology.

1.2 Kesterite-based solar cells

In the last years substantial increases in CZTSSe device performance improvements have been reported. It was in August 2011when CZTSSe was first considered among the *top ten notable exceptions* solar cells[3] with a efficiency of 9.7%[4] by IBM as a result of intense research, not only in the world record holder laboratory but all around the globe. Then, in January 2013, the same group improved the efficiency of the CZTSSe-based devices to 11.1%[5]; at the same time, the pure sulfur kesterite absorber, CZTS was first included among the top ten notable exceptions solar cells[6] with a efficiency of 8.4%[7]. After two years, by January 2015, the pure sulfur kesterite record device was slightly improved to 8.5%[8]; it reveals the complexity of the pure sulfur kesterite-based devices.

By May 2014, the Watson Research Center (IBM), showed the *actual* world record[8] for CZTSSe-based solar cells with η = 12.6%[9], Voc = 513.4mV, Jsc = 35.2mA/cm^2, FF = 69.8%, Rs = 0.72Ω·cm^2 and Eg = 1.13eV, achieved via a hydrazine slurry approach; hydrazine is a toxic and explosive solvent that must be handled using the appropriate protective equipment to prevent physical contact with either vapor or liquid. Those world records as well as the day-by-day improvements of each laboratory and researcher are encouraging to continue working hard on this challenging material.

In this section some of the main aspects influencing the efficiency and physical properties of the kesterite-based devices are discussed, going from the fundamental properties of kesterite materials to the aspects related with efficiency improvements.

1.2.1 Fundamental properties

The kesterite type sulfur-selenium alloy CZTSSe semiconductor belongs to the I_2-II-IV-VI_4 compounds. As for the chalcopyrite type compounds, the mineral, where the structure type was determined first, gives the name of the structure[10]. kesterite can be obtained from the chalcopyrite structure by replacing In in the $CuIn(S,Se)_2$ with Zn and Sn. The crystal structures are therefore very closely related, which raises the hope that the excellent optoelectronic properties of the Cu chalcopyrites can also be achieved for this

material[11]. Replacing In and Ga in Cu(In,Ga)Se$_2$ by the earth-abundant elements Sn and Zn would allow for a sustainable deployment of this technology on the terawatt scale.

The kesterite type structure (Figure 1 Cu (orange), Sn (blue), Zn/Fe (grey), S (yellow). American Mineralogist crystal structure database.) is characterized by alternating cation layers of CuSn, CuZn, CuSn and CuZn at z = 0, 1/4, 1/2 and 3/4, respectively. Thus one copper occupies the 2a (0,0,0) position with zinc and the remaining copper ordered at 2c (0,1/2,1/4) and 2d (0,1/2,3/4) resulting in the space group $I\bar{4}$ [10]. From that, CZTS and CZTSe crystallizes in kesterite type structure, where the identified intrinsic point defects are Cu_{Zn} and Zn_{Cu} anti-sites, occurring in the Cu_{Zn} (0 0 1) planes at z = 1/4 and 3/4. Moreover the defect concentration depends on the starting composition and the cooling rate after sample synthesis[10]. This disorder may be explained by a co-existence of kesterite and Stannite. However, the energy difference of the Stannite structure is only slightly larger, and since the band gaps predicted for the Stannite are smaller than those of the kesterite, a co-existence of both structures could lead to the relatively low open-circuit voltages observed in kesterite solar cells as compared to the band gap[12].
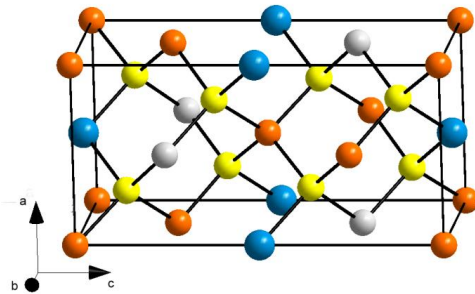
Figure 1. Kesterite structure.

Regarding defect formation energies, which depend on composition and on the Fermi level, some clear trends are observed[13]: The defect with the lowest formation energy is the acceptor Cu_{Zn} defect. Further low energy formation acceptors are Cu_{Sn} as well as V_{Cu}. Donor defect levels such as V_S or Zn_{Cu} in general show higher formation energies, which in combination with the low, often even negative formation energy of Cu_{Zn} explains that CZTS and CZTSe so far have always found being p-type.

The band gap is experimentally determined by optical transmission measurements or by quantum efficiency measurements in solar cells. The variation of the sulfur-selenium content on the solid solution $Cu_2ZnSn(S_xSe_{1-x})_4$, is responsible of the energy band gap of the resulting material; it is 1.5eV for x = 1 (CZTS) and goes down to 1eV for x = 0 (CZTSe)[14].

On phase diagrams there exists only a small region of single phase kesterite allowing 1-2% (absolute) deviation in the composition at temperatures around 550°C, which is significantly less than in the case of chalcopyrites allowing Cu deficiency of 4% (absolute)[13]. In addition, the high-efficiency solar cells always have a Cu-poor, Zn-rich, and slightly Sn-poor composition[15]; it makes of the kesterite-based solar cells a very complex technology.

1.2.2 Low diffusion length

Kesterite compounds are characterized by low minority carrier lifetimes (<2.5ns). This implies low diffusion length and mobility values; while for CIGS thin film solar cells life times as long as 250ns have been reported[16]. Low diffusion length values determine low values of Voc and low fill factor. Improvement of the morphological properties and the crystalline quality of the films involved in the solar cells are some aspects to be taken into account for improving the charge carrier transport parameters. Longer minority carrier lifetimes is attributed to low band gap energy materials, such as CZTSe, than in high band gap devices like CZTS[12]. The compositional homogeneity and phase purity in the absorber need to be more finely controlled in order to further increase power conversion efficiency, since even the CZTSSe films used in relatively high efficiency devices exhibit low (a few ns) lifetimes[12, 17] which reflect complex carrier dynamics.

1.2.3 Grain boundaries transport

Grain boundaries are Cu-rich[18], which increases the recombination rates. Cu-rich absorbers were found to have lower Voc than Cu-poor ones, probably in relationship with Cu_2X formation. The difference between Eg in [eV] and Voc in [V], called Voc deficit, is smaller in lower band gap energy materials (near to Se-pure absorbers) and KCN etched absorbers as this etching removes the Cu-related phases. Interesting results show that HCl-based etch is effective for the selective removal of superficial Zn-rich secondary phases. Etching processes with HCl have a significant impact on the optoelectronic parameters of the solar cells. This markedly influences the Jsc and Rs parameters and, consequently, the conversion efficiency of the devices[19]. Furthermore, HCl can potentially replace KCN etching which is not industrial compatible.

Experimental evidence was given to support efficient removal of the ZnSe secondary phase located at the surface of Zn-rich and Cu-poor CZTSe absorbers[20]. An oxidizing route, $KMnO_4$ in H_2SO_4, was selected among different oxidizing agents as the most effective route to remove this phase, which is detrimental for solar cell performance. In addition to this oxidizing step, a Na_2S etching step was also necessary to remove elemental Se resulting from the oxidation of ZnSe. Solar cells with two different kinds of absorbers (highly Zn rich and slightly Zn rich) were produced using etched and non etched CZTSe samples. I–V curves showed that efficiency was considerably improved owing to a major increase in Voc, up to 100mV, for the most Zn-rich sample. Chemical passivation on the CZTSe absorber surface was considered as additional effect of this etching.

1.2.4 Composition and secondary phases

The formation of secondary phases should be avoided; the atoms within the kesterite crystal structure should ideally take the positions shown in Figure 1; due to the CZTSSe complexity and the number of elements it is not surprising the co-existence of multiple secondary phases due to the complexity of chemical potentials[21].

As mentioned earlier, high power conversion efficiency is achieved in a relatively narrow range of composition[4, 22] Cu/(Zn+Sn) = 0.8, Zn/Sn = 1.22 and Cu/Sn = 1.6. Under this conditions (Cu-poor, Zn-rich), Zn(S,Se) is the most likely secondary phase (as the Zn chemical potential lies in a extremely narrow range[21]) and is responsible of the high series

resistance of the devices, acting as insulators with band gap energies of[22] 3.7eV and 2.7eV for ZnS and ZnSe respectively. Its superficial removal by wet chemical etching (as previously mentioned) is possible however, its existence below the absorber's surface has been probed[18, 23], and is related with the deposition technique and thermal annealing profiles. This secondary phase can reduce the area where electro-hole pairs are formed and inhibit current conduction. In some cases it forms a front contact barrier with ZnO: Al/ZnO. CuS and $Cu_{1.8}S$ behave as metal creating a short circuit between the front and rear contacts of the solar cells while Cu_2SnS_3 compound presents metallic properties.

Physical vacuum deposition techniques can produce absorbers in the relatively narrow range of the compositional phase diagram closest to the optimal ones than those obtained by chemical routes.

1.2.5 Buffer/kesterite interface

Recently, observed differences in the recombination path between pure selenide absorbers and S-containing ones strongly supports a cliff at the interface of sulfur containing absorbers (CZTSSe) and a spike at the interface of pure selenide absorbers (CZTSe) showing that CdS is a suitable buffer for pure selenide kesterite, but not the ideal choice for CZTSSe[22]. This non-ideal recombination is caused by an extremely high density of defect states; in general, the relative low efficiency values could be attributed to both, kesterite bulk recombination and buffer/kesterite interface problems, where the interface recombination is the main loss mechanism.

It makes clear the importance of developing an optimized deposition process for the CdS buffer layer for high performance CZTSe kesterite solar cells as reported by IREC[24]. This optimization was on the direction of changing the cadmium precursor source from sulfate to nitrate salts; it reduces the deep level acceptor-like traps states inside the CdS layer, which are responsible for an increase of the conduction band spike up to a current blocking value (for the sulfate precursor case). Understanding the origins of this current and FF-limiting JV curve distortions opens new perspectives for optimizing solar cell performance. A slower growth process (nitrate approach, >30min) definitely reduces the amount of light-sensitive defects resulting in an elimination of crossover, red kink and a reduction of series resistance, which is considered as one of the main efficiency-limiting problems in kesterite-based solar cells along with the Voc deficit. It was also found that light soaking can temporarily improve device performance (up to 8.2%) by neutralizing interface defects in the buffer layer by photo-generated holes leading to a reduction of series resistance and improved FF.

1.2.6 Back-contact in kesterite

The kesterite-based solar cells had developed so fast because they use almost the same process and knowledge that the CIGS technology; both solar cells technologies are conceptually the same but experimentally they have remarkable differences.

As CIGS precursor layers are normally deposited directly onto Mo-coated glass substrates, researchers from the beginning, started doing the same, using Mo as back contact[25]. However it has been demonstrated[26], from thermodynamic analysis that chemically, the kesterite/Mo interface is not as stable as the CIGS/Mo interface. In the kesterite case, the

back contact plays a much more active role than in the case of CIGS, in part due to the narrow stable region of kesterite but also for the unstable interface between CZTSSe and Mo. During the thermal annealing of kesterite, the back contact has an important role in the film growth process and influences directly the resulting bulk properties, including the formation of interfacial voids[27], potentially resistive secondary phases[26] and intermediate $Mo(S,Se)_2$ layers[28, 29].

The decomposition of kesterite (phase segregation) into low band gap compounds near the Mo at high temperature[27] (~540°C) occurs because of the concentration of a particular crystal defect has exceeded its solubility limit in the single phase, this reaction can be lowered using high chalcogen partial vapor pressures but as side effect, thick $Mo(S,Se)_2$ are formed; a balance should be found because if the $Mo(S,Se)_2$ layers are too thick, they are also detrimental. Thick MoS_2 (~100nm) and $MoSe_2$ (~1µm) layers are observed in kesterite-based devices, the thickness of this interfacial layers have a reverse correlation with device performance reducing the Voc and increasing the series resistance[28]. On the other hand, the world record CZTSSe cells[9, 30] exhibit low series resistance in the range of 0.40–0.72 $\Omega \cdot cm^2$; it relieves the earlier concerns that Mo might always form a blocking contact with the absorber without been the optimum.

Several studies have observed secondary phases, such as ZnS or Cu_2SnS_3, at the back contact[26, 27, 31], which may have implications for device resistance, film growth, and device stability. It is unclear if the elevated series resistance (>3$\Omega \cdot cm^2$) observed in CZTS devices[7, 12, 29] is related to the MoS_2 at the back contact or the bulk. In the direction of controlling the formation of MoS_2, the use of a thin layer (10-70nm) of TiB_2 sputtered intermediate layer between absorber and Mo back contact has been tested[32]. This approach reduces the series resistance and thereby increases the device efficiency by increasing the short current density (Jsc) and fill factor boost. However, it was shown that introducing TiB_2 degrades the crystal quality of absorber, which is detrimental to device performance especially Voc. This intermediate layer only increases solar cell performance from 3.0% (0nm) to 4.40 % (30nm).

To limit the thickness of the $MoSe_2$, diffusion barriers had been used, such as TiN diffusion barrier that showed to limit $MoSe_2$ growth to ~200nm under normal processing conditions and significantly improve lifetime (>9ns) and device performance until 8.9%[28]. Before the general experimental agreement that Mo is not stable at the interface with the kesterite absorber, various metals (Au, W, Pd, Pt, and Ni) deposited in the top of Mo were tested as back contact[33]. It was demonstrated that it is possible to synthesize device-quality CZTSSe thin films on W, Au, and Pt back contacts. It was shown that W and Au back contacts allow enhancing the photo generatedcurrent, but that Mo remains the best back contact in terms of power conversion efficiency.

Regarding the formation of $MoSe_2$ in pure-selenium kesterite devices, we reported a process based on the use of a thin (10-20nm) ZnO intermediate layer[34] between the Mo back contact and the absorber. In that work it was experimentally confirmed that CZTSe decomposes inevitably in contact with Mo during the annealing or cooling process. It was found that the inclusion of intermediate ZnO nanolayer leads to an significant inhibition of the decomposition reaction[26], allowing the formation of higher quality absorber/back contact interfaces. The presence of this ZnO nanolayer prevents direct contact between Mo and CZTSe, and inhibits absorber's decomposition. The device with the thinner ZnO layer

(10nm) exhibited 6.0% efficiency (the highest in the report), while the reference cell (without ZnO) only yielded 2.5% of efficiency. The fall in the value of efficiency when the thickness of the ZnO was increased is presumably due to series resistance effects and Zn-related compounds.

Despite Mo has been widely used as a standard back contact material in kesterite devices it should be urgently reexamined as suggested by the above researchers; a detailed study of alternative metals to be used as back contact in CZTS, CZTSe and CZTSSe is still waiting to be done.

1.2.7 Aspects related to the improvement of solar cell efficiency

There are several difficulties in the kesterite solar cells that need to be overcome in order to reach high efficiencies. This section is indented to review the main problems in the materials and devices showing at the same time the state of the art of the different published approaches to solve them.

Reverse saturation current in kesterite-based devices is[35, 36] $\sim 10^{-6}$ to 10^{-3} mA/cm^{-2}. This is orders of magnitude higher than that seen in high-quality CIGS ($\sim 10^{-8}$ mA/cm^2). Aside from this, diode quality factors for CZTSSe devices are 1.3-2, indicating substantial recombination in the space charge region. Short-circuit current collection in CZTSSe devices is on par with that achieved in CIGS devices, which along with the high observed reverse saturation current is consistent with losses primarily due to recombination[37]. The defects responsible for Voc loss in CZTSSe devices likely include deep recombination centers in the bulk material and recombination centers at interfaces and grain boundaries. The limited Voc in CZTSSe devices is likely due primarily to the activity of defects and the resulting increased reverse saturation current. Thus, future progress in CZTSSe solar cells will likely rely on understanding the defects that lower Voc relative to its ideal value[36] and the nature of defects near the CZTSSe/CdS heterojunction.

In addition to high-quality material, CZTSSe cells must have optimized window and back-contact interfaces to minimize recombination, resistive losses, and parasitic absorption. While the optimized CdS buffer (as discussed earlier) may be adequate to address some of the most urgent absorber development needs, moving to higher band-gaps and improved light transmission will require buffer development similar to that being carried out for CIGSSe devices. In addition to determining and optimizing the interfacial band offset, understanding band bending, interfacial defect concentration, inter-diffusion and stability among other properties is necessary to maximize depletion and minimize recombination.

There are other interconnected factors that must be analyzed:

First, low values of absorber's resistivity ($\rho_{absorber}$) are generally reported. If p–n junction behavior is assumed, low values of this parameter (as compared to ones of n-type semiconductor partners) imply that the space charge region in the heterojunction is displaced to the n-type material. This displacement is dependent on the $\rho_{buffer}/\rho_{absorber}$ ratio. So, the hypothesis of the Metal–Insulator-Semiconductor (MIS) structure may be more appropriate, taking into account the following considerations:

i. The buffer can be considered as an insulator between the TCO that behaves like metal and the p-type semiconductor

ii. The depletion region and the absorption length in the absorber are similar (about 1μm). Thus, the predominant transport mechanism is the drift of the charges due to the field, instead of the diffusion mechanism of a p–n junction.

Consistent with the MIS model is the use of a resistive buffer; this corresponds to the best results reported of kesterite solar cells using CdS as buffer layer with thicknesses below of 60nm[24]. The appropriate dopant atoms could increase the resistivity of the buffer and can be a useful procedure for improving the solar cells optoelectronic properties. The hypothesis of the MIS model has been also assumed in CdTe solar cells. According to the MIS model it has been observed that when the CdS is doped with Cu prior to CdTe deposition, efficient solar cells are obtained[38].

Second, most of the reported solar cells have been fabricated with the CIGS structure. The option of develop devices in a superstrate structure, (i.e. the deposition of buffer onto TCO, followed by the deposition of the absorber), could favor the properties of the solar cells, especially when deposition methods of absorber imply high roughness of the films like spray pyrolysis. In this way the roughness should have less impact in the properties of the solar cells. However for this case, is not possible the long-time (~30min) high temperature (>525°C) annealing need to obtain high crystalline quality absorbers. Thus for applying this idea, different already crystallized absorbers should be deposited onto the CdS buffer layer, maybe by dip coating or screen printing of nanoparticles, for example.

Third, as it was analyzed before, the use of Mo as back contact is associated to a $Mo(S,Se)_2$ compound layer which can behaves as a blocking back contact. Therefore, the option of using other types of metals is an open option.

Fourth, band alignment at the buffer/absorber layer interface is a critical aspect that needs a more complete study in order to understand the Voc limitation in these devices. With post-thermal annealing and thinner buffer layers it would be possible to improve the properties of the buffer/absorber heterojunction. The influence of low-temperature post-deposition annealing is currently under investigation, but widely reported to be beneficial for kesterite and chalcopyrite solar cell devices [17, 24, 39].

Several aspects must be solved before CZTSSe could be validated as an alternative to the already industrialized CdTe and $Cu(In,Ga)(S,Se)_2$ solar cells. First, a deeper understanding must be achieved on the formation of secondary phases, grain boundary barriers, buffer/kesterite, back-contact/kesterite interfaces, band alignment and long-time stability.

1.3 Kesterite: deposition methods and efficiencies

Currently the biggest challenge in the kesterite-based solar cells is their low open-circuit voltage, as the current 12.6% CZTSSe world record device[9] witnesses, reaching only 58% of the maximum theoretical attainable open-circuit voltage. A low Voc can result from a number of problems including[40]: the presence of high concentration of defects that reduce the minority carrier life time; the presence of high density of states in the gap, the partial compositional disorder that results in non-beneficial band gap variations and those sub-

1. Introduction

bad gap adsorption and emission. Also, improper band alignment between device layers which is strongly related with the deposition process of each layer.

Substantially high efficiencies from solution processes synthesized absorbers have been reported, for example the selenization of CZTS layers of nanocrystals with device efficiencies of up to 7.2%[41] (Eg = 1.1eV). As well as other chemical routes to CZTSSe thin film solar cells by the spin coating of salt metals and thiourea in DMSO with efficiencies of 4.1%[42].

Table 1 shows the state of the art of the world record efficiencies for η > 9% of kesterite-based devices for pure-sulfur, pure-selenium and sulfu-selenide kesterite solid solutions. In Table 1, the deposition technique, the key facts in each process and the main optoelectronic parameters are shown. It is worthy to notice that the table is dominated by solution-based process were IBM is leading.

Table 1. Selection of record efficiencies (η>9%) for kesterite-based solar cells.

Material	Technique	Key	η [%]	Voc [mV]	Jsc [mA/cm²]	FF [%]	Intitute
CZTSSe	Spin-coating	Hydrazine	12.6	513.4	35.2	69.8	IBM[9]
	Spin-coating	Hybrid buffer	12.3	471	37.1	70.3	IBM-Solar Frontier[43]
	Stacked metals	Bandgap grading	11.0	516.0	34.1	62.5	Solar Frontier[44]
	Spin-coating	CdS passivation	10.5	480	35.7	61.5	EMPA[45]
	Doctor blade	Se annealing	10.3	471	31.6	69.6	ZSW[46]
	Ultrasonic spray	Computer controlled	9.5	460	33.2	62.3	Hillhouse Group[40]
	Doctor blade	Nanocrystals, Hot injection	9.0	404	35.1	63.7	Purdue University[47]
	Co-evaporation	NaF doping	11.6	423	40.6	67.3	IBM[48]
CZTSe	Sputtering	H_2Se in N_2 annealing	10.4	395	39.7	66.2	CENA[49]
	Sputtering	Doping	10.1	453	33.3	66.8	IREC[50]
	Co-evaporation	Chemo-mechanical polish	9.8	380	37.6	68.9	NREL[51]
	Stacked metals	Hybride buffer	9.2	708	21.6	60.1	Solar Frontier[52]
CZTS							

In the IBM world record[9], the CZTSSe were synthesized using a hydrazine-based pure solution approach under Cu-poor and Zn-rich conditions of Cu/(Zn+Sn) = 0.8 and Zn/Sn = 1.1 in the starting solution. Mo-coated soda lima glass were used as substrates. They said that in the top of the films, some millimeter-range nonuniformities are observed; that could limit the device performance. The samples were coated with CdS (25nm, CBD), i-ZnO (10nm) and ITO (50nm). Ni/Al (2μm) top metal contacts and MgF_2 (110nm) were deposited by electron-beam to finish the 0.42cm² mechanically scribed devices. The key for this efficiency record as well as its drawback is the use of hydrazine that can not be used in line production.

1.3.1 Sprayed kesterite: state of the art

Using spray as synthesis or deposition technique has recently become very attractive. When spray is used as deposition technique of nanoparticles or colloidal solutions, the substrate temperature should be just enough to volatize the solvent; in the case of colloidal solutions a chemical reaction could also take place. Spray as synthesis technique is usually called *spray pyrolysis* and in this case, the elements in the precursor solution experiences a transformation produced by the action of the hot substrate; i.e. the preferred reaction when metal salts in solution are sprayed; it is the king of spray used in this thesis.

Table 2 shows a selection of efficiencies (η > 0.5%) of pure-sulfur kesterite devices obtained by different spray setups around the world. Some important spray parameters are shown, as well as the annealing conditions used for the remarkable efficiencies. Also, the key facts leading to the reported efficiency value are included in the table.

The actual record for pure-sulfur sprayed kesterite-based devices belongs to Larramona, G. et al.[53]. They recently, using a non-pyrolytic spray approach, reported 5% CZTS-based solar cells from sprayed Cu-Zn-Sn-S colloidal dispersion (10mg/ml) in water (90 vol%) and ethanol (10 vol%) without any organic additives, using a X-Y robot and N_2 as carrier gas inside a N_2 globe box. The synthesis of the out stoichiometry colloidal Cu-Zn-Sn-S mixture they used, was based on a direct precipitation of the chlorides in acetonitrile at room temperature in a N_2 globe box in order to avoid any possible oxidation or hydrolysis. It makes the synthesis of the colloid (particles: 10nm diameter) simple and very rapid compared to for example hot injection, as they said. Some traces of Na (~1% at, ICP-AES) were found on the dried colloids, which could assist the grain growth[54]. They found that exposing the as sprayed films to ambient air for several minutes hinders the formation of large grains and improves the compactness of the films upon annealing. It is a crucial step that using the setup of this thesis cannot be done. They also found that the films should be annealed first in pure N_2 (525°C,15min) followed by a second annealing in H_2S (3% in N_2) at 525°C (60 min) resulting in ~2μm films (Eg = 1.5eV). Prior the CdS (60nm) buffet layer deposition by CBD, their CZTS record sample was etched in HCl (8% in water) as IREC reported previously[19]. The samples were finished with magnetron spattered i-ZnO (60nm) and ITO (250nm) windows layers without anti-reflecting coating.

Table 3 shows the state of art efficiencies of CZTSSe-based sprayed devices for η > 0.7% obtained by different research groups around the world. Important spray parameters, key facts and optoelectronic properties of the reported devices are included. The record of sprayed CZTSSe devices belongs to the Hillhouse Research Group.

1. Introduction

Table 2. State of the art efficiencies (η>0.5%) of sprayed pure sulfur kesterite (CZTS) solar cell devices.

Spray (month/year) *Key*	Precursors (solvent) *Carrier gas (atm)*	Substrate temp. [°C] *Etching*	Annealing conditions	η [%]	Jsc [mA/cm²] *Voc [mV]*	FF [%] *Cell area [cm²]*	Rs(Rsh) [Ω·cm²]	Institute
-Pneumatic X-Y robot (3/2014) *Cu – Zn – Sn – S colloid*	CuCl, ZnCl₂, SnCl₄, NaHS (water/ethanol) *N₂ (N₂ globe box)*	300 *HCl (8%)*	N₂, 525°C, 15min +H₂S, 525°C,60 min	5	19 *630*	50 *0.25*	4(300)	IMRA[53]
Pneumatic (11/2012) *In₂S₃ buffer +In (8nm)*	CuCl, ZnAc, SnCl₄, Thourea (water) *Air (air)*	331	331°C, 30min	1.8	8.3 *430*	52	9.7(252)	Cochin Univ.[55]
Pneumatic (10/2014) *Substrate temp. composition*	CuCl₂, ZnAc, SnCl₄, Thiourea (water) *Ar(Ar)*	360 *KCN (1%)*	Ar, S+Sn 580°C, 30min	1.4	9.8 *421*	34.3 *0.09*	18(89)	IREC[56]
Pneumatic (5/2014) *Ar and Ar-H₂ carrier gases*	CuCl₂, ZnAc, SnCl₄, Thiourea (water) *Ar(Ar)*	220 *KCN (1%)*	Ar, S+Sn 580°C, 30min	1.4	10.7 *407*	33 *0.09*	17(70.8)	IREC[57]
Pneumatic (11/2013) *KCN etching*	CuCl₂, ZnAc, SnCl₄, Thiourea (water) *Ar(Ar)*	350 *KCN (1%)*	Ar, S+Sn 580°C, 30min	1.2	10.3 *356*	32.5 *0.09*	16(61)	IREC[58]
Pneumatic (10/2013) *Carrier gas and atm*	CuCl₂, ZnAc, SnCl₄, Thiourea (water) *Ar(Ar)*	450 *KCN (1%)*	Ar, S+Sn 580°C, 30min	1	7.5 *361*	37.1 *0.09*	15(103)	IREC[59]
Pneumatic (7/2014) *Composition, annealing*	Cu₂Ac, ZnAc, SnOct₂ , S (C₃H₇NO) *Air (air)*	160	520°C	0.9	6.7 *451*	31.0	43(102)	Nagaoka Univ.[60]
Pneumatic (01/2013) *Comp. optimiz., anneal temp.*	CuCl₂, ZnAc, SnCl₄, Thiourea (water) *Air (air)*	450 *HCl (10%)*	Ar, S+Sn 580°C, 30min	0.5	10.1 *173*	28.2 *0.09*	3.3(19.7)	IREC[61]

Collord, A.D., Xin, H. & Hillhouse, H.W. have very recently reported a 9.5% CZTSSe device using precursor inks formed by dissolving CuCl₂, ZnCl₂ and SnCl₂ anhydrous precursors with thiourea in DMSO[40]. After deposition the films were selenized at 540°C in a graphite box containing Se pellets. Immediately after annealing the films were coated with CdS (50nm) by CBD (65°C, 17min), the films were then selenized at 540°C (20min) under Ar flux (10sccm). Next, i-ZnO (50nm) and ITO (250nm) were deposited by RF-magnetron sputtering followed by Ni/Al evaporated top contact fingers. No use of chemical etching is mentioned for any step of the process, as well nor additives neither treatment to the

surface. This applaudable efficiency comes from the vast experience the members of the Hillhouse research group has on solution-based synthesis routes[62-64] especially for CIGS materials[65, 66]; they have done significant important contributions to the synthesis of CIGS nanocrystals[65-68]. In the recent years they have done important contributions to understand more the complex CZTSSe solid solution studying nanoparticles[41, 69-71]

Table 3. State of the art efficiencies (η>0.7%) for CZTSSe solar cell devices that have used spray as synthesis or deposition technique.

Spray (month/year) *Key*	Precursors (solvent) *Carrier gas (atm)*	Substrate temp. [°C] *Etching*	Annealing conditions	η [%]	Jsc [mA/cm²] *Voc [mV]*	FF [%] *Cell area [cm²]*	Rs(Rsh) [Ω·cm²]	Institute
Ultrasonic (1/2015) *Computer controlled, Ink-based NaCl doping*	CuCl₂, ZnCl₂, SnCl₂, Thiourea (DMSO)		Se, 540°C, 20min	9.5	33.2 *460*	62.3 *0.47*	0.68	Hillhouse Research Group[40]
Pneumatic X-Y robot (11/2014) *Cu – Zn – Sn – S colloid*	CuCl, ZnCl₂, SnCl₄, NaHS (water/ethanol) *N₂ (N₂ globe box)*	300 *HCl (8%)*	N₂, 525°C,15min +Se,SnS, 550°C,30min	8.6	30.9 *460*	60.0 *0.25*	1.4(300)	IMRA[72]
Pneumatic (4/2013) *Annealing time*	CuCl₂, ZnCl₂, SnCl₄, Thiourea (water) *N₂ (air)*	450 *KCN (10%)*	N₂ flow, Se, 530°, 25min	2.4	16.9 *360*			Incheon Univ.[73]
Pneumatic (to be send /2015) *Selenization temperature*	CuCl₂, ZnAc, SnCl₄, Thiourea (water/CH₃OH) *Ar (Ar)*	220 *Br₂-MeOH (0.025%)*	Ar, Se+Sn 550°C, 30min	1.9	16.3 *293*	39.4 *0.09*	7.2(51)	IREC[50]
Pneumatic (11/2014) *Composition, Br₂-etching*	CuCl₂, ZnAc, SnCl₄, Thiourea (water/CH₃OH) *Ar (Ar)*	235 *Br₂-MeOH (0.025%)*	Ar, Se+Sn 550°C, 20min	1.9	16.2 *292*	39.6 *0.09*	4.7(48.4)	IREC[74]
Ultrasonic X-Y (9/2013) *Sulfur source*	CuCl₂, ZnCl₂, SnCl₄, C₂H₅NS (ethanol) *N₂*	370 *KCN*	N₂, Se 600°C, 5min	0.7	6.2 *290*	38.3 *0.09*	0.87	EMPA[75]

Larramona, G. et al[72] improved their CZTS efficiency with CZTSSe-based solar cells using the same Cu-Sn-Sn-S colloid explained earlier, with a further annealing in Se atmosphere. The authors said they have first tested NaHSe as Se precursor for the colloid formulation but only efficiencies below 5% were obtained. Second, they found that the secondary phased formed by the interaction between the Cu-Zn-Sn-S and Mo play an important role also in the case of annealing in Se (only) atmosphere because of the applicable

mechanisms are different for each type of deposition technique and precursors. The third and last approach allowed the authors their record efficiency, after annealing they films from pure-sulfur colloidal solutions, the samples were hot plate annealed (525°C,15min) in a N$_2$ globe box, after this first annealing step the samples were expose to high power ultrasonication (10min) to *clean* the samples, after that, the samples were annealed in a graphite box containing Se and SnS (550°C, 30min) both annealing steps were performed following specific annealing profiles resulting in homogeneous distribution of S and Se with an optical band gap of ~1.1eV. The samples were finished as in their previous report but with Ni (50nm) and Al (1000nm) grid, without anti-reflecting coating.

Figure 2 summarizes the solar cell efficiency evolution of this thesis as Table 2 and Table 3 shows. It is the result of improved processes, techniques and skills.
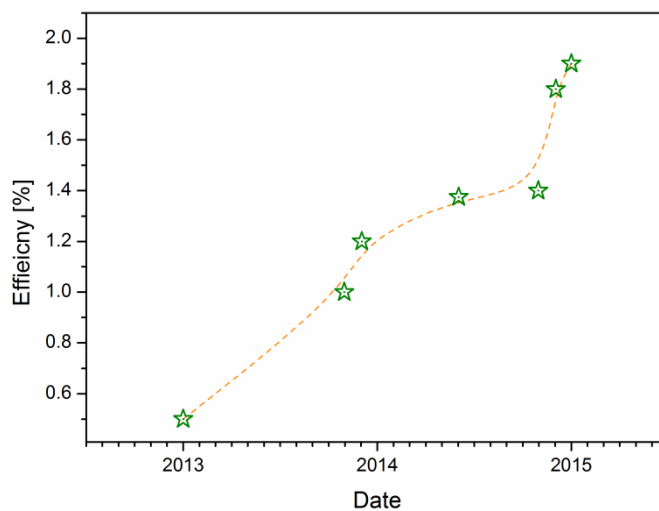
Figure 2. Solar cell efficiency evolution of sprayed kesterite solar cells at IREC.

1.4 Motivation, objectives and structure of this thesis

At the beginning of this thesis, spray pyrolysis was only randomly used to obtain kesterite thin films. It was tempting to use the sprayed films as the absorber layer in thin film solar cells and by that time no report was published of spraying in a controlled atmosphere and it was believed to be one of the main limitations of this technique.

The objectives of the thesis are:

iii. Start-up and understand the spray pyrolysis setup as a cost-effective deposition technique for kesterite thin films

iv. Optimize the system and solution parameters to obtain device grade kesterite thin films

v. Obtain working devices from sprayed kesterite thin films

vi. Optimize the device efficiency by means of spray and annealing parameters

1.4.1 Structure of this thesis

Following this Chapter, Chapter 2 presents the experimental methods from the spray pyrolysis setup towards the characterization of the sprayed materials and solar cells. Chapter 3 contains the main results when water was used as solvent. The optimization of the spray system, the precursor solution and the first sprayed solar cells are here presented. The chapter 4 deals in general with optimization the selenization variables when alcohol-containing starting solutions are used. Interesting results for novel photovoltaic applications are also included in chapter 4.

2 THIN FILMS BY SPRAY PYROLYSIS

The solution-based deposition techniques are attractive for the PV industry due to their potential for costs reduction combined with high throughputs. These include coating techniques as *spray*, spin coating, doctor blading, casting, painting, slot-die coating and knife-over-edge coating; and printing techniques as screen printing, pad printing, gravure printing, flexographic printing and offset printing [76].

During the last decades spray pyrolysis has become an attractive technique to deposit a wide variety of thin film materials. Such materials include thin films of metal oxides, metallic spinel oxides, binary, ternary and quaternary chalcogenides and also superconducting oxides[77]. Despite its simplicity, such ample diversity of sprayed materials supports spray pyrolysis as an attractive cost-effective deposition technique.

Over decades many studies have been done on the processing and preparation of thin films by spray pyrolysis. Chamberlin and Skarman[78], were the very first to report a CdS thin film obtained by spray. But it was in 1996 when Nakayama and Ito[79] first reported a Cu_2ZnSnS_4 thin film obtained by spray. It give way to spray pyrolysis as a deposition technique for this compound.

Unlike many other deposition techniques, spray pyrolysis is a very simple and relatively cost-effective processing method. The major advantage of spray pyrolysis is that it has full tunable parameters, allowing wide flexibility for process control also does not require high quality targets or substrates, the deposition rate can be easily controlled (but the films thickness has a limit), operates at an ample temperature range (100°C -600°C), there are virtually no restrictions on substrate material, dimensions or its surface profile. Subsequently, tailored conditions for specific substrates (e.g. nanoestructurated substrates) can be managed. Additionally reduced initial investments and lower production costs make this method an interesting deposition technique. Nevertheless, spray pyrolysis has some drawbacks, among them: presence of impurity phases on the films (for example in the case of CZTS: ZnO, Cu-S, ZnS are formed during spray time that

are hard to remove after[57, 80]), films have relative small grain sizes[81] and high surface roughness[61].

This chapter deals with the aspects of spray pyrolysis as deposition technique for CZTS films. First, a description of the possible model of thin film formation by spray pyrolysis is presented. Then a brief description of the spray set up developed and used in this thesis will be given. The last section is dedicated to the solution (solvent and precursors) used to spray the CZTS films.

2.1 Types of spray pyrolysis

Spray, as deposition technique, is sometimes also called: spray coating[13], chemical spray[13, 82]spray[13, 82], spray pyrolysis[83] and combinations of those. The previous names are very general names referring to the source of the precursors or the process involved in the film formation. Other kind of more specific names for this deposition technique emphasizes on the atomization method, each technique allows a different control over droplets size and their distribution across the preheated substrates.

The spray systems regarding their atomization technique might include nebulized spray[84], corona spray pyrolysis[85], electrostatic spray pyrolysis[86, 87], ultrasonic spray pyrolysis[81, 88] and pneumatic spray pyrolysis[61, 89].

In relation to the relative direction of the droplets, the spray systems can also be classified in two big configuration categories: horizontal and vertical configurations[83]. Those describe the droplets motion direction respect to the observer. In the vertical configuration, the droplets experience a free fall motion with initial velocity different to cero (provided by the carrier gas).

The way in which the substrate is heated also gives a name to the spray setup; if the substrate is heated by convection from the hot walls of the vertical or horizontal reactor, it is called hot-wall spray. If the substrate is heated by direct contact with the source of heat (e.g., hot-plate, tin-bath), the spray setup is called cool-wall spray.

In this work due to its ample applicability and flexibility, the most basic spray setup was used as the deposition technique of CZTS thin films: *cool-wall vertical pneumatic spray pyrolysis* (SP).

2.2 Model of deposition by spray pyrolysis

To explain the processes leading to film formation by spray pyrolysis has been the focus to many researchers; but our knowledge is far to be complete. There are empirical[90] and theoretical[91] models trying to understand the physics of droplets transport. However, the very large number of drops in a spray process, its high and varying velocity, the wide range of drop sizes in practical sprays, the changes in drop sizes with time due to evaporation and coalescence, the temperature gradient and the gas regions between neighboring droplets, are typically so complex that computational resources are insufficient to solve the dynamical and thermal interactions coupled in a large system of equations. It is the reason why the theoretical explanations of the spray deposition process simplify the hypothesis to ideal bounded conditions, revealing at first glance, the

complexity of the spray process. In this thesis, the system parameters leading to obtain device grade CZTS thin films were experimentally obtained.

In 2005, Perednis & Gauckler published a remarkable review[90] on thin film deposition using spray pyrolysis. Their compilation of experimental results guide them to establish a panorama of the spray parameters from a film quality perspective. They stated the importance of the process optimization for each parameter change and each material. Their findings, well match with the results and abservations of this thesis.

> *"Obtaining films by SP, involves different processes occurring either sequentially or simultaneously. Understanding these processes is helpful in improving film quality."*
>
> *Dainius Perednis & Ludwig J. Gauckler[90].*

There is a general agreement in dividing the thin film deposition process using SP into tree main steps[90, 91]. They come from observation and can be easily deduced or assumed because they follow a logic sequence.

The SP deposition process can be divided in tree steps:

    i.   Spray of the precursor solution.

    ii.   Transport of the resultant droplets.

    iii.   Pyrolysis of the droplets.

In Figure 3 the tree steps involved in the thin film deposition proses by SP are shown. For the picture the surface of the heater is at 400°C. The step i start and finishes rapidly while steps ii and iii need more time. Notice that step iii starts before the step ii is finished. The duration of step ii depends directly on the allowed pressure of the compressed gas. The start point of step iii will be determined by the temperature and droplet size.
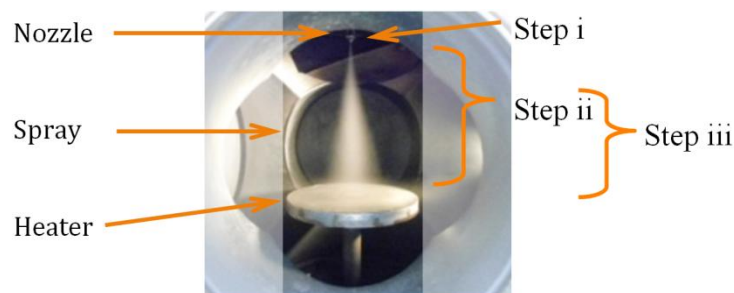
Figure 3 Picture showing the tree different steps on the SP deposition process.

In step i, droplets are generated from the precursor solution to form a spray. Here, *spray* might be understood as: liquid broken up into very tiny droplets and blown, forced into, or falling through the air[92]; it is the definition of spray.

Notice that, in step i, the precursor solution has just been transformed into multi-sized droplets each with individual velocity and direction therefore the spray is not a vapor.

Different nozzles produce different sprays in terms of droplets size distribution, coverage area, spray shape and initial velocity of the droplets.

Ideally, the nozzle should be able to produce mono-sized droplets, with effective spraying area bigger than the area of the substrate (or relative nozzle-to-substrate movement might be possible), with a near-round spray shape (linear spray shape also works with relative nozzle-to-substrate movement). The initial velocity should provide the droplets enough kinetic energy to allow them to travel (step ii) to the vicinities of the substrate to allow step iii to start. In a pneumatic spray system, the initial velocity of the droplets is determined by the pressure of the compressed gas; it is lower- and upper-limited by the specifications of the fabricator of the nozzle. If no relative nozzle to substrate movement is possible, the *cone angle* becomes important. In Figure 3, if L_1 is a line perpendicular to the heater connecting the discharge orifice of the nozzle and the central point of the heater and if P_1 is a plane such that L_1 is in P_1 then, the cone angle is the minim angle formed by two lines in P_1 that cut the spray contour. This definition applies for solid angle sprays and hollow conical sprays. In a pneumatic system, for a given nozzle, the cone angle depends directly on the pressure of the compressed gas. In general an increase of the cone angle increases the exposure of the droplets to the surrounding gas all the way through the step ii. If oxygen is present in such gas atmosphere, the oxidation of the precursor may occur.

In step ii, the generated droplets are transported. Their individual initial velocity, size, location within the spray cone and the substrate temperature will determine the physicochemical changes the droplets will experience during transportation. In a pneumatic spray setup, as the droplet traverses the ambient, there are tree forces that simultaneously can act on it; those forces will describe the path of the droplet and forces are: gravitational, thermophoretic and Stokes force.

The size of the droplets will be reduced during transport (step ii) due to evaporation of the solvent; it affects the influence of the forces on their trajectory. This evaporation might happen rapidly if the temperature of the substrate is too high (compared with the boiling point of the solvent) or if the droplet is too small. But if the temperature of the substrate is too low, the droplets will reach the surface. When most of the droplets are in the macroscopic scale (as in a pneumatic spray setup) gravitational force will have effect on them pulling them downward to the center of the earth. This force is a direct function of the density and size of the droplet. For large droplets, this force is the driving force behind the droplets transport; the small droplets will evaporate before arrive to the substrate.

The thermophoretic force pushes the droplet away from the hot surface of the substrate due to energy transfer. As the droplet is approaching the preheated substrate the molecules facing the direction of motion, acquire thermal energy from the hot ambient (if the droplet is near the heater, hot vapor might also exist) and when they touch the substrate the molecules from the hotter side of the droplet rebound with higher kinetic energy than those from the cooler side. This phenomenon is observed by the naked eye with good lighting, in droplets with one millimeter or les in diameter. In addition to the sizes of the droplets and the magnitude of the temperature gradient, the heat conductivity and heat absorption of the drops play a role. The thermophoretic force is a direct function of size of the droplet, the viscosity and temperature of the surrounding gas[91]. In non-electrostatic spray process, thermophoretic forces keep most droplets away from the substrate.

The Stokes force is the drag experienced by the droplet due to the gas resistance along step ii. This force is caused by friction between the droplet and gas molecules the drops are moving into. The Stokes force is a direct function of the viscosity of the gas, the size of the droplets, and relative gas-to-droplet velocity[91]. Therefore, large droplets which move with a high velocity will experience the largest retarding force.

As seen in Figure 3, step ii could finish before the droplets arrive to the substrate. As step ii is only related to the motion of the droplets when the solvent in the droplets is almost completely evaporated, step iii stars. It is also seen in Figure 3 how the droplets from the outer sides of the spray cone shields the inner drops from rapid evaporation. In a pneumatic spray setup, the spray cone has a central zone with higher drop density thus in the central zone more drops are likely to contribute to the film formation process.

In step iii, transformation of the droplets produced by the action of heat (pyrolysis[92]) is expected. The starting point of step iii for each individual droplet will depend on the size of the droplet, the proximity of it to the substrate and the temperature of the substrate. Figure 4 shows the simplified changes that a droplet could experience on step ii and iii. In Figure 4, the temperature axes reflects the temperature of the substrate as well as the position of it respect to the droplet. There are four physical forms in which the droplet might interact with the substrate.

Process A: If the temperature of the substrate is not high enough to vaporize all the solvent in the droplet, the droplet splashes on the substrate, vaporizes and leaves a dry precipitate in which decomposition occurs[93].

Process B: If the droplet continues experiencing an increase of its temperature, the size of the droplet is reduced due to solvent evaporation, it leads to a concentration gradient within the droplet. When the concentration exceeds the solubility limit, the precursor precipitates on the surface of the droplet and a dry precipitate hits the substrate. This results in the formation of particles in the sprayed films which are not desired because they increase films roughness.

Process C: When the processing environment causes droplets to evaporate a precipitate will form (process B). As the precipitate reaches the immediate vicinity of the substrate, it vaporizes (or sublimes). The vapor diffuses to the substrate to undergo a heterogeneous reaction there. This is a classical chemical vapor deposition (CVD) process which results in a high quality film deposition and a high sticking probability.

Process D: If a droplet is too small, if it is too far from the substrate (like the ones in the outer parts of the spray cone) and/or if the temperature is too high, the droplet quickly forms a precipitate. As the precipitate approaches the substrate, is vaporized and a chemical reaction subsequently occurs in the vapor phase. This homogeneous reaction leads to condensation into crystallites in the form of a powder precipitate. The powder reaches the substrate but without deposition reaction.
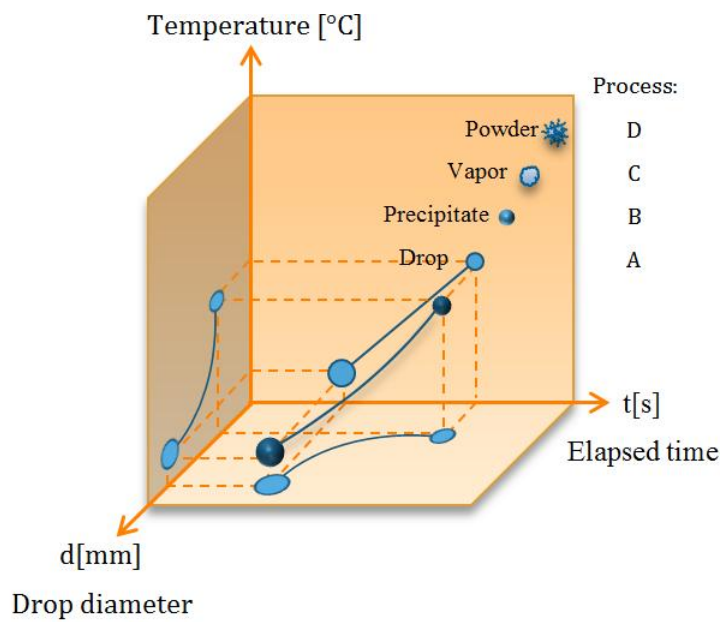
Figure 4. Evolution of droplet diameter during transport as it experiences increase in temperature.

An ideal deposition condition is when the droplet approaches the substrate just as the solvent is completely removed and the temperature of the substrate is enough to facilely a CVD-like process (process C). However, provided the droplet size distribution of each particular nozzle, the four processes happens simultaneously. As more homogeneous is the size of the droplets the more is possible to optimize the system parameters to the C-type deposition process.

2.3 Experimental

The typical SP equipment consists of a spray nozzle, air pressure control, precursor solution, liquid flow meter, substrate heater and temperature controller[94]. The ease with which parameters can be changed even during a film deposition, allows quite rapid determination of the necessary conditions for deposit. To obtain the desired properties, separate additional experimentation is required.

The system setup and the solution characteristics can have a significant impact on the film formation behavior. In this section the experimental aspects of the SP used in this thesis will be exposed going from the system itself to the solution.

2.3.1 Spray pyrolysis system setup

A sketch of the system setup used in this thesis is showed in Figure 5. The gas pressure control, the spray solution container, the liquid flow meter and the temperature controller, are not shown for simplification. In addition to the typical SP equipment, this spray system operates in the inside of a closable stainless steel 316 chamber. It allows to pump out the air from the chamber and then, fill it up with the desired gas (N_2, Ar, Ar-H) which might be also used as the carrier (or vector) gas. In this sense, it is possible to affirm that the films are sprayed under controlled atmosphere
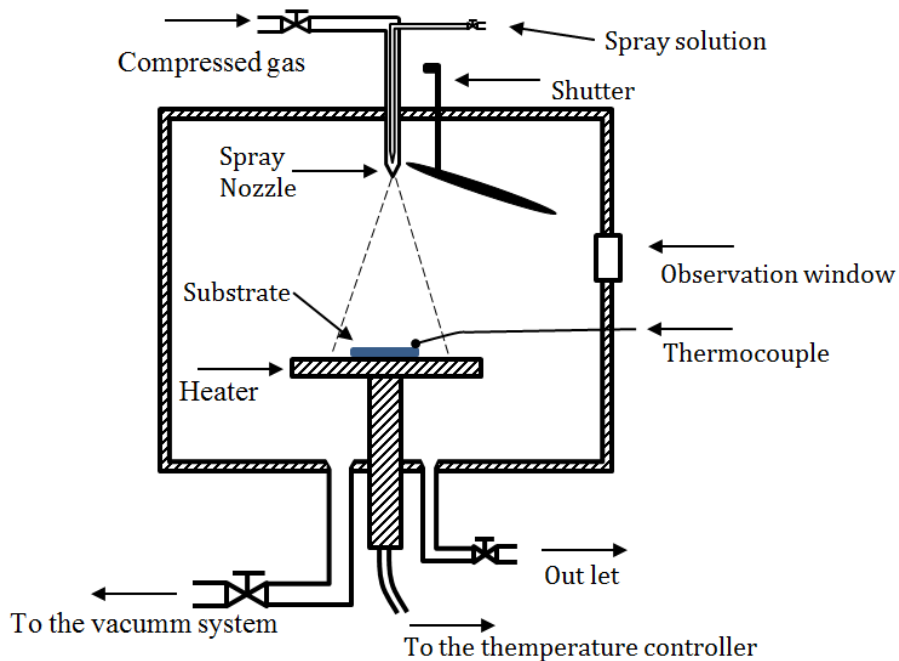
Figure 5. Simplified sketch of the system setup used in this thesis

The SP workshop at IREC is showed in Figure 6. The pressure of the gas used to spray the solution is controlled by a manometer in the range of 0-2.5 bar. The pressure inside the chamber is measured by a Oerlikon Thermovac TM 101 datalogger. The spray solution is pumped to the nozzle by a Masterflex L/S peristaltic pump.
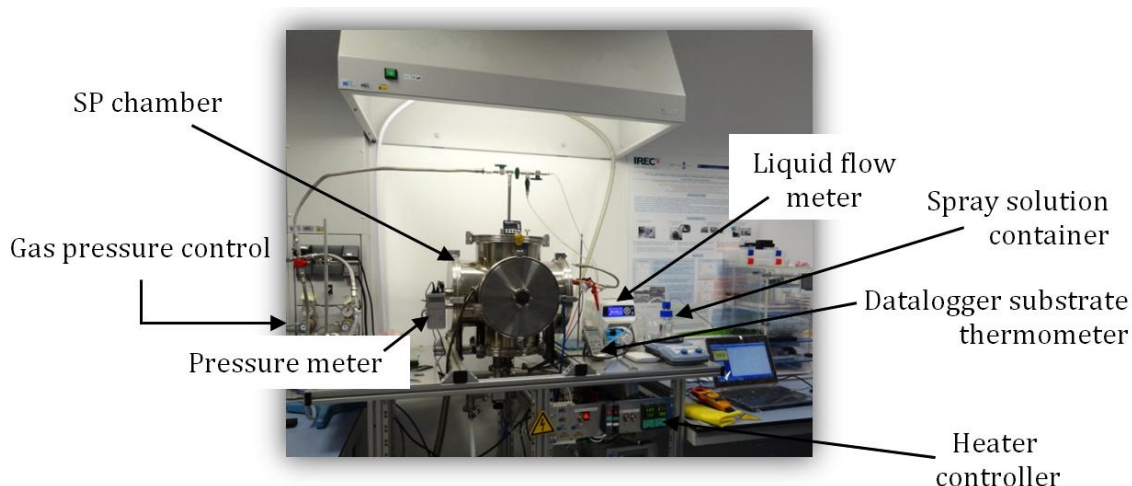
Figure 6. SP workshop at IREC

The temperature is in-situ acquired by a RS datalogger thermometer using a K-type thermocouple. The substrate temperature reported in this thesis is the temperature of a reference substrate placed aside to the spraying substrate; it is to avoid shadowing effects during the spray deposition process. In the next chapter those shadowing effects on film thickness will be shown. The heater depicted in Figure 5 is an electrical heater with two concentric heating zones embedded in a circular stainless steel plate. Its thickness is of approximately 3 centimeters which ensures well temperature inertia. Each zone is dynamic and independently controlled by the heater control to ensure a constant substrate temperature thought all the spray deposition process. For safety reasons and well preservation of the system, in all the experiments, the maximum power the control system allows to be delivered is never more than 80% of the SP power capacity. It means that the heater operating at the maximum allowed capacity can deliver 3.52 kW in each zone.

The SP power, the thermal inertia of the heater and a dynamic temperature control, allows a minimum substrate temperature decrease in both when the spray starts and during the spray deposition. The former is a common problem when using pneumatic spray setups and is due to heat exchange between the heater, the stream of pressurized gas and the droplets. In order to overcome this issue, different deposition profiles were tested using different substrate temperatures, solution fluxes and changes in the pressure of the carrier gas. The best solution is to start the steam of the pressurized gas without solution flow (no spray) before start the heating. It allows a slow heating of the substrate; when it reaches the desired temperature the solution is allowed to flow, in this way a minimum fall in temperature was observed. During deposition the dynamic control of the temperature plays an important role. This optimization processes will be reviewed in the next chapter. Another issue related with the temperature of the substrate is that it could be consider that the *real* substrate temperature is lower than the one is measured by the thermocouple because of the substrate surface is been cooled by the carrier gas and droplets, the thermocouple is also been cooled down. It can be consider just as a systematic measurement error.

To demonstrate the system capabilities, Figure 7 shows the temperature and chamber pressure profiles in a test run of the SP. For this test, the substrate heating rate was 35 °C/min as observed in the violet shadowed part of the heating period. Before that time, it is before 6.8 minutes, the control system reduces automatically the allowed power (diminishing the heating rate) to not exceed the desired temperature, in this case: 250 ±3°C; for this test run, the system only used 62.5% of power.

With respect to the gas used to spray and the atmosphere in which the deposition takes place, it is mighty to notice the difference between *spraying in a controlled atmosphere* with specific gas and *spraying in air ambient* with specific gas. In the second case (typical spray systems), the oxygen present in the ambient will contribute to the oxidation of the sprayed elements and the final films as well; no matters what the pressure of the carrier gas is. Despite this, oxygen is of course beneficial when producing oxide films, but is not the aim of this work.
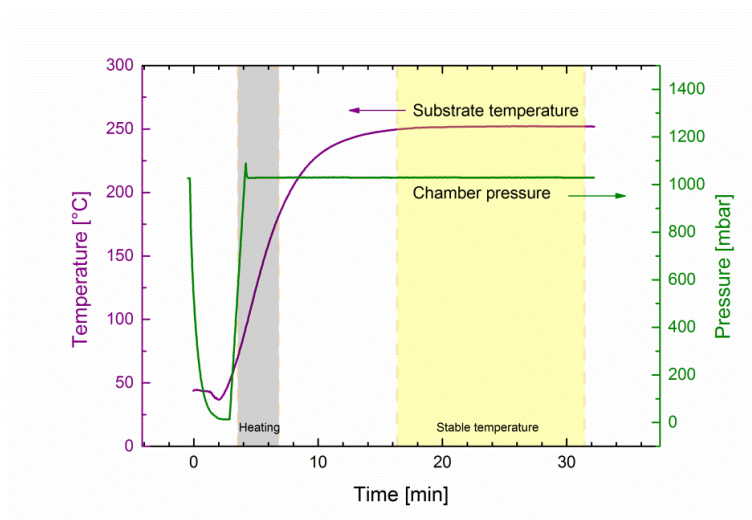
Figure 7 SP temperature and pressure profiles vs. time.

The SP chamber has a volume of ~0.86 m³ and is evacuated using a Oerlikon SOGEVAC SV 28 BI mechanical pump. The chamber can be filled up with the desired gas in 1.5 min, the pressure excess during a run, is released by the outlet valve shown in Figure 5. In all the experiments, after filling the chamber, the chamber pressure was kept at 1030 mbar allowing the extra pressure in the chamber to naturally flow out of it. Two different stainless steel 316 nozzles were used in this thesis, both are from spraying Systems Co., J2050 and J2850 in the round spray category, the second one is shown in Figure 8.

Figure 8. Nozzle used in the SP setup

As seen in Figure 5 and Figure 6 the SP setup and workshop have many variables that can be adopted as parameters, but mainly four of them will strongly influence the properties of the final films; those are:

  i. Inner chamber atmosphere.

  ii. Substrate temperature.

  iii. Time of spraying

  iv. Pressure of the carrier gas.

The influence and optimization of those parameters in the sprayed films will be shown in the next chapter.

2.3.2 The importance of the precursor spray solution

Thin film deposition using the SP technique, involves spraying onto a preheated substrate, usually a metal salt solution. An advantage of this deposition technique (in addition to the previously mentioned) is that it offers rapid solution preparation, but inherently, it has complex reaction chemistry. As a result of this aspect, the solution composition is tailored by the composition of the sprayed films. It adds an extra step to the films preparation process compared with high vacuum methods (e.g. sputtered metals); in such methods the composition is gained by just modifying the deposition time of each source. In the case of thin films prepared by SP, the deposition time is more strongly related with the thickness than with the composition of the films. However, the spraying atmosphere, the substrate temperature, the precursors and the solvent are strongly related with the final composition of the sprayed films and will be referred as the *composition related parameters.*

For the SP deposition technique, compared with spin and dip coating, the solution has to have low viscosity to facilitate the atomization process to form small droplets. It makes SP a suitable technique, adaptable to complex substrate shapes and sizes; as small and complex as nanostructured substrates as we will show in this thesis[74].

The starting materials which can be used are many, and the choice depends only on what appears to yield the best results from a device standpoint. The purity, freedom from other compounds or elements and their toxicity are usually well accepted deciding factors. The compounds used to provide the needed elements must be soluble in the solvent used and not react with each other or form precipitates. Ideally, the remainder of the starting components must be completely volatilized during the spray process.

Generally metals are in solution as their chlorides, acetates or nitrates; sulfur and selenium, exist for example in the form of N,N dimethylthiourea, thiourea and N,Ndimethhylselenourea and selenourea among many others. In this thesis, the chlorides and acetates of Cu, Zn and Sn as metal precursors were used and only thiourea was used as the sulfur source. The selenium incorporation into the Kesterite, to form $Cu_2ZnSn(S,Se)_4$ was achieved by annealing the sprayed films in a reactive atmosphere containing elemental selenium and tin. The annealing processes will be explained in detail in the next chapter.

The use of a solution is what gives to SP its character of chemical deposition technique[79, 80, 95-97]. In this work, the *precursor solution* refers to the specific proportions of solvents used to prepare the solution and the concentration of the selected salts in such solvent. The salt precursors used in this work are listed in Table 4

Regarding the chlorides, one advantage of using them is that they have high solubility in water (more than 70 g/100mL) and alcohols. The solubility of the acetates in water is lower (ZA, 43 g/100mL) but they are highly soluble in alcohols.

Table 4. Precursors

Formula	Name	Provider
$CuCl_2.2H2O$	Cupric chloride dihydrate	Sigma-Aldrich, ≥99.0%
$SnCl_4.2H_2O$	Tin(IV) chloride	Alfa-Aesar, 98.0%
$Zn(CH_3CO_2)_2$	Zinc acetate	Alfa-Aesar, 98.0–101.0%
CH_4N_5S	Thiourea	Sigma-Aldrich, 99.0%

The solubility of the precursors in the solvent is a very important parameter; it determines the maximum salt concentration in the solvent and the maximum concentration of the other precursors in the precursor solution. The concentrations used to prepare the spray solution will be presented in the next chapter, obtained during the optimization of the different process parameters. The solvents used in this work are listed in Table 5.

Table 5. Solvents

Solvent	Molecular formula	Boiling point	Supplier
Choline chloride	$C_5H_{14}ClNO$	not applicable due to decomposition on heating	Sigma-Aldrich, >98%
Water	H_2O	100 °C	
Ethanol	C_2H_6O	78.4 °C	Sigma-Aldrich,
Methanol	CH_4O	64.7 °C	Sigma-Aldrich,

For the chemical solution deposition techniques, the solvent characteristics that may define film formation and properties are[98]:

SOLVENT QUALITY AND VAPOR PRESSURE.

Related with the drying and film formation processes. It will dictate the minimum substrate temperature that is needed in order to evaporate it in the vicinities of the

substrate. Water or short-chain alcohols are preferred as solvents in SP as they have higher vapor pressures. On the contrary, low volatility solvents that use to have long C-chains, can inhibit reactivity between precursor species and the contained carbon is hard to remove after.

CONCENTRATION AND VISCOSITY OF THE SOLVENT.

It is related with thickness and uniformity of the films. The concentration refers to the proportion of two different solvents when they are mixed in the solution (e.g. 50% water + 50% alcohol, v/v). In this case, some precursors may be more soluble in one solvent than in the other. In SP solvents with low viscosity are preferred.

REACTION TENDENCIES AND BI-PRODUCTS.

It refers to the solution stability over time. After disassociation of salts due to thermodynamic interactions between solvent and solute, it is desired that the metals kept as ions in the solution for further pyrolytic reaction. During the solution preparation, for a given solvent, the precursors might be susceptible to hydrolyze, form segregated phases, conglomerates or precipitates affecting the CVD-like deposition process. Those changes in the solution might not happen immediately but depend on time and temperature.

Finally, the election of precursors and solvent has to be done before the optimization of the other parameters. It is because the system parameters depend on the type of precursor solution. Three parameters solution-related will strongly influence the properties of the final films; those are:

  i.   Solvent.

  ii. Concentration of precursors.

  iii. Solution flux.

They, in varying degrees are related to the composition and thickness of the final films, having a significant impact on the film formation characteristics.

In summary, the process to obtain thin films by SP involves many parameters that have to be taken in to account. To make understandable the relation between the solution-related and the system-related parameters, a schematic representation of its interrelation is shown in Figure 9. In order to simplify the figure, not all the interrelations are shown. For example, different nozzles could need different solution fluxes. The time of spraying may also depend on the concentration of the salt precursors. The pressure of the carrier gas will cool down the substrate temperature, and so on.
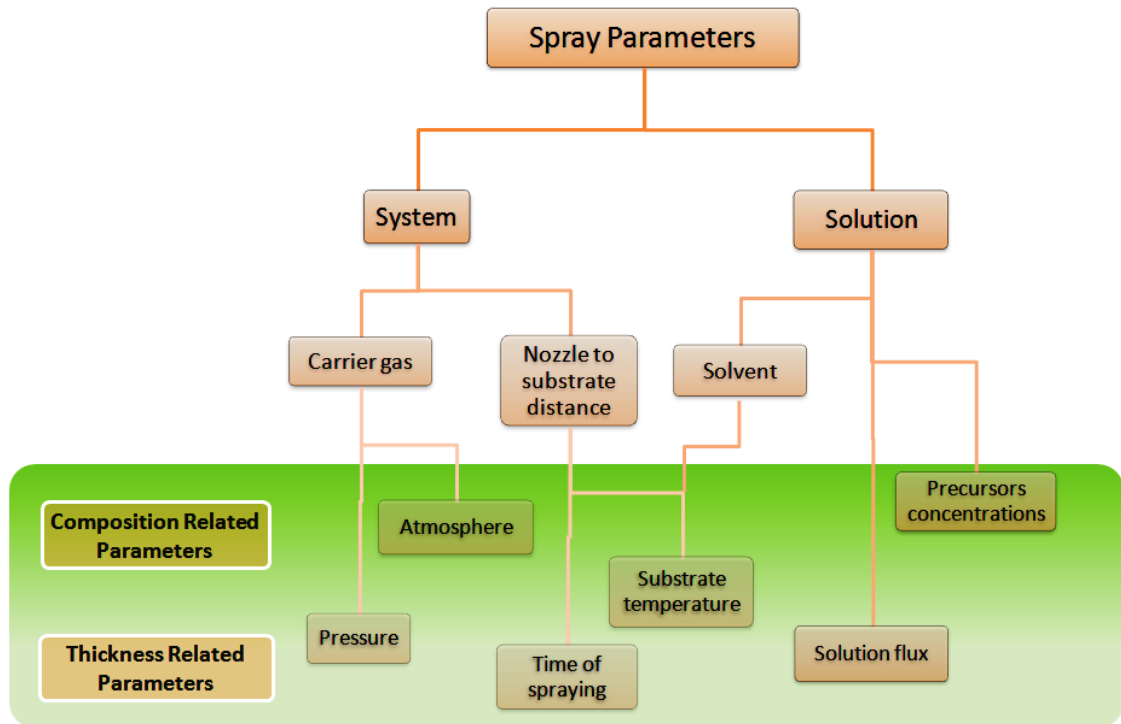
Figure 9. Schematic representation of the SP parameters and their relation with the composition and thickness of the sprayed films

We can correlate the parameters with two main characteristics of the sprayed films, which will influence the performance of the final devices: the thickness and composition of the as-sprayed layers. However, the ultimate films properties depend on the deposition and thermal annealing conditions. In the next chapters those parameters will be examined and presented.

2.4 Solar cells fabrication

The structure of the solar cells produced in this thesis is shown in Figure 10. It corresponds to a substrate structure similar to the traditionally used for the CIGS technology.
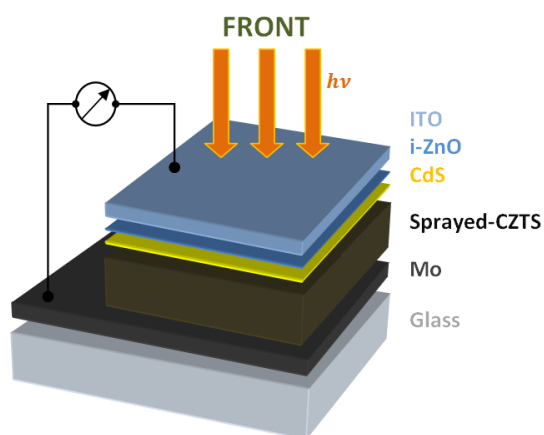
Figure 10. Kesterite-based solar cells layout

This thesis is centered in the study of the properties of the sprayed CZTS films passing though all the spray parameters involved. In the following pages a brief description of the different layers in the solar cells is given.

2.4.1 Mo back contact

Mo layers were deposited by DC magnetron sputtering (Ac450 Alliance Concepts) from a four-inch diameter 99.99% purity target under the following conditions: $4.3Wcm^{-2}$, 0.0006mbar, 10sccm (Ar) and 10rpm by 39 minutes at 120°C. The resulting in Mo layers are 800nm in thick with a sheet resistance $R_{sheet} = 0.16\Omega/sq$.

Additionally, in some cases (all the films in chapter 4) to prevent the interaction between the forming Kesterite and the Mo layer during the annealing process, an intermediate i-ZnO layer in the top of the Mo-coated SLG was used, as we reported[34]. For this purpose, 10nm of i-ZnO were deposited onto the fresh Mo substrates by DC-pulsed magnetron sputtering deposition (CT100, Alliance Concepts) under the following conditions: 1.48 Wcm^{-2}, 0.001mbar, 19.9sccm (Ar) and 0.1sccm (O_2), 10rpm at room temperature by 90s using 99.99% purity i-ZnO target. The SLG/Mo/i-ZnO substrates were cut in $3x3cm^2$ pieces and referred hereafter as substrate.

During the first spray seconds the chamber is filled with vapor of water, from them Mo oxidation occurs mainly in the early stages of the deposition, catalyzed by the hot Mo surface forming MoO_2[99] affecting its wettability. It affects the formation of the absorber and degrades the optoelectronic properties of the solar cells creating a resistive layer for carrier transport; the use of the intermediate i-ZnO layer prevents this oxidation and helps the well adhesion of the films. As we will show, the use of this intermediate layer is of high importance to produce working devices from sprayed absorbers.

2.4.2 Reactive thermal annealing under chalcogen atmosphere

The sprayed samples (cut in $1.1x2cm^2$ in area) were reactively annealed in two graphite boxes, one dedicated to the formation of the CZTS films and other to the formation of the CZTSSe absorbers.

All the annealing processes were done in a three zone tubular furnace (capable of working at 10^{-4}mbar). The heating rate, duration and temperature was computer-controlled. Ar was used as carrier gas; before start heating, the atmosphere of the furnace was cleaned several times by repeatedly filling (with Ar) and evacuating.

For the pure sulfur absorbers, 50mg of sulfur (Alfa-Aesar, 99.995%) and 5mg of tin (Alfa-Aesar, 99.999%) was used. The Ar-base pressure of the furnace at room temperature was 640mbar, with the temperature the pressure increases until 1bar at the set annealing temperature (520-580°C, see chapter 3). With a heating rate of 20°C/min the typical annealing duration was 30 min. After annealing the sample was cooled naturally.

To form the CZTSSe absorbers, 20mg of Se (Alfa Aesar, 99.995%) and 2mg of Sn (Alfa Aesar, 99.995%) was used. In this case, several annealing profiles were investigated (see chapter 4), using in all cases a heating rate of 20°C/min. After annealing the samples were cooled at -5°C/min.

2.4.3 CdS-Buffer layer

Prior to the deposition of the CdS-buffer layer all the annealed absorbers were etched in 18MΩ deionized water by 10 minutes under magnetic stirring[100]. Two different CdS buffer were used, both deposited by chemical bath deposition (CBD), the difference in the buffer-layers comes from using two different cadmium precursor sources, namely $CdCl_2$, cadmium chloride and $Cd(NO_3)_2$, cadmium nitrate[24].

The precursor were dissolved in water with a concentration of ($[CdCl_2]$ or $[Cd(NO_3)_2] =$ 0.12 M, $[CH_4N_2S]$=0.3 M, pH = 9.5, T = 75 ºC), the concentration of Cd and S was kept the same in both solutions.

In the first part of this thesis (chapter 3, pure sulfur kesterite), $CdCl_2$ was used as the Cd precursor. In this case, the CBD process takes 7 minutes, resulting in a uniform pinholes-free CdS layer with an estimated thickness of 70 nm (calibrated by XRF on CdS samples deposited on glass). Prior the depositions of this CdS, the samples were etched 2 minutes in KCN, 1% (w/v).

The CZTSSe-based solar cells in chapter 4 were prepared using $Cd(NO_3)_2$ as the Cd source. The process takes 50 minutes to reach an estimated CdS thickness of 46±7 nm. The use of $Cd(NO_3)_2$ results in a much slower growth kinetic of CdS, allowing the preparation of thinner layers with higher quality. Additionally, S is more effectively incorporated into the CdS layer, due to the better control of the CdS precipitation. Using this Cd precursor, the growing time were increased in 5 minutes for the sprayed samples of this thesis to warrantee a better coverage of the rough surface of the samples. Prior the depositions of this CdS-buffer layer, the CZTSSe samples were etched in HCl 10% (v/v) at 75°C by 2minutes[19]. It was found that a KCN etching for sulfo-selenium sprayed films results in non-rectifying devices, with no power conversion efficiency.

2.4.4 i-ZnO and front window layer

After the CdS-buffer layer a i-ZnO thin layer (50nm) was deposited by pulsed DC-magnetron sputtering followed by a transparent conducting oxide layer (TCO).

The CZTS-based and the CZTSSe-based solar cells were finished with a ZnO:Al (450 nm, R_{sheet} = 20Ω/sq) and ITO (400nm, R_{sheet} = 25Ω/sq) deposited by pulsed DC-magnetron sputtering, respectively.

For the optoelectronic characterization, 3x3mm2 cells were scribed, using a micro-diamond scriber (MR200 OEG), neither metallic grid nor anti reflecting coating were used.

2.5 Characterization of materials and devices

In the following sections, the main methods used in this thesis for the characterization of materials as well as devices are briefly presented.

2.5.1 Material characterization

X-Ray Florence (XRF)

To determine the composition and thickness of the samples a X-ray fluorescence (XRF) Fisherscope XVD system was used. The system is routinely calibrated with ICP-OES (inductively coupled plasma optical emission spectroscopy, Perkin Elmer Optima 3200RL). Specific procedures are used depending on the type of substrate and elements present in the samples using an acceleration voltage of 50kV with a Ni filter using 1023 channels over the voltage range. Commonly 9 points were measured on each sample with a integration time of 45 seconds.

Scanning electron microscopy (SEM)

The surface and cross section morphology of precursors and annealed films was analyzed by scanning electron microcopy using secondary electrons (SE) in a FEI Nova™ NanoSEM 230 system using a work distance of 5mm and an operating voltage of 5 kV. The samples were cut for the cross sections using a Dremel moto-tool with variable speed coupled with a diamond disc then the cut samples were Ar blown to remove dusts. Silver paste and carbon tape was used to create an electrical circuit to avoid image drifting.

To analyze the composition of the surface particles on the films, the abundance of the elements on the sample was obtained by energy-dispersive X-ray spectroscopy at 20kV using the α emission lines.

Raman spectroscopy

The as sprayed and annealed films were characterized by Raman spectroscopy using different wavelengths, in a backscattering configuration in particular T64000 Horiba-Jobin Yvon spectrometer using the 514.5 nm excitation wavelength of an Ar+ laser, and with a LabRam HR800-UV Horiba Jobin-Yvon system with a 325 nm (UV) excitation wavelength.

UV-vis-NIR spectroscopy

To estimate the band gap of the samples, the transmittance and reflectance were recorded in the wavelength range 400–2500nm, using a Perkin Elmer Lambda 950 UV/VIS Spectrometer prior system cero calibration.

X-Ray Diffraction (XRD)

Information of the samples' crystal structure was obtained by X-ray diffraction analysis on an Advance D8 diffractometer (Bruker) using CuK α radiation (λ = 1.5406 Å, 40 kV, 40 mA). To this end, typical θ–2θ measurements were performed from 15° to 70° with a step size of 0.010° and integration time of 2 seconds.

2.5.2 Solar cell characteristics

Current Density – Voltage (J-V) Curve

The current density (J) as function of the voltage (V) for solar cells can be written by the one-diode model under illumination as follows[101]:

$$J = J_o \left[exp \frac{q}{A k_B T} (V - Rs) - 1 \right] + \left(\frac{V - R_s J}{R_{sh}} \right) - J_L$$

Where J_o is the dark saturation current, q the electron charge, k_B the Boltzmann constant, T the absolute temperature, J_L the light generated current density, A the diode ideality factor, R_s and R_{sh} the series and shunt resistance respectively. The value of the ideality factor has a value between 1 and 2, high values indicate the presence of transport mechanisms different to diffusion which also implies a low V_{oc}.

Figure 11 shows the short-circuit current density (J_{sc}) and the open-circuit voltage (V_{oc}), they are the maximum values of current density and voltage that the solar cell can deliver however, for such operational values the power is cero.
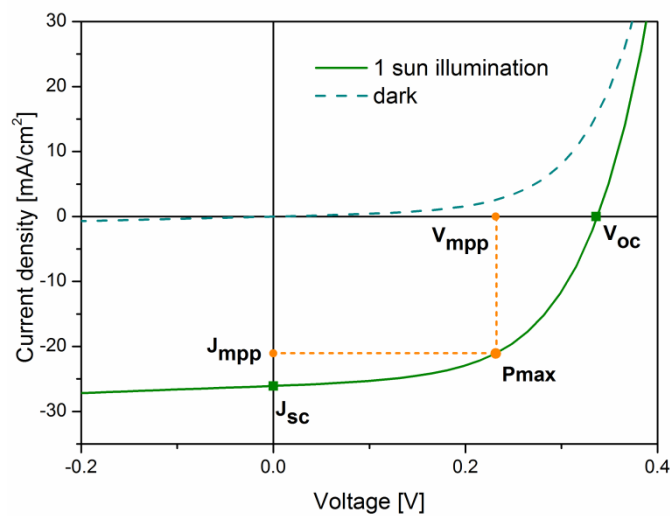
Figure 11. J-V characteristic of a high efficiency CZTSe solar cell[24].

2. Thin Films by Spray Pyrolysis

The maximum power point value is given by

$$P_{max} = J_{mpp} * V_{mpp}$$

Where J_{mpp} and V_{mpp} are current density and voltage at the maximum power point; they help to define the fill factor (FF). The FF is a parameter that determines the squareness of a J-V curve given by

$$FF = \frac{J_{mpp} * V_{mpp}.}{J_{sc} * V_{oc}}$$

The power conversion efficiency or simply efficiency (η) gives the ratio of how much of the solar power can be converted into electricity, it is defined as follows

$$\eta = \frac{J_{mpp} * V_{mpp}}{P} = \frac{J_{sc} * V_{oc}}{P} FF$$

It depends of many factors, such as the incident radiation spectrum, the intensity, the operation temperature and the recombination mechanism that determines the values of J_{sc}, V_{oc} and FF. Because of that, the efficiency is the merit figure of a solar cell.

The J-V dark and illuminated curves were carried out at 25°C using a Sun 3000 class AAA solar simulator (Abet Technologies Inc., Milford, Connecticut, USA; uniform illumination area of 15x15 cm²) with calibrated intensity to 1 sun AM 1.5 by using a Si reference cell.

QUANTUM EFFICIENCY CURVE

The quantum efficiency is the ratio of the number of carriers collected by the solar cell to the number of photons of a given energy incident on the solar cell. The quantum efficiency ideally has a square shape but it is reduced due to recombination effects and optical losses. It can be viewed as the collection probability due to the generation profile of a single wavelength, integrated over the device thickness and normalized to the incident number of photons.

The external quantum efficiency (EQE) includes the effect of optical losses such as transmission and reflection. The spectral external quantum efficiency measurements were made using a Bentham PVE300 system (Bentham Instruments Ltd, Berkshire, U.K.) calibrated with a Si and Ge photodiode using a step size of 5nm.

3 FROM AQUEOUS SOLUTION TO SPRAYED CZTS SOLAR CELLS

As most of the spray systems usually operate under air conditions, this chapter is devoted to compare and study the properties of sprayed films that have been sprayed under air conditions but also under controlled inert atmosphere including Ar or Ar-H_2. The use of a controlled atmosphere is one of the main contributions to the development of the SP system in the present thesis.

The idea of using a controlled atmosphere to spray, is to reduce the presence of oxygen during the whole deposition process. The spraying atmosphere is the extra spray variable over which we show control.

In spray pyrolysis deposition, the atmosphere, in which the film-growth takes place is usually a neglected variable. From the historical and technical point of view to ignore the spraying atmosphere has many explanations related with the material and with the applications of it. As the final end of the sprayed-CZTS films is to become absorbers for photovoltaic applications, the quality of such sprayed films ought to be as good as possible. To obtain device grade CZTS films is not a simply task. It is not restricted only to spray pyrolysis, it is a challenge for all deposition techniques. Specifically, the use of SP to obtain device grade thin films poses a serious challenge from the technical and material sciences perspective.

The use of water as solvent and air as carrier gas is the logic first step that was used in the first section of this chapter. With that, encouraging results in solar cell devices were obtained. Characterizations of as sprayed films are presented in the different sections of this chapter as well as the study of the sulfurization of the different films. At the end of the chapter after using Ar as carrier gas (and atmosphere) and water as solvent, promising devices were obtained with power conversion efficiencies up to 1.4% after the optimization of system parameters, precursor solution and sulfurization.

3.1 Air as carrier gas

This section is partially based on the publication: Espindola-Rodriguez, M. et al. Compositional optimization of photovoltaic grade Cu_2ZnSnS_4 films grown by pneumatic spray pyrolysis. Thin Solid Films **535**, 67-72 (2013).

The ancient Greeks regarded air as one of the four elements. Today, air is not less important but it was not until the seventeenth century that air was recognized as a mixture of gases. Although later, even after knowing the existence and some characteristics of oxygen and nitrogen; the principal components of air, the question of whether it was a mixture remained. Now we know that in the air there are relative persistent gases that act as the background matrix within which the intricate chemistry of the atmospheric trace components takes place[102]. The constituent gases of the air are shown in Table 6.

Table 6. Composition of dry unpolluted air by volume[102].

Gas		Volume [%]
Name	**Formula**	
Nitrogen	N_2	78.084
Oxygen	O_2	20.946
Argon	Ar	0.934
Others		0.036

Air humidity (the result of water vapor in the air) is a factor that should not be neglected; it changes among other properties the density and heat diffusion of air. In compressed air from the atmosphere, the humidity and pollution could be reduced by filters and draying cycles however, the composition of compressed air cannot be warranted to be the same from one day to the next; additionally the ratio of the air's components shown in Table 6 varies just slightly, from place to place in the earth.

In order to have the same carrier gas in each spray experiment, in this section *compressed synthetic air* was used a carrier gas with a fixed composition of N_2 (80%) + O_2 (20%) and is referred simply as air.

3.1.1 Substrate temperature profiles

A substrate temperature profile is defined as the temperature that the substrate experiences inside the SP chamber before, during and after the deposition time. The temperature is measured directly on the top of the substrate or on an identical aside alternative substrate to avoid shadow effects. Using air as carrier gas, different substrate temperature profiles were tried.

Figure 12 shows two common substrate temperature profiles with strong changes in temperature before or after the growing time. In the first case (Figure 12a) the substrate was heated up until above 250°C in a static atmosphere inside the SP chamber. It can be seen that once the gas flow stars, the substrate rapidly cools down. Then the precursor solution is allowed to flow to start the spray, this also contribute to cools down more the substrate. Those fast temperature changes usually crack the substrate. Figure 12b shows what happens when no gas flow is allowed after the growing time. The thermal inertia of the heater increases the temperature of the substrate in some seconds. It stresses the film and substrate and usually results in compositional variations that are hard to control.
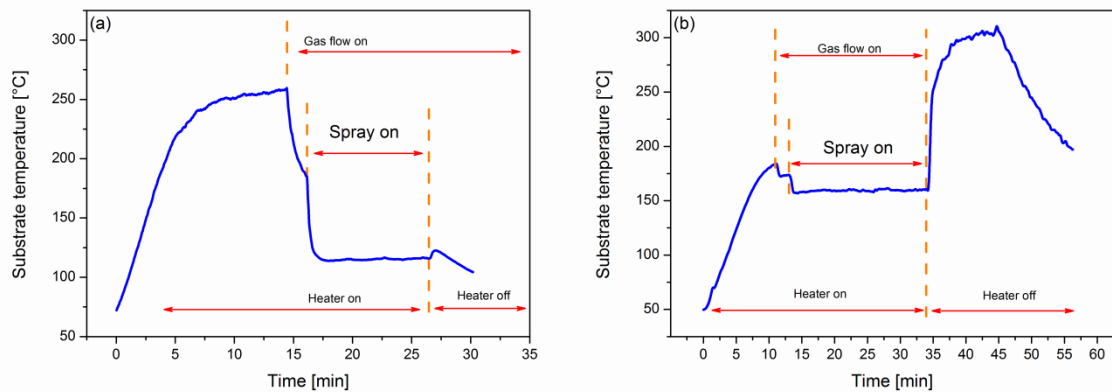
Figure 12. Different substrate temperature profiles. (a) gas flow is present from the spray on time and during the cooling time. (b) gas flow is only present during the spray on time.

Figure 13 shows the substrate temperature profile used in this thesis. The shown profile is the combination of the previous two profiles. In this case, a gas flow thought the nozzle is hitting the substrate all the time: before, during and after the spray on time. It helps to reduce drastic temperature changes that are positive for the film, substrate and SP system. The inset in Figure 13 shows the normal distribution of the substrate temperature during the spray-on period ($\mu = 235$°C, $\sigma = 1$ °C); the data presented is experimental logged data.
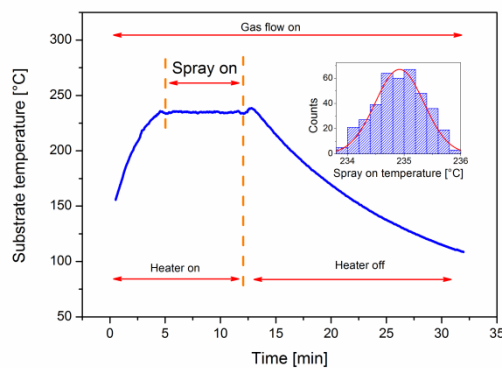
Figure 13. Substrate temperature profile. A gas flow is present all the time.

3.1.2 Thickness: solution flux and time of spraying

In order to investigate the effect of the solution flux [mL/min] and time of spraying [minutes], several experiments were done with a constant carrier gas pressure of 2 bar.

Figure 14 shows the contour map and x-, y-thickness profiles of two different samples sprayed under different conditions on substrates of 30 x 30 mm². The first and most noticeable characteristic is that, in all the sprayed films there is a thickness gradient from the center of the substrate and perpendicular to it. It is due to the kind of spray system used in this thesis that there is not x-y nozzle-to-substrate relative movement. The use of such a system is a possibility that is left open in this thesis.
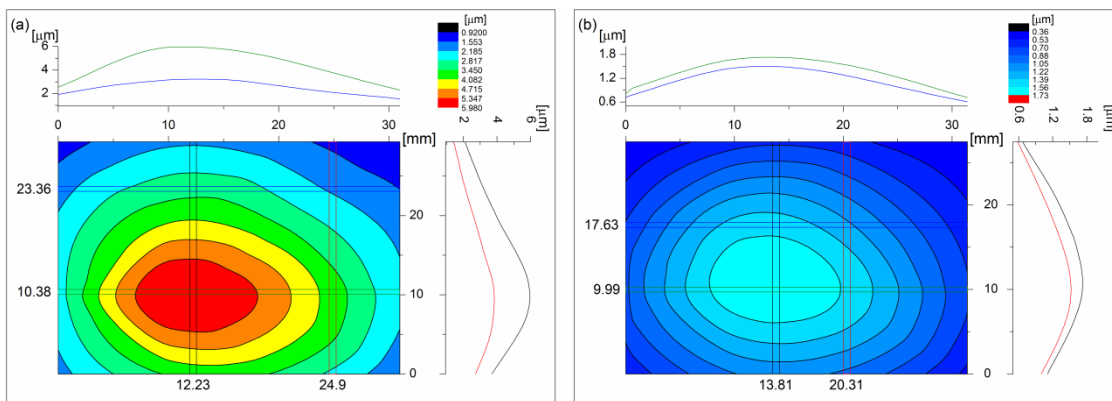
Figure 14. Contour map and x-, y-thickness profiles of different samples.
Using 4mL/min, (a) 30 minutes, (b) 20 min.

Figure 3 summarizes a series of experiments in which was studied the spraying time in relation with the absolute value of the films thickness and their corresponding homogeneity. By using a flux of 4mL/min, two different times were used to spray the films. Figure 14a show that after 30 minutes of spray; the film reaches a maximum thickness on its central part of about 6µm as confirmed by the x-, y-profiles. Out of the center the films has a thickness of about 3µm; this difference reveals the strong thickness gradient. By reducing the time of spraying (Figure 14b) the thickness of the films is also reduced. After 20 minutes of spraying, the films have typically a central zone with about 1.7µm in thickness; out of this central zone, the thickness is measured to be 1.5µm.
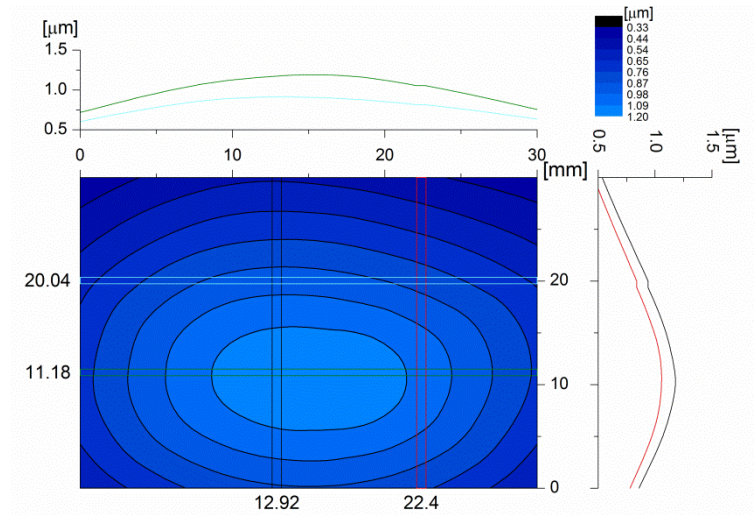
Figure 15. Contour map and x-, y-thickness profiles of a sample using 3mL/min, 20min

Figure 15 shows a typical contour map and x-, y-thickness profiles of a sample, sprayed this time with a lower precursor solution flux of 3mL/min, but with the same time (20min) as in Figure 14b. Figure 15 shows a film whose central zone has a maximum thickness of 1.2μm; 15mm from that point the thickness is measured to be 1μm. It shows the beneficial effect in thickness and the corresponding homogeneity of using low fluxes; this time in the central zone the difference in thicknesses is about of 200nm. Sprayed films of 1.2±0.2μm in thickness are good candidates to perform a compositional optimization as CZTS absorbers are required to be ~1μm in thickness. The reason of using in all this section the same carrier gas pressure (2bar) is that, it is limited by the nozzle design. In the following sections, the influence of both, the concentrations of the metal precursors (mainly Cu and Zn) and the annealing conditions on the properties of the CZTS films are investigated.

3.1.3 Compositional optimization of air sprayed CZTS films

In this section is investigated the effect of the precursor's concentrations on the obtained sprayed CZTS layers by respectively:

vii. Reducing the Cu concentration

viii. Increasing the Zn concentration

ix. Reducing Cu concentration and at the same time increasing the Zn concentration.

The films presented in this section where made using $CuCl_2.2H_2O$, $Zn(CH_3CO_2)_2$, $SnCl_4.2H_2O$ and CH_4N_5S in a stoichiometric concentration of 9mM, 4.5mM, 4.5mM and 50mM respectively, where the salts were dissolved in 18MΩ deionized water. Thiourea was intentionally chosen in excess with respect to the stoichiometric concentration to compensate the loss of sulfur reported[97, 103] when using purely aqueous solutions.

To stabilize the precursor spray solution, and in order to avoid its precipitation; the Sn precursor was prepared in aqueous acid media (pH<2, by HCl). Afterwards, the Zn, Cu and S precursors were sequentially added. With the parameters shown in Figure 15, the next

step was in the direction of optimize the composition of the sprayed films using air as carrier gas. Depositions were carried out for stoichiometric solutions (St) and for Cu-poor and Zn-rich solutions as explained in Table 7, the solutions were named according the concentration of the precursors as well as the resulting samples. The thiourea concentration was in all the cases 50 mM, and the Sn concentration 4.5 mM.

Table 7. Summary of the different solutions and films prepared, where the name, precursor salts concentration and comments are included.

Solution Name	Solution concentration		Solution ratios			Comments
	Cu [mM]	Zn [mM]	$\dfrac{Cu}{Zn+Sn}$	$\dfrac{Zn}{Sn}$	$\dfrac{Cu}{Sn}$	
St	9.00	4.50	1.00	1.00	2	Stoichiometric
-10% Cu	8.10	4.50	0.90	1.00	1.8	Cu poor
-20% Cu	7.20	4.50	0.80	1.00	1.6	Cu poorer
+10% Zn	9.00	4.95	0.95	1.10	2	Zn rich
+20% Zn	9.00	5.40	0.91	1.20	2	Zn richer
+10% Zn-10% Cu	8.10	4.95	0.86	1.10	1.8	Cu poor, Zn rich
+20% Zn-20% Cu	7.20	5.40	0.73	1.20	1.6	Cu poorer, Zn richer

Table 8 shows the XRF elemental composition of the sprayed CZTS films. Using the stoichiometric solution the resulting films were non-stoichiometric, in fact slightly Zn-rich and Sn-poor composition was found. The films sprayed from the Cu-poor and/or Zn-rich solutions showed a systematic variation on its composition in agreement with the expected values of the precursor solution.

Table 8. Compositional ratios of as-sprayed CZTS films

Sample	Thickness [μm]	$\dfrac{Cu}{Zn+Sn}$	$\dfrac{Zn}{Sn}$	$\dfrac{Cu}{Zn}$	$\dfrac{Cu}{Sn}$	$\dfrac{S}{M}$
St	1.15	1.00	1.10	1.91	2.11	0.39
-10% Cu	1.18	0.92	1.13	1.74	1.97	0.38
-20% Cu	0.87	0.80	1.15	1.49	1.71	0.24
+10% Zn	0.98	0.99	1.23	1.80	2.21	0.44
+20% Zn	1.48	0.89	1.32	1.57	2.07	0.36
+10% Zn-10% Cu	0.90	0.90	1.04	1.76	1.84	0.46
+20% Zn-20% Cu	1.80	0.75	1.50	1.26	1.88	0.49

As shown in table 3, the films are sulfur-deficient although after using a high thiourea concentration in the precursor solution; implying the necessity of an annealing sulfurization step. The necessity of a high temperature thermal annealing will be also confirmed by Raman scattering. Aside from the sulfur incorporation after annealing, the crystallinity, the optical and electrical properties of the samples are also tremendously improved as detailed on the following section.

3.1.4 Sulfurization of air-sprayed CZTS films

Figure 16 shows the metallic ratios of selected samples after sulfurization at different temperatures, whiles other parameters were kept constant.
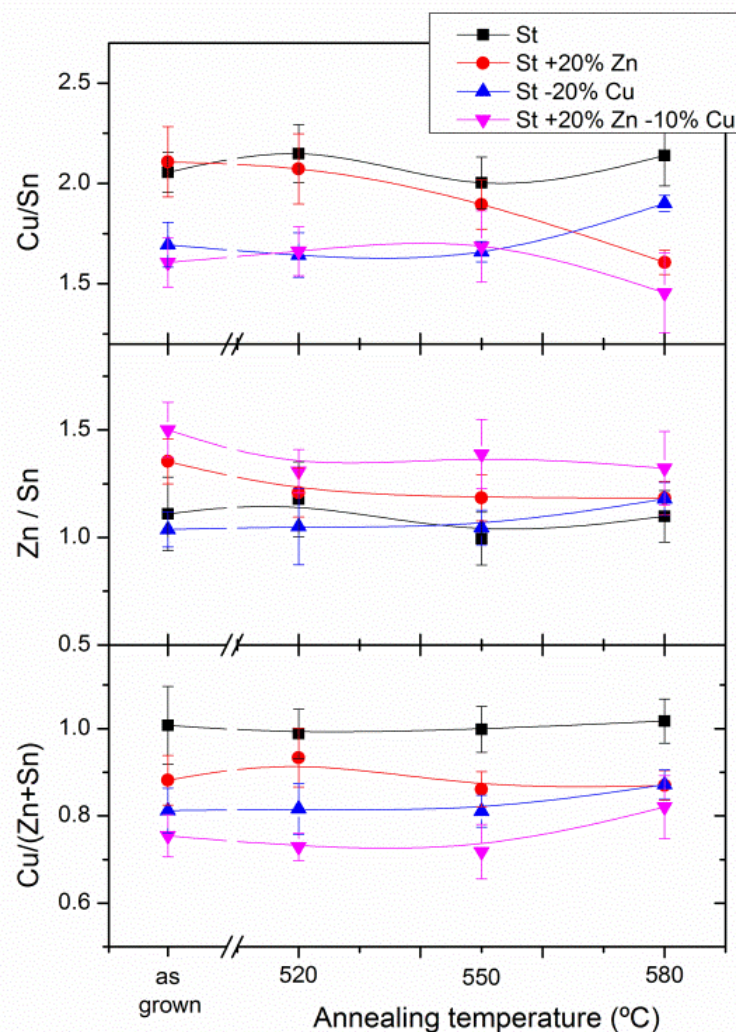
Figure 16. Compositional ratios of as sprayed and annealed samples from different concentrations in the precursor solution.

The samples were sulfurized in a three zone tubular furnace under Argon atmosphere (1 bar), using a graphite box as was described in the 2.4.2 section, containing 50mg of elemental sulfur (Alfa-Aesar, 99.995%) and 5mg of elemental tin (Alfa-Aesar, 99.999%), at 520°C, 550°C and 580°C.

After annealing and as function of the increasing sulfurization temperature, the Zn/Sn ratio converges to ~1.1-1.3 and the Cu/(Zn+Sn) to ~0.8-0.9, except for the St sample which remains Cu-stoichiometric. This demonstrates the interest of the variation of the spray precursor solution composition to obtain CZTS layers with optimized metallic ratios.

From Figure 16 it is possible to establish that through the reduction of the Cu concentration in the precursor spray solution (sample -20%Cu), the Cu/(Zn+Sn) ratio is reduced as well, such condition is sufficient to increase the Zn/Sn ratio to the optimum values[9, 104] Cu/(Zn+Sn) =0.8 – 0.9 and Zn/Sn= 1.1 – 1.2. Moreover, with solely increasing the Zn concentration in the precursor solution (sample +20%Zn), it is possible to adjust the Zn/Sn ratio, but the films still have higher Cu concentrations than the desired one. By increasing the Zn and reducing the Cu concentration in the precursor spray solution (at the same time, sample +20%Zn -20%Cu), the Zn/Sn ratio substantially increases and the Cu/(Zn+Sn)ratio decreases. This indicates both a more effective Zn incorporation and Sn deficit.

A beneficial consequence of annealing is the enhancement of the S amount in all the samples despite the metallic ratios as reported in Table 9. Compare with the S/M ratios of the as-sprayed samples in Table 8 where S/M < 0.5. In all the cases, the +20%Zn -20%Cu sample is the one that thought all the tree annealing temperatures has a better sulfur incorporation with~54% for 520°C and 550°C and 51.24% for 580°C. On the other hand this slight sulfur excess (S/M >1) can be suspected to be forming S-related unwanted faces particularly ZnS as will be later disclosed by Raman under resonant conditions, as well as for the formation of MoS_2 at the back contact, for the partial sulfurization of Mo.

Table 9. S/M ratio of samples annealed at different temperatures.

Sample	$\dfrac{S}{M}$		
	520°C	550°C	580°C
St	0.98	1.13	1.03
-10% Cu	1.12	1.13	1.02
-20% Cu	1.07	1.17	1.03
+10% Zn	1.04	1.06	1.01
+20% Zn	1.15	1.15	1.04
+10% Zn-10% Cu	1.13	1.16	1.00
+20% Zn-20% Cu	1.17	1.17	1.05

The samples sprayed using precursor solutions with different Cu and Zn concentrations results in samples not only with specific composition but also with specific electrical properties as can be noticed in Figure 17, where the resistivity of different samples is plotted vs. the annealing temperature.

All as sprayed films exhibit low electrical resistivity except for the sample who is Cu-poorer (-20%Cu). After annealing at the different temperatures, the St sample show still low resistivity. The sample sprayed from the Zn-richer solution (+20%Zn), shows also a low resistivity comparable to that for the St sample. However, lowering the Cu concentration and independent of the Zn concentration, the electrical resistivity was considerable increased at values >10^3 Ω·cm in agreement with previous published results suggesting that Cu concentration controls the electrical resistivity in CZTS[79, 105].
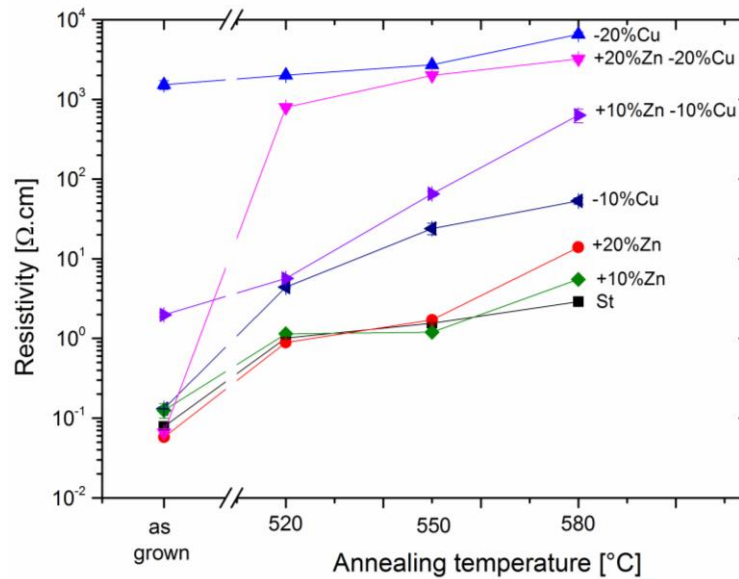
Figure 17. Resistivity variation with annealing temperature for the different samples.

Figure 18 shows the Raman spectra of five selected samples using 514nm (Figure 18a) and 325nm (Figure 18c). The spectrum of the as sprayed film exhibits a low intensity and a broad Full Width at Half Maximum (FWHM) independent of the composition (FWHM$_{A1}$ = 13cm^{-1}), indicating its low crystalline nature. Nonetheless, the main peak at 337.4cm^{-1} agrees with the A$_1$ mode of CZTS, confirming the presence of the kesterite phase in the as sprayed samples[19, 106]. As expected, after the reactive annealing under S+Sn containing atmosphere, the crystalline quality of the samples is strongly enhanced.

Observing the region corresponding to the A$_1$ mode of CZTS in detail it is evident that the spectrum from Zn-rich film is very similar to those from the St. Conversely, for Cu-poor samples and independent of the annealing temperature, a low frequency shoulder is clearly observed with an additional contribution at a frequency of about 330cm^{-1} (indicated by a blue arrow in Figure 18a). The presence of this additional contribution for the Cu-poor sample is accompanied by a red shift of the A$_1$ CZTS mode and by a deterioration of the crystalline quality (increase in the FWHM) as shown in Figure 18b. This suggests a disorder induced origin of the additional spectral contribution at about 330cm^{-1}, which would be related to the presence of disorder in the Cu sub-lattice, as a result of the Cu-poor composition of the layers. It has been shown recently, that this contribution at 330cm^{-1}, is associated to the presence of a disordered kesterite phase[107] and that such phase could be favored by the Cu poor composition of these samples[108]. In this case, the reduction of the Cu concentration on the spray solution, although improving

the electrical properties of the as grown layers, leads to the formation of a disordered phase together with the main kesterite phase.
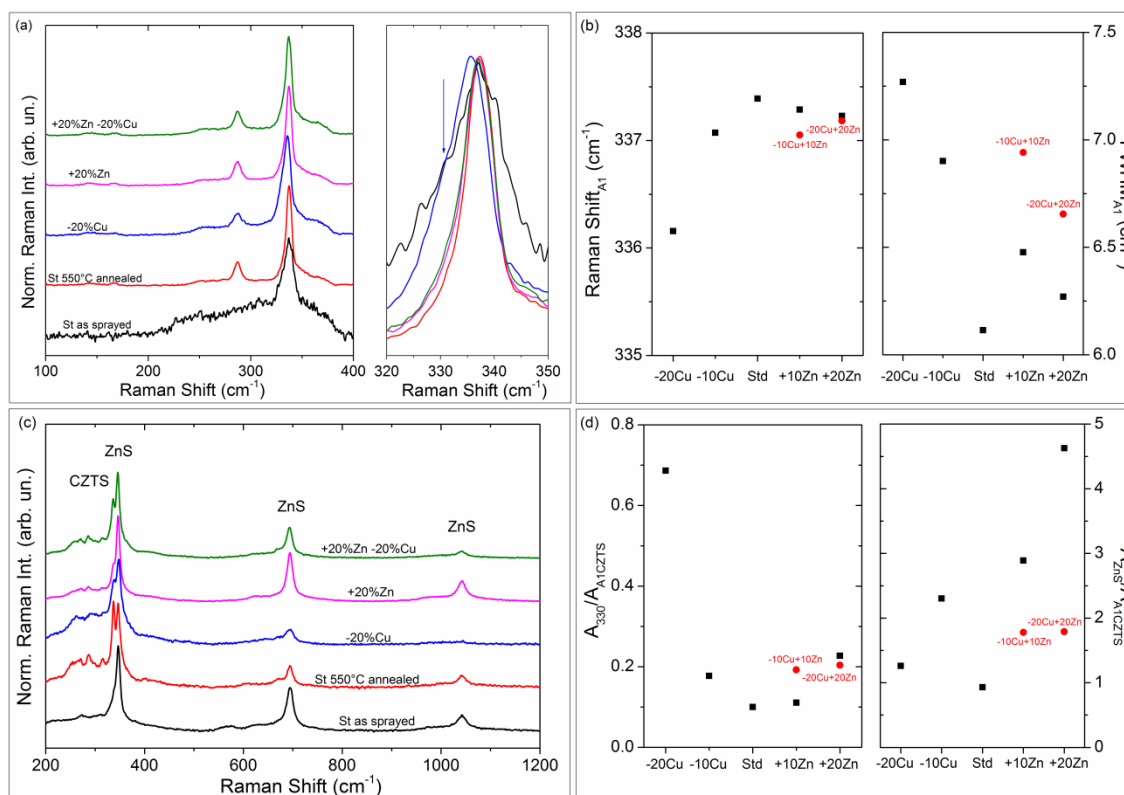
Figure 18. Surface Raman spectra of as sprayed and sulfurized (550°C) samples (a) using 514nm and (c) 325 nm excitation wavelength. (b) Raman shift and FWHM of the CZTS A_1 mode, (d) Ratios evolution of CZTS (330cm^{-1}) and the main ZnS (346cm^{-1}) over CZTS (A_1) for the different samples.

Increasing the concentration of Zn in the solution (and thus in the layers, Figure 16), partially corrects the red shift and broadening of the A_1 CZTS mode observed in the Cu-poor samples, as shown in Figure 18b. In fact, the shoulder at about 330cm^{-1} is never observed in Zn-rich films, neither in Cu-poor and Zn-rich ones when Zn excess is around 20% (sample +20%Zn -20%Cu). This suggests that a threshold excess of Zn concentration in the spray solution of +20% is required, to obtain an important improvement in the crystalline quality of the layers, as is already pondered in the Raman spectral results.

Complementary to the Raman analysis with green excitation, more detailed information about Zn-related secondary phases is obtained by using UV excitation[106]. Figure 18c shows the Raman spectra for the same samples than in Figure 18a, but measured with UV excitation. Together with the main A_1 mode of CZTS, first, second and third order peaks of ZnS at approximately 347cm^{-1}, 694cm^{-1}and 1042cm^{-1} are observed, indicating the presence of this phase in all layers[19, 106]. While both, Cu-poor and especially Zn-rich conditions seem to enhance the ZnS Raman signal with respect to the Kesterite one, films prepared from Cu-poor +Zn-rich solutions enhance the formation of CZTS over ZnS. This is not a surprising result, supporting that for the maximization of the Kesterite phase both strategies are needed: be deficient in Cu and to have excess of Zn.

Figure 18d summarizes the evolution of the relative intensity of the additional contribution at 330cm^{-1} (Figure 18a) and the main ZnS peak (Figure 18c) in relation to that of the main CZTS A_1 peak. These data demonstrate that the combination of both Cu-poor and Zn-rich conditions allows a simultaneous reduction of the disordered kesterite phase and the occurrence of ZnS as a secondary phase.

According to the obtained data, Cu-poor precursor spray solutions lead to the formation of disordered Kesterite phase, Zn-rich spray solutions lead to the preferential formation of ZnS over Kesterite, whereas the Cu-poor +Zn-rich leads to a layer with the correct electrical properties together with the minimization of the presence of secondary phases.
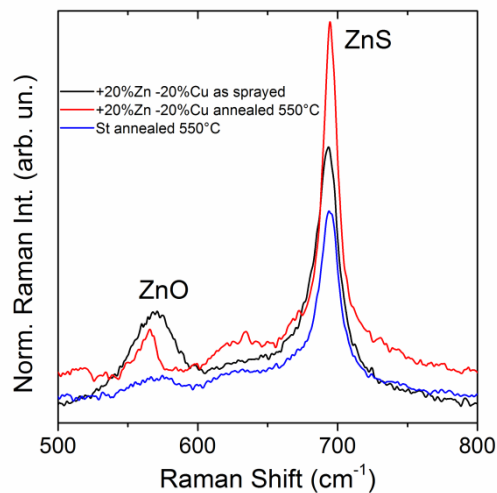
Figure 19. UV-Raman spectra of as sprayed and annealed samples showing the presence of ZnO.

Figure 19 shows the UV-Raman spectra taken in the 500–800cm^{-1} spectral region of two samples +20%Zn –20%Cu sample (550°C annealed and as sprayed) and St sample (annealed at 550°C). Two main peaks are distinguishable: at 694cm^{-1} the second order mode of ZnS[106], and at 565–569cm^{-1} a broad band assigned to the presence of ZnO in the films[109-111]. This evidences that oxidation occurs during spray pyrolysis deposition, mostly affecting the Zn incorporation.

It is important to notice that ZnO was detected in all the as grown and annealed samples. To exemplify it, here is presented the St annealed sample, no other sample has less Zn content than this sample; even after annealing, it shows the presence of ZnO. This indicates that compositional issues do not have any effect on the oxidation of the layers during growth. Furthermore, ZnO is detected in certain points of the layers suggesting a non-uniform distribution along the absorber.

After thermal treatment, the ZnO signal seems to be reduced but never completely eliminated (Figure 19), suggesting that film's oxidation is one of the main challenges to solve in spray pyrolysis technique applied to the growth of CZTS. The presence of ZnO as a contaminant in the as grown samples can have a direct impact on the optoelectronic properties of the resulting absorber by acting as recombination centers and limiting the Voc of the devices. In addition, oxidized species can also act as diffusion barriers preventing the correct grain size growth during the annealing of the samples, in agreement with the morphology study presented before

3.1.5 Air-sprayed CZTS solar cells

Figure 20 shows the cross section SEM views of different selected samples. The sample +20%Zn -20%Cu is shown as sprayed (Figure 20a) and annealed at 550°C (Figure 20d). The morphology of the as sprayed sample indicates that the sample is non crystalline independently on the precursor solution used. The reactive annealing clearly improves the crystallinity as distinguishable grains start appearing after sulfurization. Once again composition seems to have limited impact on the grain size however, increasing the sulfurization temperature from 550°C to 580° helps grain size growth. Although it is a promising result, it is clear that the annealing process still has to be further improved. The presence of an interfacial layer between the Mo and the absorber reveals the sulfurization of the Mo back contact to form MoS_2, as was predicted before by XRF.
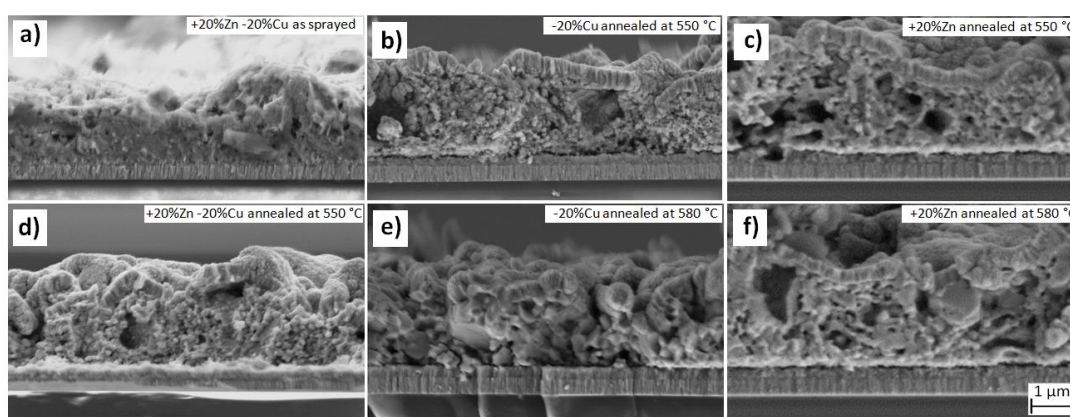
Figure 20. SEM cross section of different samples: (a) +20%Zn -20%Cu as sprayed, (b) -20%Cu annealed at 550 °C, (c) +20%Zn annealed at 550 °C, (d) +20%Zn -20%Cu annealed at 550 °C, (e) -20%Cu annealed at 580 °C, (f) +20%Zn annealed at 580 °C.

In close agreement with the electrical characterization presented in Figure 17, the best results were obtained for the Cu-poorer samples, called +20%Zn-20%Cu and -20%Cu annealed at 580°C. In Figure 21 the J–V curves of the best devices obtained are presented, with conversion efficiencies of 0.45% and 0.49%. Analyzing the optoelectronic parameters of the devices, it is evident that major problems come from the low shunt resistance (R_{sh}) which leads to low open circuit voltage (Voc) and the consequent deterioration of F.F. and efficiency. The presence of these effects in samples with absorber composition close to those used in higher efficiency cells suggests that compositional issues are not the main origin of the low obtained values of Voc. In the case of Cu-poor samples, the potential presence of a ternary CTS phase could counts for its low Voc. On the other hand, even if the films are formed by small grains after thermal annealing, similar grain sizes have been reported[108] with cells having efficiencies of about 3%. This strongly suggests the involvement of an additional feature leading to the deterioration of the optoelectronic characteristics of the cells.

At the moment of publication of the here presented results[61], the 8.4% world record efficiency[7] for CZTS-based solar cells was only known in between the *top ten notable exceptions[6];* at that time, Kesterite working devices were not yet spread in the world's PV

laboratories. Today, the best CZTS-based solar cell, listed in between the *top twelve exceptions*[8] has a reported efficiency of 8.5%. It shows the high degree of difficulty that working on pure-sulfur Kesterite devices has; in the next chapter the research will be on the direction of CZTSSe-based solar cells.
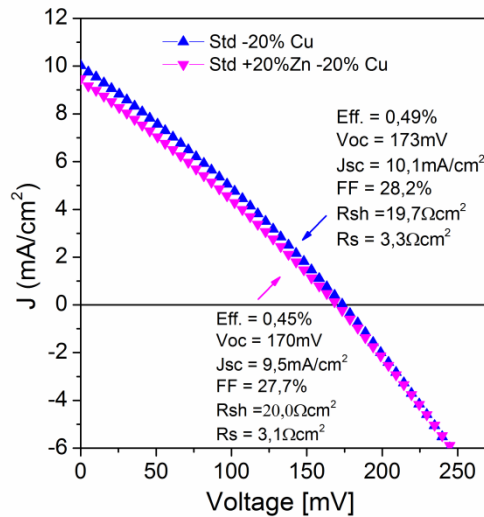
Figure 21 Illuminated J-V curves and optoelectronic parameters of the best cells obtained.

In summary, the optimization of the composition of pure sulfur Kesterite films grown by SP was presented in this section. We show that for obtaining photovoltaic grade films, i.e. with the adequate morphological, structural and electrical properties, both, Cu-poor and Zn-rich starting spray solutions are required. Imposing only Cu-poor conditions, and although the electrical properties of the obtained films are the correct, the formation of disordered CTS and/or CZTS phases is observed, explaining the red shift and broadening of the main A1 CZTS Raman peak and the appearance of an additional band at lower frequencies. Additionally, imposing only Zn-rich conditions the formation of low resistivity films with high ZnS binary phase concentration is obtained.

3.2 Ar and Ar-H$_2$ as carrier gas

This section is partially based on the publication: Espindola-Rodriguez, M. et al. Pneumatically sprayed Cu$_2$ZnSnS$_4$ films under Ar and Ar–H$_2$ atmosphere. Journal of Physics D: Applied Physics **47**, 245101 (2014).

As mentioned in the chapter 2 the SP set up used in this thesis, has the capability of working under controlled atmospheres; it allows the use of a specific carrier gas after filling the SP chamber with the same specific gas; to a pressure slightly above the atmospheric pressure (1030mbar).

So, it is possible to affirm that the films were grown either in an inert or reducing atmosphere when Ar or Ar-H$_2$ is used as carrier gas and atmosphere; aiming to eliminate the oxygen present when spraying in open atmosphere as in the classical spray pyrolysis configurations; that uses in addition air as carrier gas. It makes possible to guarantee that the films are grown under controlled atmosphere as well as that they were cooled down in a controlled almost oxygen-free atmosphere; this is a sometimes carefree time of the spray-deposited films. It was a worldwide new concept at the time of pushing the results here presented[57] as the few reports shows. It is directly related to the complexity of managing all the parameters involved in the pyrolysis process to obtain device-grade films nevertheless the world interest in this technique is increasing.

In the previous section it was shown that, using air as carrier gas, or in other words spraying in an oxygen-containing atmosphere, there is low sulfur incorporation on the films as well as oxide contaminant phases on the as sprayed samples. The presence of these oxides has been shown to be detrimental for the solar cell characteristics. It is the reason why after SP parameters optimization for the use of Ar or Ar-H$_2$, thin films with different compositions were prepared and thermally annealed to investigate its compositional and physical properties and its performance as absorber layers in CZTS-based solar cells. The films were sprayed following the substrate temperature profile of Figure 13.

When the growing time finishes, the sample's temperature of the sample could increase (if gas flux is stopped) to reacting temperatures due to thermal inertia, as shown in Figure 12b (inherent of the commonly used metallic substrate holders). Or, if the SP chamber is not kept at over pressure (1030mbar), air can easily get in contaminating the inner atmosphere with oxygen as well as oxidize the still hot sprayed sample.

3.2.1 Compositional optimization of Ar and Ar-H$_2$ sprayed CZTS films

Because of the effect of an inert carrier gas in films' composition was still unknown; it was decided to spray from precursor solutions with different metal concentrations as in the previous section. Always keeping in mind to obtain Cu-poor and Zn-rich films, that are characteristic of the device-grade absorbers. Cu$_2$ZnSnS$_4$ thin films were deposited onto soda-lime glass (SLG) and Mo-coated SLG substrates using Ar and Ar-H$_2$ as carrier gas.

Using $C^{II}C$, ZAc, $T^{IV}C$ and TU as precursors in a solution of 100% 18MΩ deionized water, the concentration of the precursors was 9mM, 4.5mM, 4.5mM and 50mM, respectively.

Cu-poor dissolutions (Cu1, Cu2) were obtained by reducing the molar concentration of the Cu precursor, and Zn-rich solutions (Zn1, Zn2) were prepared increasing the concentration of the respective precursor, as shown in Table 10. The metallic ratios (deduced from the molar concentration of the different species) in the precursor solutions are shown.

From the experience gained in the previous section, this time only Cu-poor *plus* Zn-rich combinations were tried avoiding the use of solutions *only* Zn-rich. An additional intermediate concentration were also tried, it is the Cu-poor +Zn-richer (see Table 7 to compare). The solutions were prepared as explained in the previous section.

Table 10. Summary of the precursor solutions used.

Solution Name	Solution concentration		Solution ratios				Comments
	Cu [mM]	Zn [mM]	$\dfrac{Cu}{Zn+Sn}$	$\dfrac{Zn}{Sn}$	$\dfrac{Cu}{Zn}$	$\dfrac{Cu}{Sn}$	
Std	9	4.5	1.00	1.00	2.00	2.00	Stoichiometric
Cu1-Zn1	8.1	4.95	0.86	1.10	1.64	1.80	Cu poor, Zn rich
Cu2-Zn1	7.2	4.95	0.76	1.10	1.45	1.60	Cu poorer
Cu1-Zn2	8.1	5.40	0.82	1.20	1.50	1.80	Cu poor, Zn richer
Cu2-Zn2	7.2	5.40	0.73	1.20	1.33	1.60	Cu poorer, Zn richer

In order to grow a film, the spray chamber were evacuated and filled with the desired gas. After that, the temperature controller was powered on in order to allow the substrate heater to heat the substrate up under a controlled atmosphere. A pressure of 2bar of compressed Ar or Ar-H_2 (H_2 5% by volume) was used as the carrier gas, using a dissolution flow rate of 3mL/min. The carrier gas used was the same than the one used to fill the chamber. When the growing time was over, to protect the still hot films from possible oxidation or adsorption, samples were kept inside the spray chamber under a flow of Ar or Ar-H_2 until the sample temperature was below 70 °C.

3.2.2 Sulfurization of Ar and Ar-H$_2$ -sprayed CZTS films: properties

To know the impact of the thermal annealing, two different annealing temperatures were used: 550°C and 580°C both during 30 minutes, the last one greatly improves the crystallinity, allowing for a better incorporation of Sn in the films.

It was observed that the molar composition of the dissolutions has a direct effect in the atomic composition of the films, as expected. We have also seen that even a concentration change as small as 5% of any of the metallic precursors in solution can be detected by XRF in the as sprayed films.

Samples were named after the gas and the solution's composition used to spray them, as shown in Table 11. The resulting metallic ratios of as sprayed and 580°C annealed samples are shown in Table 11.

Table 11. Metallic ratios of as sprayed and 580°C annealed samples.

Sample Name	As Grown				Annealed at 580ºC			
	$\dfrac{Cu}{Sn+Zn}$	$\dfrac{Zn}{Sn}$	$\dfrac{Cu}{Zn}$	$\dfrac{S}{M}$	$\dfrac{Cu}{Sn+Zn}$	$\dfrac{Zn}{Sn}$	$\dfrac{Cu}{Zn}$	$\dfrac{S}{M}$
Ar-Std	1.12	1.15	2.07	0.86	1.03	1.06	2.02	1.30
Ar-Cu1-Zn1	0.88	1.16	1.64	0.88	0.79	1.01	1.59	1.08
Ar-Cu2-Zn1	0.75	1.17	1.42	0.80	0.75	1.20	1.38	1.12
Ar-Cu1-Zn2	0.83	1.33	1.46	0.77	0.85	1.22	1.57	1.16
ArH-Cu1-Zn2	0.84	1.22	1.53	1.01	0.87	1.28	1.54	1.19
Ar-Cu2-Zn2	0.78	1.34	1.37	0.80	0.80	1.17	1.49	1.12
ArH-Cu2-Zn2	0.68	1.58	1.12	1.08	0.64	1.49	1.08	1.15

In the Ar-sprayed films, the Cu/(Zn+Sn) and Zn/Sn ratios are higher than those corresponding to the starting dissolutions (Table 10 and Table 11). This suggests that some Sn is lost during the spraying process because of the Cu/Zn ratio of the as-grown samples are very close to those of the starting dissolutions, meaning the same proportion of Cu and Zn added in the dissolution was then deposited into the film. This demonstrates that the amount of Cu and Zn are well preserved during the Ar-spraying process.

Concerning to use of Ar-H$_2$ as carrier gas we first observed, that the behaviour of the composition when using Ar-H$_2$ as carrier gas is different than when using Ar. Table 11 shows that even when using the same composition of dissolution if the carrier gas is changed, then a different composition results. It states that the carrier gas and atmosphere are in fact spray parameters because they define and determine the performance of the spray system having a direct effect in the main characteristic of the sprayed films: the composition. As a parameter, the compositional influence of the carrier gas has to be subjected to optimization (in terms of the concentration of the dissolution used) to make it

possible to reach the target ratios Cu/(Zn+Sn) = 0.8 and Zn/Sn ~ 1.1 reported as optimums[9, 25, 104].

In the following, annealed films means anneal *plus* 10 minutes dip in NaCl 1M just before placing them in the furnace. Table 11 also shows the compositional ratios of the films annealed at 580 °C. After 10 min dip in NaCl 1M, the initial variations of Cu and Zn from the starting precursors are well preserved after annealing. From this table it is clear that in order to reach the values of the target ratios, both Cu-poor and Zn-rich starting dissolution conditions are required. Specific concentrations of Cu and Zn in solution are needed for each carrier gas.

In the case of Ar sprayed films the best approach to the target ratios was obtained when using the Cu2-Zn2 composition (Ar-Cu2-Zn2 sample) and in the case of Ar-H$_2$ it is when using the Cu1-Zn2 composition (ArH-Cu1-Zn2 sample).

The top morphology of the as sprayed films are seen in Figure 22a, and remains almost like the one obtained using air as carrier gas, showing a near amorphous-like nature independently of the composition of the starting dissolution and carrier gas used. The insert in Figure 22a shows a typical cross section of the as sprayed sample; no grains are distinguished, evidencing some voids that disappear after the one step sulfurization.
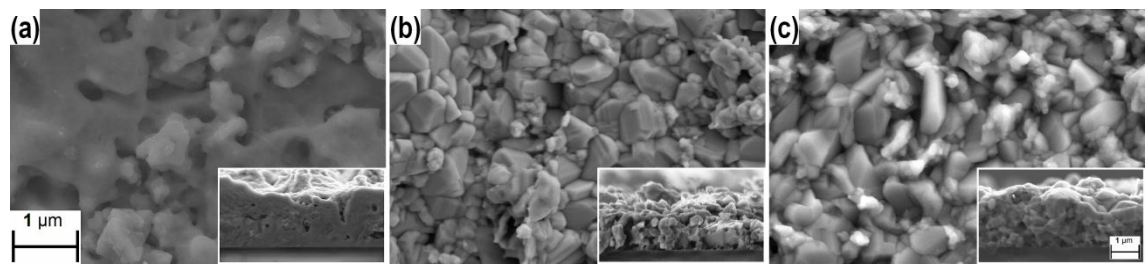
Figure 22. SEM images of (a) typical as sprayed sample, (b) Ar-Cu2-Zn2 annealed sample at 580 °C and (c) ArH-Cu1-Zn2 annealed sample at 580 °C. Insets show cross section images respectively.

In all cases, compared with air-sprayed samples (Figure 20), a noticeable improvement in crystallinity and grain size is observed after annealing. A top view of Ar-Cu2-Zn2 sample annealed at 580 °C in the presence of elemental powders of S and Sn is shown in Figure 22b. At this annealing temperature a compact layer results, formed by facets showing grains up to ~200 nm in size and free of amorphous-like zones revealed by the cross section insert in the same figure.

The ArH-Cu1-Zn2 sample (Figure 22c) is also a compact film showing less sharpened grains and smaller in size than those of the Ar sprayed films. For both carrier gases, the grain size is still lower than that generally accepted as suitable for high efficiency devices, in the order of microns. The mayor problem, (evident in the SEM pictures) inherent to this deposition technique is the surface roughness, that is higher for the spray pyrolysis technique than for PVD deposition. That spray-related roughness is detrimental for the p-n junction formation summing an extra challenge to the Kesterite films obtained by this deposition technique.

One improvement to remark after the use of Ar as carrier gas and atmosphere, is the better incorporation of sulfur in the as-sprayed films with S/M = 0.8 (Ar-Cu2-Zn2), which corresponds to a sulfur incorporation about 13% higher than those previously reported on our as-sprayed films using air as the carrier gas[61]. In this sense, the use of Ar-H$_2$ improves even more the incorporation of sulfur in the as grown samples resulting in a S/M = 1.01 (ArH-Cu1-Zn2).

The use of a controlled atmosphere enhances sulfur incorporation by decreasing the formation probability of volatile S-O species like SO$_2$. The next step could be to reduce the oxygen presence to the minimum by using other polar solvents instead of, with a lower boiling point and with the shorter carbon chain as possible such as CH$_3$-OH or CH$_3$-CH$_2$-OH to avoid as much as possible carbon contamination.

The enhanced sulfur incorporation is the first evidence of the positive effect of spraying in a controlled atmosphere favouring the formation of Kesterite right from the spraying period and not only during annealing time. The second is the bigger grain size obtained after annealing using the same conditions used for the air-sprayed films in the previous section.

In order to evaluate the band gap energy, spectral transmittance (T$_\lambda$) and reflectance (R$_\lambda$) of the samples grown on glass substrates were measured. The optical band gap energy can be estimated from the linear extrapolation of the plot $(\alpha h\nu)^2$ versus $h\nu$ with the $h\nu$-axis[112, 113]. Figure 23 shows the plots of $(\alpha h\nu)^2$ versus $h\nu$ of Ar-Cu2-Zn2 and ArH-Cu1-Zn2 samples. As sprayed samples (squares) showed an optical band gap value of 1.68 eV (sample Ar-Cu2-Zn2) and 1.66 eV (sample ArH-Cu1-Zn2), that agrees with the direct optical bad gap of CZTS thin films as reported by both Kumar[113] *et al.* and Katagiri[25] *et al.,* the former one in films obtained also by spray pyrolysis.
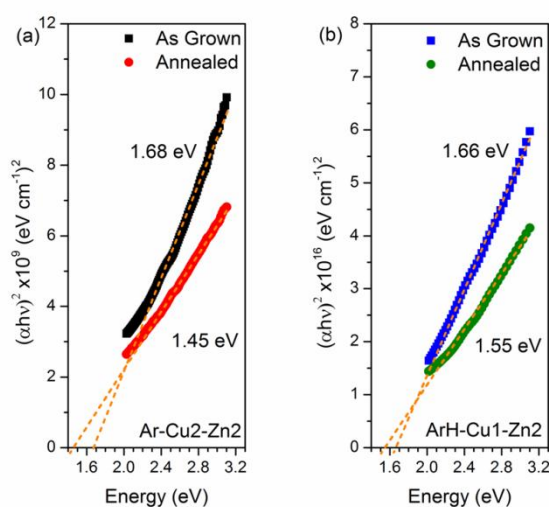
Figure 23. Optical band gap energy given by (αhν)² vs. photon energy to-cero-extrapolation of as-grown (■) and 580°C annealed (●) samples. (a) Ar-Cu2-Zn2 (b) ArH-Cu1-Zn2.

After annealing, both films showed an improved optical band gap; 1.45 eV for the Ar-Cu2-Zn2 sample and 1.55 eV for the ArH-Cu1-Zn2 sample. The first well matches with the pursued bad gap value for Kesterite absorbers, the second is in a reasonable adequate value taking into account the composition of the Ar-H$_2$ sprayed films need to be optimized (Table 11).

Thought the optical properties it is not possible to determine the presence or not (neither the amount) of binary or ternary phases formed during the spraying or annealing processes, but it is useful to determine the global behaviour of absorber materials in the part of the electromagnetic spectrum of interest, in this case, the visible region.

The presence of Cu$_x$S, in as grown samples will be disclosed later by Raman scattering measurements giving first evidence on the formation of Cu$_x$S (Eg = 1.2-1.7 eV, typically p-type) secondary phases in the as-grown samples and by XRD in the annealed ones. The presence of these secondary phases is enhanced in the ArH-Cu1-Zn2 sample that was sprayed from a precursor solution with higher Cu concentration. This suggests an incomplete reaction of the precursors for the given substrate temperature, even when its composition is Cu-poor like

The presence of ZnS (Eg = 3.7-3.8 eV, typically n-type) will be also evidenced by UV Raman scattering showing a reduced intensity after annealing, suggesting that the annealing process assists the partial reaction between Cu-S$_{(s)}$, ZnS$_{(s)}$ and SnS$_{2(g)}$ (the last one from the annealing atmosphere), leading to a decrease in the presence of secondary phases in annealed films. That all is globally measured by the T$_\lambda$, and R$_\lambda$ experiments; that would help to understand the high Eg values for as-grown samples and for those having compositions that favours some of this unwanted phases. The error in the estimation of the optical band gap energy is estimated about ± 0.03 eV.

In order to investigate the presence of Kesterite and possible secondary or ternary compounds in selected 580°C annealed Ar- and Ar-H$_2$-sprayed films, the θ-2θ XRD patterns were recorded and are shown in Figure 24. The corresponding XRD patterns of both samples show a perfect match with the sulfur kesterite reference pattern (PDF: 26-0575). The minor reflexions (002), (101) and (110), below 2θ = 24° that unambiguously belong to Kesterite are clearly visible as well as the (103) at 29.69°.

Presumably Cu$_2$SnS$_3$ (PDF: 27-0198), ZnS (PDF: 05-0566), SnS (PDF: 39-0354), Cu$_2$S (PDF: 33-0490), and MoS$_2$ (PDF: 73-1508) are present in the films, but the different phases are not discernible with this type of characterization. As it is known, XRD cannot be used to unambiguously identify ZnS nor CTS even if half of the sample consist of a secondary phase[114]. As a way out, multiple wavelengths Raman analysis suing visible and UV excitation is useful to distinguish ZnS from Kesterite.
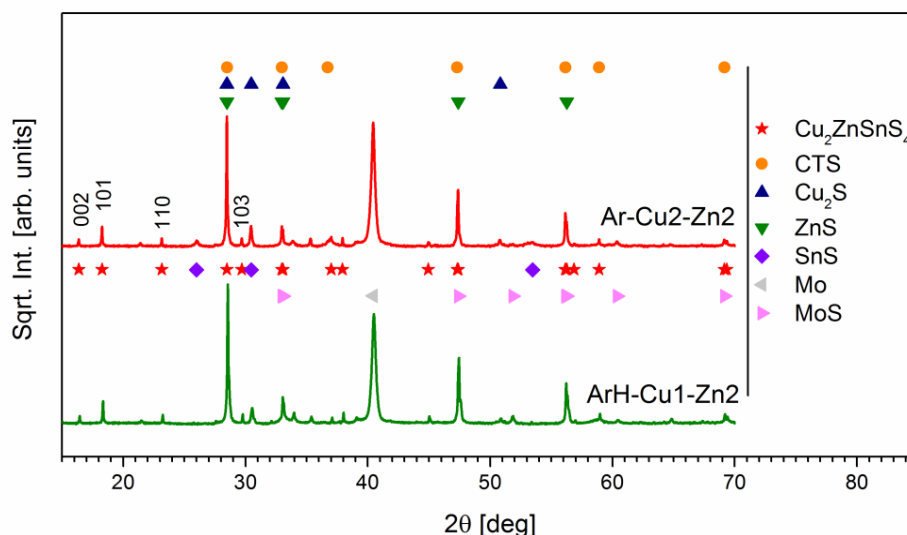
**Figure 24. XRD pattern of Ar-Cu2-Zn2 (top) and
ArH-Cu1-Zn2 (bottom) after annealing.**

To better assess the secondary phases identification, complementary Raman spectroscopy was used in the same samples presented in Figure 24. Using two excitation wavelengths, the results are shown in Figure 25; the spectra covering the frequency region 200-550cm^{-1} were measured with 514nm excitation wavelength (green); the spectra covering the frequency region 200-800cm^{-1} were measured with 325nm excitation wavelength (UV) in as sprayed (Figure 25a) and annealed samples at 580°C (Figure 25b).

The spectra at 200-550cm^{-1}, (λ = 514nm) of both as-sprayed samples (Figure 25a) is characterized by the presence of a broad peak at about 337cm^{-1}, which has been identified with the main A^1 symmetry mode from the kesterite CZTS phase[107]. The Cu$_x$S phases (x ≤ 1.8), which are characterized by a main peak[115] at 475 cm^{-1} are present only in the surface of the as sprayed samples. The ternary Cu-Sn-S compounds cannot be confirmed, nor discarded, because their main Raman peaks at 290, 317 and 352cm^{-1} are close to those characteristic of both CZTS and ZnS phases[80, 116].

In spite of the imposed inert atmosphere used during the spraying process, the spectra measured from the as sprayed samples (Figure 25a) with UV excitation wavelength ((λ = 325nm) shows a small peak at about 573cm^{-1} which has been identified with the A$_1$ ZnO Raman mode[109-111]. After annealing (Figure 25b) and given the pre-resonant excitation used, no evidence of ZnO is observed in any of the films, no matters the composition or the gas used to spray them, supporting the XRD results suggesting the complete elimination of this detrimental phase under the applied thermal conditions. This contrasts with the behavior observed in films grown using air as the carrier gas, where the presence of ZnO persists even after reactive annealing. This shows the effectiveness of the imposed inert atmosphere and reactive Sn+S annealing processes to minimize the presence of detrimental oxidized species.
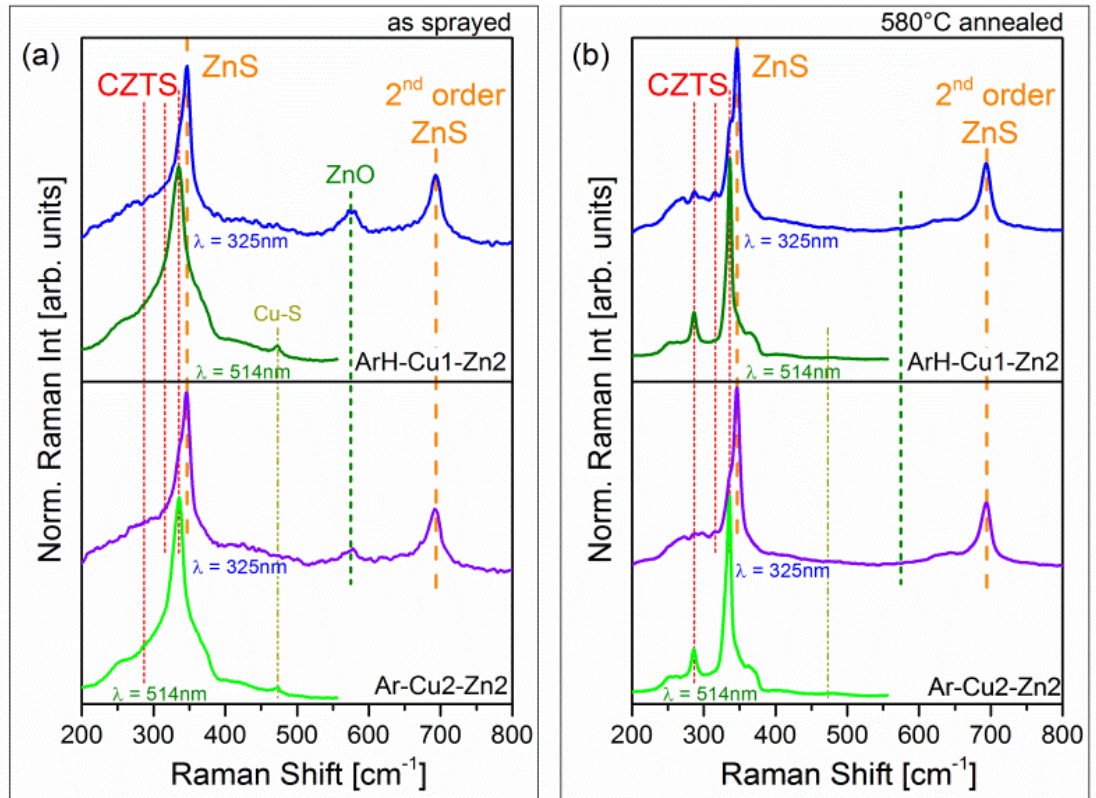
Figure 25. Raman spectra of (a) as sprayed and (b) 580°C annealed samples. The excitation wavelengths used are: green, 524nm (200-550cm^{-1}) and UV, 325nm (200-800cm^{-1}).

Annealing the films (Figure 25b, λ = 514nm) leads to a significant decrease of the Full Width at Half Maximum (FWHM) of the main A_1 (337cm^{-1}) peak, from 17.6 cm^{-1} to 8.9 cm^{-1} and from 20.8 cm^{-1} to 7.7cm^{-1}cm^{-1} for Ar-Cu2-Zn2 and ArH-Cu1-Zn2 samples respectively. After annealing, in the same spectra of both samples (λ = 514nm), also appears a second peak at around 287cm^{-1}, that is attributed to a second A symmetry mode characteristic of the kesterite phase[107] confirming the higher crystalline degree showed earlier with the XRD results.

Fitting the spectra covering the 200-550cm^{-1} region, (λ = 514nm) of the annealed samples (Figure 25b) with Lorentzian curves allows the observation of additional weaker contributions at higher frequencies at about 166, 252, 272, 353 and 366cm^{-1} that correspond to E or B symmetry modes from the CZTS kesterite phase[80, 106]. This agrees with the significant improvement in the crystallinity of the samples after the annealing process, as revealed by SEM.

By using UV excitation conditions (Figure 25, λ = 325nm), pre-resonant excitation of the main Zn-S vibrational modes are reached, greatly enhancing the sensitivity of the measurement for the detection of this phase[106]. In Figure 25 (λ = 325nm), the spectra of as-sprayed and annealed samples covering the region 200-800cm^{-1} show the presence of characteristic intense ZnS 1st/2nd order peaks of this binary compound with characteristic contributions at about 346 and 694cm^{-1}; confirming what was suggested previously by XRD.

In the annealed samples (Figure 25b, λ = 325nm) the relation between the deconvolutioned intensity of the 1st order ZnS Raman peak (at 346cm^{-1}) and the main CZTS peak (at about 337cm^{-1}) is 2.5 and 3 for Ar-Cu2-Zn2 and ArH-Cu1-Zn2 samples respectively. That means that for the ArH-sprayed sample, the deconvolutioned intensity of the main ZnS peak is 3 times higher than the intensity of the main kesterite peak for the specific wavelength used. In other words, the most intense ZnS peak corresponds to the sample with the bigger Zn/Sn ratio.

In contrast, as we reported[80] for similar samples, annealing only under S atmosphere (Figure 26) leads to a drastic FWHM increase up to 10.8cm^{-1} (8.9cm^{-1} annealing in S+Sn) which correlates with a significant worsening of the structural quality of the Kesterite phase due to a highly disordered distribution of Cu and Zn atoms[107] resulting from Sn deficiency in the samples.
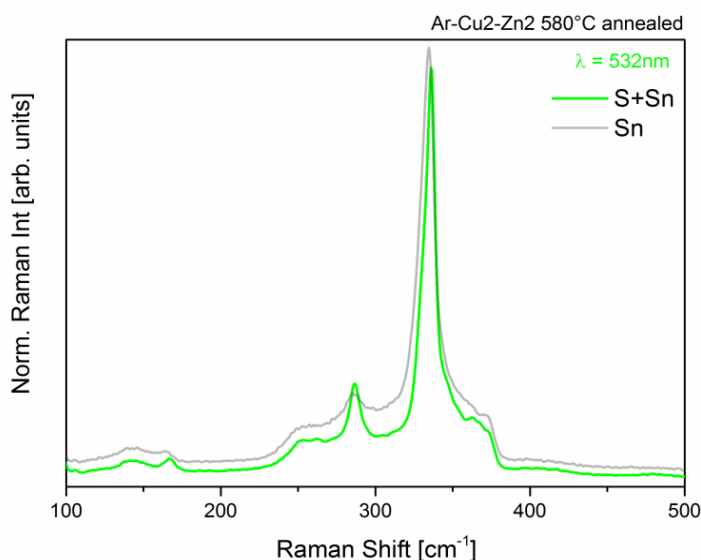
Figure 26. Ar-Cu2+Zn2 sample annealed under S+Sn and only S atmosphere.

3.2.3 Ar and Ar-H$_2$-sprayed CZTS solar cells

Solar cells were fabricated using an Ar-Cu2-Zn2 and ArH-Cu1-Zn2 absorbers; the beneficial effect of NaCl (1M) dip of the precursors just before annealing is shown in Figure 27.

The Ar-sprayed dipped sample with the optimized composition (Cu2-Zn2) showed the best optoelectronic properties as Table 12 reports. Compared to the previous section using air as carrier gas[61] this improvement is mainly due to an increase of the shunt resistance (R_{sh}), V_{oc}, and FF. This is likely related to an increase in the average grain size and a better passivation of the grain boundaries by using an Ar atmosphere, where oxidation effects are minimized. The R_{sh} and V_{oc} improvement observed in this work when using Ar, are still below the optimal reported values[9] and it could be caused, among others, by the presence of low band-gap materials such as Cu_xS or SnS_x that reduce the open circuit voltage and decrease the shunt resistance[14].

Referring to the use of ArH$_2$ as carrier gas and from the optoelectronic point of view, a great improvement was also achieved with respect to use of air as carrier gas as evidenced by a power conversion efficiency after NaCl dip of η = 0.65 %, FF = 31 %, V$_{oc}$ = 305 mV and J$_{sc}$ = 6.9 mA/cm^2. This efficiency would increase if the composition of the ArH$_2$ sprayed films were closer to the target ratios, however we limited this work to show on films and devices, the effect of changing only the carrier gas with previous optimization of the precursor solution for Ar as carrier gas.
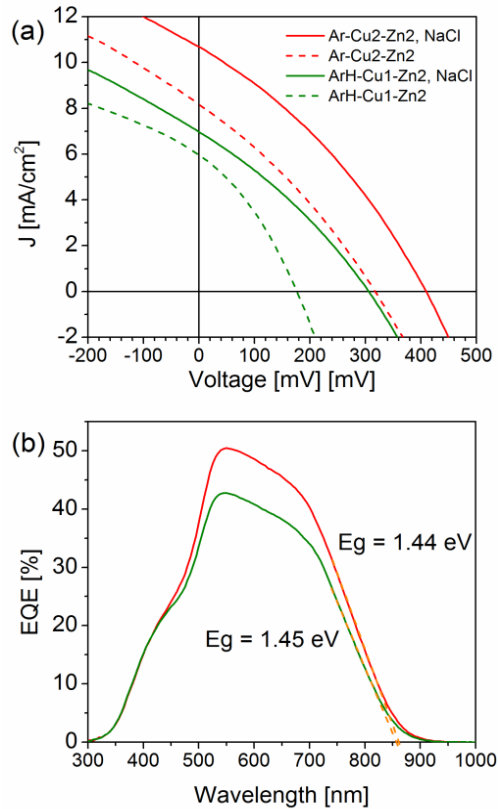
Figure 27. Optoelectronic characteristics of devices made from Ar and Ar-H2 sprayed absorbers. (a) illuminated J-V response showing the beneficial effect of NaCl dip and (b) the corresponding external quantum efficiency.

A further improvement on the V$_{oc}$ values can be obtained by the open possibility of optimizing the thermal processes to increase the grain size in the absorbers thus reducing the density of grain boundaries which in turn would help decrease the density of recombination centers. Also, the low short circuit currents of the solar cells could be related to the high roughness of the absorbers.

Table 12. Optoelectronic parameters of Ar and Ar-H$_2$ sprayed solar cells.

Annealing Param.	Jsc [mA/cm^2]	Voc [mV]	FF [%]	Efficiency [%]	R$_{sh}$ [Ωcm^2]	R$_s$ [Ωcm^2]
Ar-Cu2-Zn2, NaCl	10.70	407.09	33.0	1.40	70.80	17.31
Ar-Cu2-Zn2	8.16	316.88	30.61	0.79	58.52	18.61
ArH-Cu1-Zn2, NaCl	6.96	305.87	31.0	0.65	65.0	19.0
ArH-Cu1-Zn2	5.92	176.15	33.36	0.35	58.14	10.17

Figure 6(b) shows the EQE of the mentioned solar cells. The linear extrapolation of the long wavelength region that correspond to the contribution of the bulk of the absorber to the EQE measurement, gives a band gap value of 1.44±0.01 eV and 1.45±0.01 eV respectively for Ar-Cu2Zn2 and ArH-Cu1-Zn2, in close agreement with the accepted value for CZTS, and with a maximum EQE of 50.5 % and 42.7% at 550 nm respectively. The value of the EQE falls rapidly while going to the long wavelength region showing that the absorber and the absorber-buffer interface need to be optimized. Considering that the composition of the absorbers is close to those reported for the best CZTS-based solar cells and the minimization or even absence of oxidized detrimental phases, the main limitations of the devices are likely related to the morphology of the absorber (small grain size, high surface roughness). The improvement of the thermal processes, better adapted for the characteristics of the sprayed precursors, aiming to obtain larger grains with smoother surfaces could help to the increase of the conversion efficiency. Nevertheless, the results here presented show the potential of this modification of the spray pyrolysis method to improve the optoelectronic characteristics of device-grade films synthesized using a cost effective process.

Our results show the importance to develop a completely inert route to increase the efficiencies of the devices prepared with this technology, avoiding the contamination with oxygen that takes place when using the standard configuration that involves an oxygen containing atmosphere.

3.3 Summary

The simultaneous combination of both Cu-poor and Zn rich growing conditions maximizes the formation of CZTS kesterite phase over the secondary ones, without any detrimental effect on the electrical properties of the films. Results on the preparation of devices and their optoelectronic characterization are encouraging, showing modest efficiencies mostly related to the low shunt resistance of the cells.

On the films sprayed under controlled atmospheres using Ar or Ar-H$_2$ as carrier gas, it was demonstrated that the carrier gas is real spray parameter as it modifies the composition of the films which is in turn influenced by the composition of the precursor solution. By out-of-stoichiometry variations in the precursor solution it is possible to modify the elemental Cu/(Zn+Sn) and Zn/Sn ratios, thus obtaining the desired compositional values, i.e. Cu-poor and Zn-rich composition.

ZnS is detected as the main secondary phases in the as sprayed and annealed samples, enhanced by the Zn-rich nature of the device grade films. Cu-S phases were also found in as-sprayed films when Ar or Ar-H$_2$ is used as carrier gas, even under the imposed Cu-poor conditions, and its presence was mainly related to incomplete reaction of the precursors. Annealing leads to the reaction of some of the secondary phases detected in the as-grown films: Cu-S reacts with ZnS and SnS$_2$ forming CZTS.

However, oxidation is one of the major challenges to push up the performance of the sprayed CZTS based devices. Using Air, Ar or Ar-H2 on as sprayed samples, it was observed selective oxidation of Zn phases independently on the starting solution composition; it is the main drawback in this technology.

In the case of air-sprayed films, the presence of ZnO remains even after annealing, in the case of Ar- or Ar-H$_2$ -sprayed films, no evidence of ZnO is found anymore after high temperature (580 ^{o}C) thermal annealing. It implies that the use of SP systems in controlled atmosphere face one of the main harms of the classical spray pyrolysis technique, the formation of oxide compounds.

After annealing (580 ^{o}C), the crystallinity and grain size of the air- and Ar- as sprayed films was improved as can be seen in Figure 28. The results show that the use of a S+Sn reactive atmosphere is necessary during the annealing process to improve the crystalline quality and composition of the films.
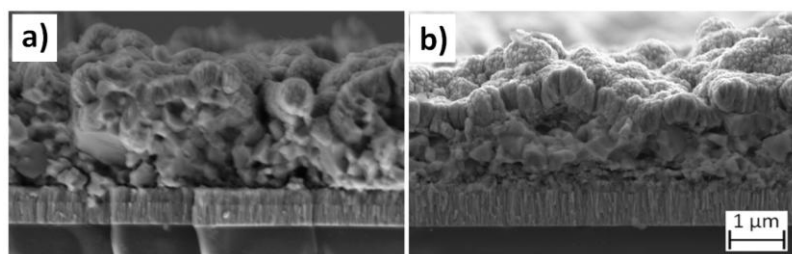
Figure 28. SEM cross section of (a) air-sprayed and (b) Ar-sprayed solar cells from +20%Zn -20%Cu precursor solution.

Nevertheless, the grain size and roughness of the surface are still far from the optimal morphology of CZTS films grown by other techniques. In a first optimization, we report a 1.4 % efficiency device (Figure 28b) that is at free of scare elements. Improvement of the optoelectronic properties of these absorbers is linked to the optimization of the reactive annealing to achieve larger grains and smother surfaces for better interfaces.

4 FROM ALCOHOL-BASED SOLUTION TO SPRAYED CZTSSE SOLAR CELLS

After the encouraging results obtained in the previous chapter on CZTS-based solar cells, this chapter deals with one of the most basic solution-related spray parameters; this is the *solvent* using Ar as carrier gas and atmosphere. Two different polar alcohols were tested as base solvents, ethanol and methanol.

This chapter deals also with the selenization of the CZTS as-sprayed films from alcohol-containing precursor solutions by one or two selenization steps to produce CZTSSe absorbers. The CZTSSe/CdS interface in theory should be completely planar but the intrinsic surface roughness of the sprayed films keeps the cells away from this theory. To smooth the as-sprayed surface and improve the interface, the effective use of a Br_2-MeOH wet chemical etching is presented.

With the aim of knowing the most appropriate solvent, etching conditions and selenization parameters in terms of power conversion efficiency, CZTSSe-based solar cells were produced from ethanol- and methanol-sprayed CZTS films. After all, one step selenization of pre-etched methanol-sprayed films showed to be more appropriate.

4.1 Ethanol-based solution

When preparing a solution, the goal is to prepare a homogeneous stable solution within the necessary cation species that will be later sprayed on the preheated substrate.

The solution for SP is a multicomponent system; it has to be considered not only the solubility of the precursors in the solvent but also their mutual solubility; the solvent must facilitate that. For example in the case of using alcohol + water as solvent, and Zinc acetate as Zinc precursor, the Zn salts have to be first dissolved in water; but there is a maximum

percentage (v/v) of alcohol that can be added to the solution before it precipitate. The best results in this thesis were obtained using Zn Acetate and are the ones that in the subsequent sections will be presented.

The solution life time is determined by the solvent, precursors, its concentrations and the temperature of the solution; an acid (pH = 2) precursor spray solution can last for days if the metallic precursors are chlorides in a alcohol + water (50%, v/v) however, such low pH values erodes the metallic nozzle; it implies that a balance has to be found between the system preservation, solution stability and solution life time.

The reaction rate of precursors in solution and their reaction pathway are defined by the solvent, as are the characteristics of the solvated reactant, the types of bounds that are broken or formed and the resulting products and transition-state species. They all are influenced by the solvent that plays an important role in the solution chemistry[98] but they are beyond the scope of this thesis.

The interest in using alcohols as base solvents is that they have reduced boiling point, density and surface tension compared with water. When spraying, it helps to reduce the drop size, with fasters the vaporization of solvent guiding to the precipitation of precursors within the droplet before they reach the substrate, in order to experience a CVD-like process from which the sprayed film is formed. Table 13 compares the boiling point, density[117], viscosity[117] and surface tension[118] of different solvents at room temperature.

Table 13. Properties of different solvents at room temperature.

Solvent	Chemical formula	Boiling Point [°C]	Density [g·cm⁻³]	Viscosity [Pa·s]	Surface tension [mN·m⁻¹]
Methanol	CH_3-OH	65	0.78720	0.545	22.70
Ethanol	CH_3-CH_2-OH	79	0.78546	1.082	22.10
Water	H-O-H	100	0.99705	0.890	72.80

In order to study the influence of ethanol in the as-sprayed films, it was first prepared a H_2O + ethanol (50%, v/v) solution to obtain the appropriate Cu-poor Zn-rich composition of the device grade films onto Mo coated substrates using metal chlorides and thiourea. This change of solvent implies a change in the spray process thus an optimization of the deposition parameters was needed. Together with the concentration of the precursors in the solution using a new solvent, the substrate temperature is the second most important spray parameter affecting the spray deposition process and the final composition of the as-sprayed films; consequently, its optimization and control is essential during the spray process time.

4.1.1 Substrate temperature

The substrate temperature profile (as was mentioned in the precedent chapters) is influenced by multiple parameters such as: substrate-nozzle distance, solvent, solution

flux, gas pressure, the moment when the spray process starts and finishes, the substrate heating conditions (with or without a gas flux), etc. All those aside parameters ought to be taken in to account to optimize the films composition.

With the intention of find the most appropriate substrate temperature, tree different values were used to spray films (235°C, 250°C, 270°C); in all cases Ar was used as carrier gas. The optimized temperature profile used in this chapter is the optimized one presented in the previous chapter (235°C).

As a dynamic system, the hot substrate has the tendency to cool down by exchanging heat with the medium; as higher the temperature as more difficult is to keep it stable. For high substrate temperatures, after some seconds of the spray-on period the chamber is filled with vapor of solvent that makes denser the inner chamber atmosphere, making it difficult for the incoming drops to freely approximate to the substrate. Because of that, more Ar pressure is needed (2 bar) to provide the drops with enough energy to traverse the dense atmosphere and approach the substrate. But the increased Ar pressure cools faster the substrate making it necessary for the control system to allow more power to the heating system; SP is a dynamic system with strongly codependent variables.

When the substrate temperature is too high, the solvent of most of the drops vaporizes too fast, it results in dusty films with aggregates (micrometric spheres that once were drops) in the top and volume of the films. The formation of this micro spheres and rough surfaces has been reported by different authors[59, 81, 95, 99, 119-121]. This typical spray morphology was logically believed to be inappropriate for some applications, in this thesis we confirm that. All the authors agree that the higher the deposition temperature the higher both: the crystallinity and the roughness of the films.

As the substrate temperature decreases, first it is easier to control it, and second the films contain only inevitable (given the nozzle) aggregates result of the early precipitation of the salts within the small drops. When those aggregates (in spherical shape) reach the substrate, they are slowly covered by the growing film, product of the metal precursors in the drops that are experiencing a CVD-like process nearby the substrate. The spraying rate needs to be carefully controlled to allow sufficient time for chlorine to evaporate in the form of HCl[99, 122].

Figure 29 shows top SEM images of as-sprayed samples at different substrate temperatures. The sample with the highest substrate temperature at the time of growing (Figure 29a), is the one that has more aggregates on the surface, most of them are of small size (~200nm); the images are at the same magnifications and SEM conditions. The sample sprayed at lower temperature, has an almost free of aggregates surface. All sprayed films need a high temperature annealing to result into working devices thus; a lower spraying temperature was chosen to optimize the composition of the films.
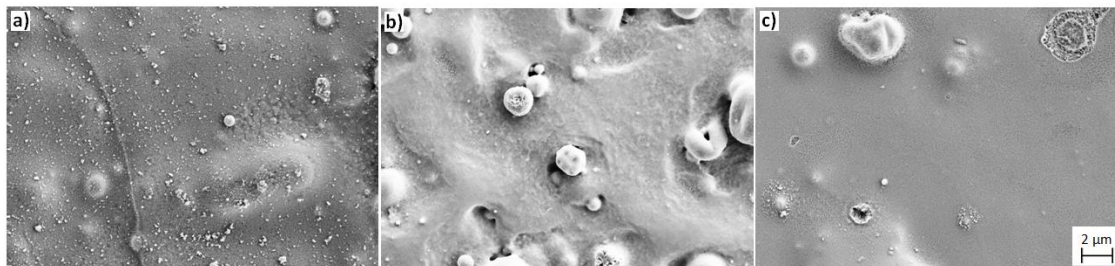
Figure 29. As sprayed samples at different substrate temperatures, (a) 270°C (b) 250°C and (c) 235°C

4.1.2 Metallic ratios optimization

An example of the metallic ratios optimization is shown in Table 14, where the substrate temperature was set to be 235°C in all cases. The films were sprayed onto Mo coated substrates using $CuCl_2.2H_2O$, $Zn(CH_3CO_2)_2$, $SnCl_4.2H_2O$ and CH_4N_5S (8mM, 5mM, 5mM and 50mM respectively, Table 14 sample A). The optimization process goes from sample A (with non-appropriate ratios) to sample E (with acceptable ratios) using H_2O + ethanol (50%, v/v) as solvent.

Table 14. Optimization of the metallic ratios in ethanol + water (50%, v/v)

Sample	Precursor solution concentration				XRF ratios on as sprayed films				
	$\dfrac{Cu}{Zn+Sn}$	$\dfrac{Zn}{Sn}$	$\dfrac{Cu}{Zn}$	$\dfrac{Cu}{Sn}$	$\dfrac{Cu}{Zn+Sn}$	$\dfrac{Zn}{Sn}$	$\dfrac{Cu}{Zn}$	$\dfrac{Cu}{Sn}$	$\dfrac{S}{M}$
A	0.80	1.00	1.60	1.60	0.66	1.28	1.20	1.51	0.78
B	0.75	1.22	1.37	1.66	0.98	1.94	1.52	2.94	0.69
C	0.77	1.08	1.48	1.60	0.81	1.87	1.28	2.37	1.84
D	0.73	1.14	1.38	1.57	0.80	1.30	1.42	1.85	1.79
E	1.03	1.57	1.69	2.65	0.90	1.19	1.67	1.98	0.86
E + Br-MeOH					0.85	1.10	1.64	1.79	1.01

The data presented in Table 14 have behind the experience gained all through the experiments exposed in the chapter 2, concerning with the optimization of the SP. Nevertheless, changing one single parameter in the system has to be accompanied of plenty of experimentation time.

As the films are not free of segregates, Figure 30 shows the SEM image of a big one on the top of the as sprayed sample E of Table 14. Table 15 shows the atm% and metallic ratios of the points shown in Figure 30. The spherical segregate shows to be slightly Cu-rich; the film (Figure 30, spectrum 2) has comparable composition than those of Table 14 sample E. After the Br_2-MeOH etching and with a cleaner surface, the composition of the sample measured by XRF is shown in the last row of Table 14.
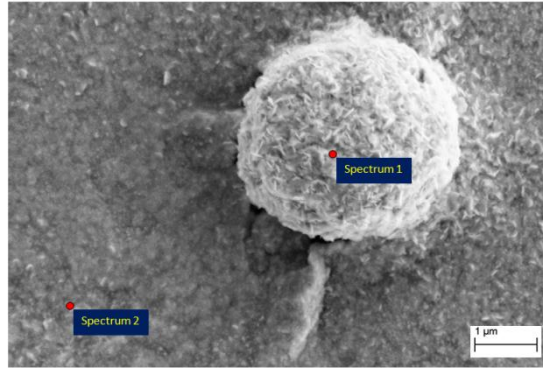
Figure 30. Top SEM view of segregate.

Table 15. EDX metallic ratios of as sprayed film

	EDX atm%				Metallic Ratios		
	Cu	Zn	Sn	S	$\dfrac{Cu}{Zn+Sn}$	$\dfrac{Zn}{Sn}$	$\dfrac{Cu}{Sn}$
Spectrum 1	28.39	13.85	12.59	45.17	1.07	1.10	2.25
Spectrum 2	22.09	12.74	11.58	53.59	0.91	1.10	1.91

4.1.3 Variation of ethanol content on the precursor solution

By using as starting point the optimized parameters of sample E in Table 14 (water + ethanol, 50% v/v) the composition and thickness of as-sprayed samples using different proportions of ethanol in the precursor solution is shown in Figure 31. High alcohol content in the precursor solution results in thinner films for the same spraying time.
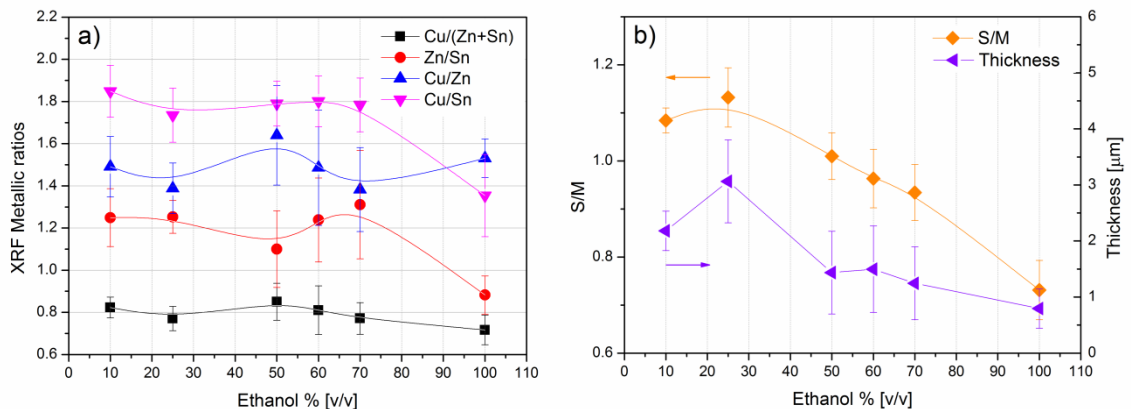
Figure 31. Composition and thickness evolution of as sprayed films with different proportions of ethanol in the precursor solution.

4.1.4 Surface roughness reduction: Br$_2$-MeOH etching

It is known that bromine solutions are efficient etchants to CZTS(e)[123] and CIGS(e)[124, 125] reducing the initial surface roughness. In this thesis as is common, the surface roughness

is shortened to roughness, a component of surface texture. Roughness plays an important role in how the surface will form interfaces; in p-n junction solar cells, the p-n interface is the most important of all the interfaces the device has. It is the reason why high roughness of absorbers is always undesirable; in theory this interface should be completely planar; sprayed thin films are far from this theory.

For sprayed CZTS thin films, the use of Br_2-MeOH etchant solution has two reasons, the first is as mentioned, reduce the surface roughness and the second is to clean the surface from the segregates. A set of comparable samples was etched in a solution containing either 0.01% (v/v) of Br_2 in Methanol (Br_2-MeOH) at room temperature. After etching, the samples were dipped in Methanol, rinsed with methanol, then dipped in deionized water and rinsed with deionized water and dried with N_2.

A relative thickness (t_{RT}) is defined to appreciate the effect of the Br_2-MeOH etching with time in the average thickness of the films.

$$t_{RT} = t_{etch}/t_o$$

Where t_o is original thickness of the films before etching and t_{etch} is the thickness of the film after etching measured by XRF. The thickness of the films after the Br_2-MeOH etching is shown in Figure 32, the thickness of the films decreases consequently with the etching time; decreases up to 25% with 180s of etching and about 15% after 120s of etching.
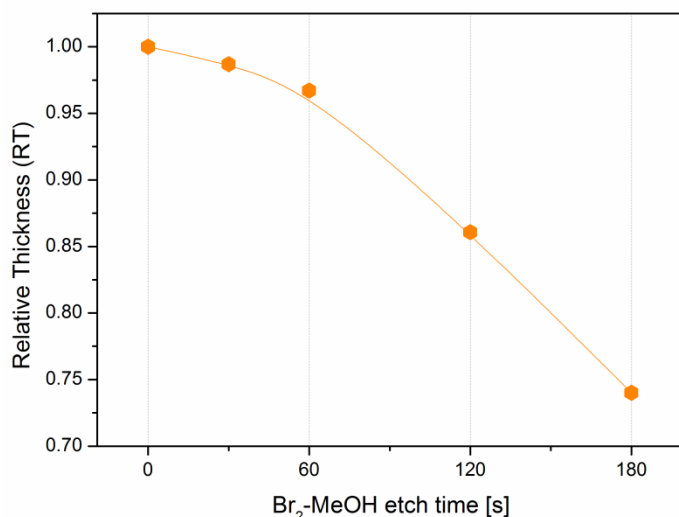
Figure 32. Thickness of as sprayed films after 0.01% of Br_2-MeOH etching.
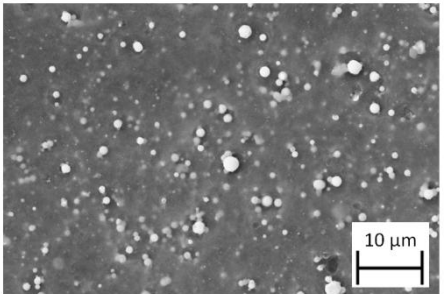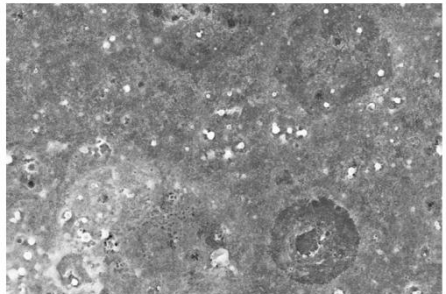
The optimum etching time is 120 seconds as for longer times the film stars to peel off however, to investigate the effect of the etching in the remaining parts of the films after long etching times, 300 seconds were tested taking the etching and samples to a boundary condition. Table 16 shows SEM top images of an as-sprayed 0.01% Br_2-MeOH etched sample for long time (300s) etching, using an acceleration voltage of 20kV of the electron gun for to penetrate deeper in the film. The images show that the precipitates are not only in the surface of the films but also below the surface (Figure 29 using 5kV also shows that)

which makes it impossible to completely remove them with this etching, however the surface is smoothed, which is the main objective of this step.

The long time etched sample in Table 16, also reveals some drop marks leaving after the spread and draying of some big drops that did not evaporate before reaching the substrate. From all the results up to here, it is stated that:

The SP films, for the examined spraying conditions, will remain holding on its surface and volume the traces of have been formed by a pneumatic spray process even after an aggressive chemical etching such as Br_2-MeOH.

Table 16. Top SEM images before and after Br-MeOH etching using 20kV

20kV	Time [s]	
Concentration [v/v]	0	300
0.010%		

A quantitative study of the surface roughness for as sprayed films etched in Br_2-MeOH is presented for the methanol-sprayed films. The XRD pattern of a as sprayed CZTS thin film sample after Br-MeOH etching is shown in Figure 33a. SnO_2 (00-041-1445), ZnO (01-074-0534), Cu_2SnS_3 (00-027-0198), Mo (00-042-1120) and Cu_2ZnSnS_4 (00-026-0575) were identified in the spectra. The oxides might have been formed during the spraying time and were not removed by the Br_2-MeOH etching as they are found not only in the surface of the films. Figure 33b shows the SEM cross section of the sample etched during 120 seconds.
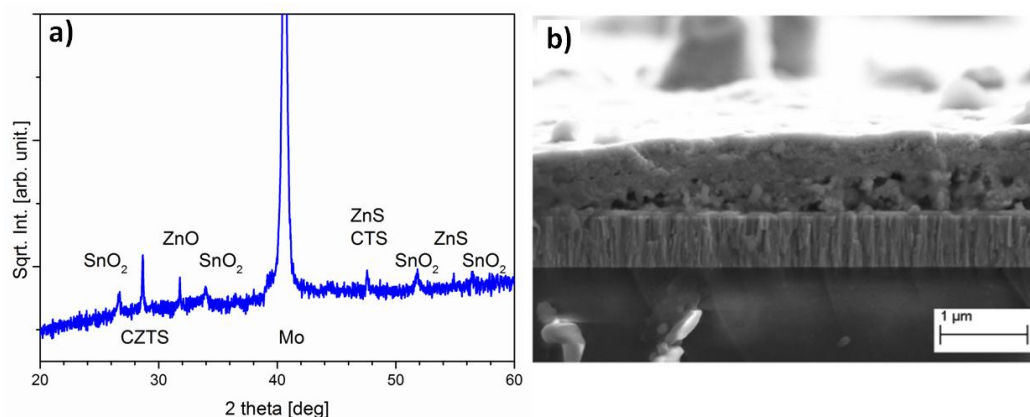
Figure 33. X-ray diffraction pattern of as sprayed CZTS sample using water + ethanol as solvent for the precursor solution.

4.1.5 CZTSSe solar cells from ethanol-based precursor solution

Recently, Na doping has been confirmed to be beneficial to CZTSSe as for CIGS. It is not totally understood the role it plays in the devices however now is know it enhances the optoelectronic characteristics of the solar cells by increasing hole density and mobility resulting in improved efficiencies. During the selenization, Na_2Se_x liquid phase has been proposed[54] to promote grain grow which is a major issue in sprayed films. Because of that, NaF was tested as Na dopant source to the sprayed CZTS films. Films of 10nm and 20nm of NaF were evaporated in the 0.01% Br_2-MeOH etched surface of the as-sprayed films prior selenization. The samples with the NaF layers in the top were selenized at 500°C and 550°C in semi closed graphite boxes containing 20 mg of elemental Se (20mg).

After selenization, to complete the solar cell devices, the samples were etched in HCl (10%, v/v) for 2 minutes at 75°C. Immediately after, a CdS film (~60nm) was deposited by chemical bath deposition, intrinsic ZnO (50 nm) and ITO (300 nm, 35 Ω/□) films were grown by pulsed DC magnetron sputtering deposition. The cross section of the resulting solar cells is shown in Figure 34.

In contrast to other solution-based deposition techniques, in this case there is not carbon layer present in the films. All the in-volume segregates have been transformed into crystalline kesterite during the selenization process.
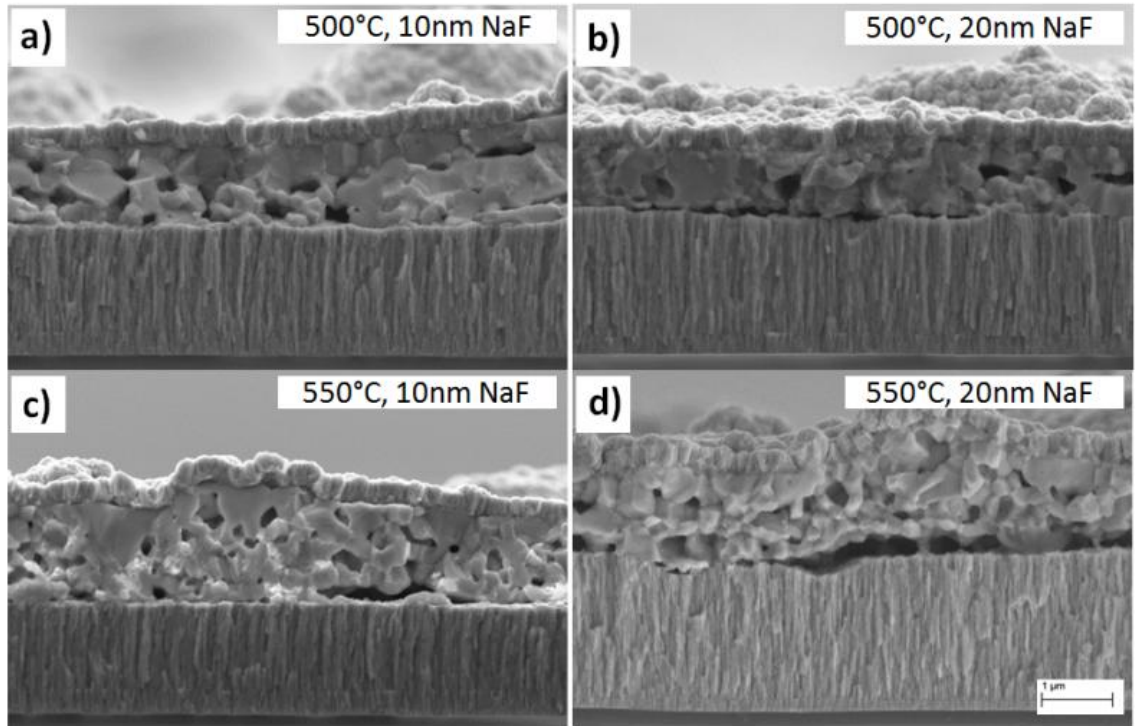
Figure 34. SEM cross section images of solar cell devices illustrating the effect of the selenization temperature and the thickness of the NaF top layer.

Figure 34a and Figure 34c compares two different selenization temperatures, 500°C and 550°C respectively using in both cases 10nm of NaF. A notable increase in grain size can be observed with respect to sprayed films annealed without Na[61, 73] were the grain size is of the order of hundreds of nanometres. The very modest J-V curves (Figure 35) and optoelectronic parameters of those devices (Table 17) are shown below.
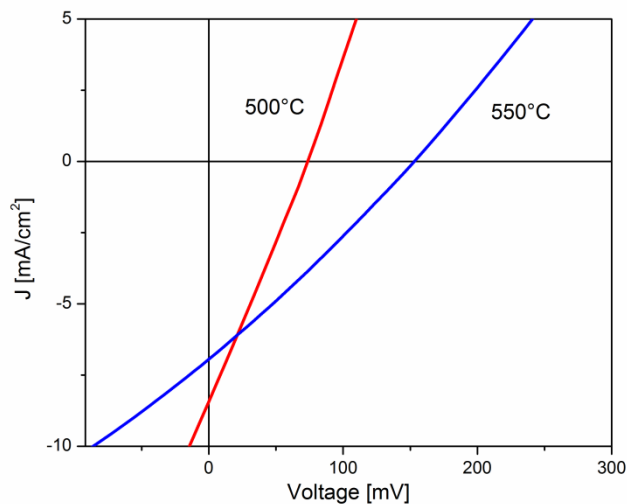
Figure 35. J-V curves of devices annealed at 500°C and 550°C.

The films annealed with 20nm of NaF resulted in non working devices maybe, due to the over selenization of the Mo back contact as a result of the enhanced reactivity of Se when forming Na_2Se_x[54].

Table 17. Optoelectronic properties of devices obtained from ethanol containing precursor solution.

Annealing Temp [°C]	NaF [nm]	Jsc [mA/cm2]	Voc [mV]	FF [%]	Eta [%]	Rsh [Ohm·cm²]	Rs [Ohm·cm²]
500	10	8.24	73.42	26.39	0.2	9.02	31.12
550	10	6.11	152.80	30.52	0.3	21.94	28.69

The low efficiency values might be the result of a series of factors: the presence of oxides in the as sprayed films, the not totally planar surface of the sprayed absorber that difficult an optimum p-n junction formation and high recombination and/or low mobility of the few generated electron-hole charge carriers. The further efforts to improve the efficiency of the solar cells ought to be in the direction of change the solvent, improve the crystalline structure of the absorber and reduce the over selenization of the Mo back contact.

4.2 Methanol-based solutions

Other interesting solvent because of its properties, availability and simplified buying process is methanol. Methanol is the simplest alcohol, has a surface tension comparable to that of ethanol but has a lower boiling point and is of comparable density but much less viscous (Table 13). As an alcohol, methanol is a good solvent of metal chlorides.

It was found that the CZTS sprayed films using methanol-based solutions are also rough at the surface but much less than when using only water; it shows one more, that rough surfaces is an intrinsic characteristic of sprayed films.

Thus, a rough surface is one of the main challenges of the sprayed films if they are thought to be used as solar cells absorbers. Up to now in this thesis, different efforts have been done in the direction to reduce the surface roughness: changing the carrier gas pressure, substrate temperature, solvents and chemical etching. From them and standing on the gained experience, in this section the system and solution related parameters will be optimized for methanol + water (50%, v/v) solutions to obtain the appropriate Cu-poor Zn-rich composition of the device grade films; following a similar process as described earlier. The results of using $CuCl_2.2H_2O$, $Zn(CH_3CO_2)_2$, $SnCl_4.2H_2O$ and CH_4N_5S will be here presented. The use of $ZnCl_2$ and $SnCl_2$ was also tested but result in devices reporting no power conversion efficiency.

4.2.1 Characteristics of as-sprayed films

The XRD pattern of a typical as sprayed CZTS thin film from methanol-containing precursor solution (50%, v/v) on glass is shown in Figure 36. The insert shows the Raman spectra obtained when using a wavelength of 532nm.

From the XRD pattern of the as sprayed sample it is not possible to distinguish between ZnS (PDF: 00-005-0566), the ternary (PDF: 00-033-0501) or kesterite (PDF: 01-075-4122) due to the overlapping of the main diffraction peaks of all of them. The fingerprint of as-sprayed samples is to have low crystallinity kesterite; it is formed by the pyrolysis of the

precursors in solution thanks to the temperature of the substrate while spraying. However the Raman spectra reveal the presence of kesterite and possible Cu-S [80, 115, 126] compounds in the surface of the sample (~50nm).

The composition of our as-sprayed sample is 0.82, 1.24 and 1.48 for Cu/(Sn+Sn), Zn/Sn and Cu/Zn respectively; it well matches with the metallic ratios reported as the adequate for good efficiency kesterite devices [25, 48] as we reported it in previous works [57].
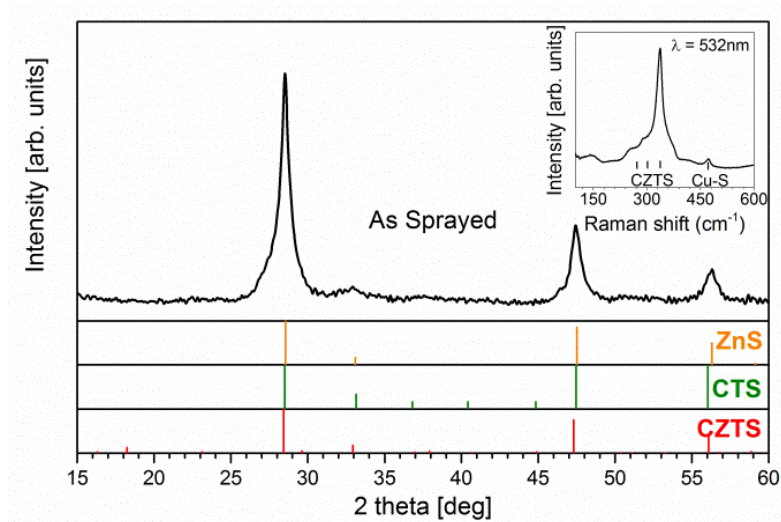
Figure 36. X-ray diffraction patterns of CZTS as sprayed sample. The insert shows the Raman spectra of the same sample using an excitation wavelength of 532 nm.

4.2.2 Surface roughness reduction: Br_2-MeOH etching

In this section, reduction of the surface roughness of the as-sprayed films is under investigation by means of a Br_2-based chemical etching. The process to etch the samples is the same as described for the ethanol-containing precursor solutions. But in this section an extended study is presented by using different etching times (from 30s to 240s) and Br_2 concentrations (0.010% and 0.025%).

Figure 37 shows the two different Br_2-MeOH solution concentrations during the etching time; where only a slight change in the etchant colour is appreciated.
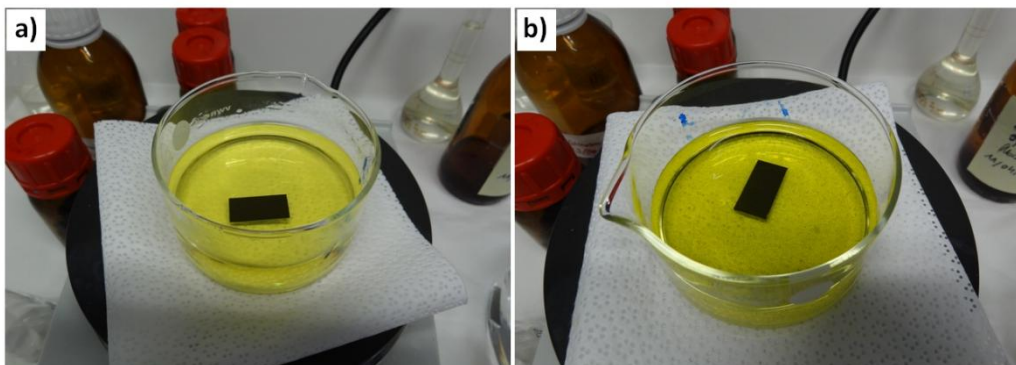
Figure 37. Br-MeOH solution during etching time. (a) 0.01%, (b) 0.025%

Figure 38 shows the mean roughness (or roughness average) Ra and the root mean square roughness RMS. The first is the arithmetic average of the absolute values of the roughness profile; the former is the root mean square average of the roughness. In other words, a single peak or flaw within the microscopic surface texture will affect (raise) the RMS value more than the Ra value. Both are a representation of the surface roughness but as mentioned, each is calculated differently from the same measured microscopic peaks and valleys.
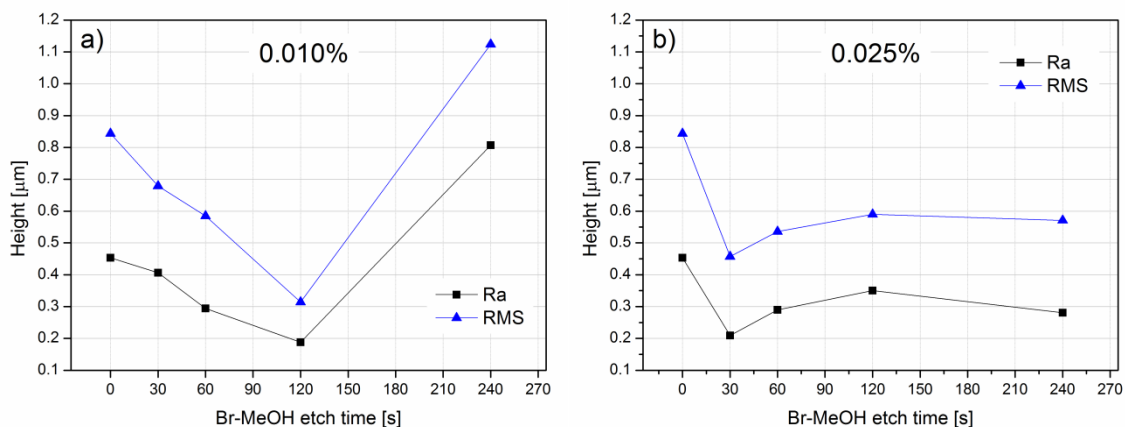
Figure 38. Roughness evolution of as sprayed films using different etching times for two concentrations of Br$_2$-MeOH: (a) 0.010% and (b) 0.025%.

Figure 38 compares different concentrations of Br$_2$-MeOH as etchant of as sprayed CZTS samples for different etching times. The lowest Br$_2$-MeOH concentration (0.010%, Figure 38a) shows a gradually reduction of the peak to valley difference by increasing the etching time up to 120 seconds. After that time both roughness values (Ra and RMS) abruptly increase (more than in the as sprayed sample); the etchant has created deep bypaths on the more vulnerable parts of the film.

Using a strongest Br$_2$-MeOH etching solution of 0.025% (Figure 38b) the roughness of the as sprayed films is rapidly reduced in the first 30 seconds. The 30s (0.025%) sample has a similar Ra value to the 120s (0.01%) sample however in the latter sample; the RMS value is higher than that in the former sample. It means that the 0.025% etching is so strong that rapidly creates marked peaks and valleys; it is contrary to what we are looking to obtain by this etching.
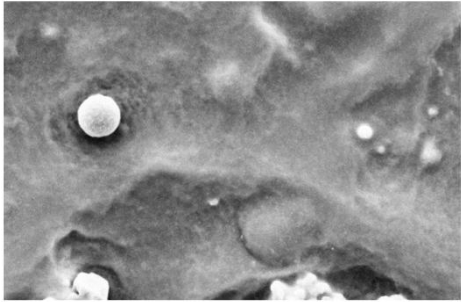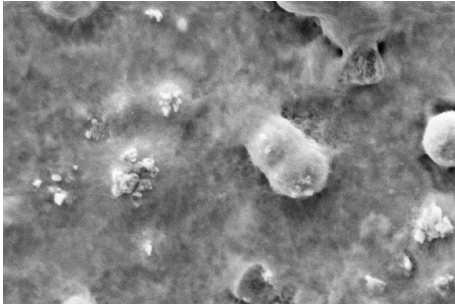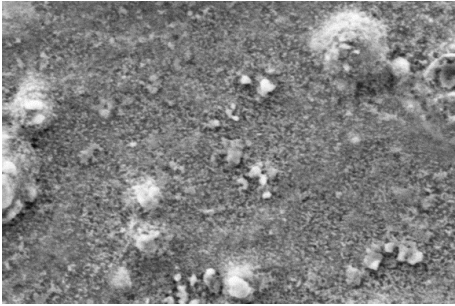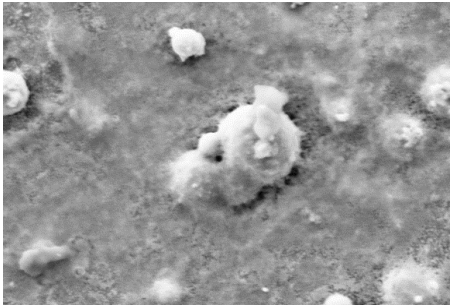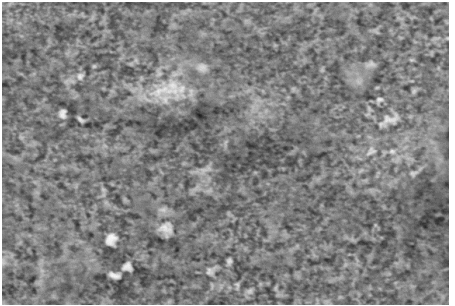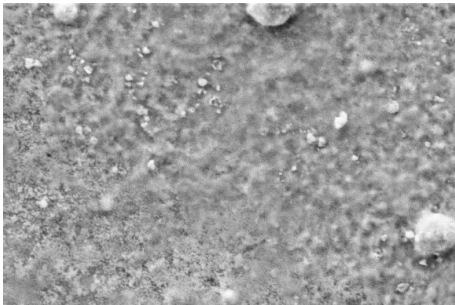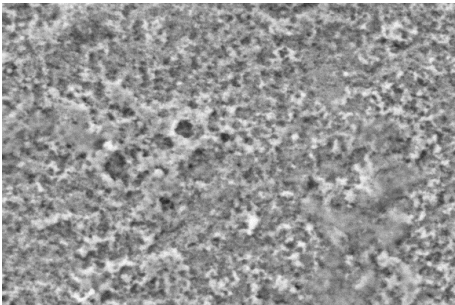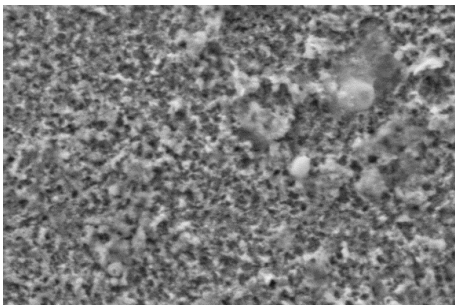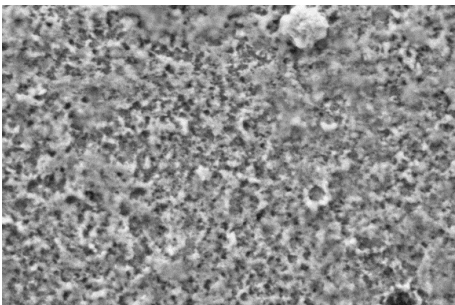
The SEM top views of the etched samples are shown in Table 18 for the different etching times. They confirm what is shown in Figure 38; long etching times and/or concentrated etchant increases the roughness of the films. From that, it is better to use low bromine concentrations and longer times; from the experimental point of view, longer times are also preferred in order to control better the time.

After 210 seconds (0.01%) the samples were partially dissolved, making visible the substrate. Higher concentration of Br were also tested, with 0.05, after 1 minute etching the films started aggressively being dissolved from the borders, 0.1% dissolved immediately the samples leaving just the substrate. As seen in Table 18, the segregates in the surface start to disappear after 1 minute of Br-MeOH etching; after 2 minutes the surface is totally free of them. Longer etching times after removing the precipitates, start affecting the film.

As shown in Figure 38, the average roughness of the films was reduced after etching but the peak to valley difference is still in the order of hundreds of nanometers (~200nm). The reason of that is the intrinsic roughness of the as-sprayed films; the next section investigates the possibility of reducing this roughness by using a dispersant agent in the precursor solution to obtain smoother as-sprayed films.

Table 18. SEM images (5kV) of Br-MeOH etched samples of as sprayed samples for different time and concentrations

5kV	Concentration [v/v]	
Time [s]	0.010%	0.025%
0		
30		
60		
120		
180		

4.2.3 Dispersing agent

Going in the direction to obtain as-sprayed films with a lower roughness, the use of a dispersing agent or a *dispersant* was also tried. A dispersant is a surface-active-substance added to a suspension or colloid to improve the separation of particles to prevent settling or clumping. Although when the precursor spray solution is stable (Figure 39), it is neither a suspension nor a colloid, the use of a dispersant was proposed to help in spreading the precursors in the substrate to prevent the formation of agglomerates.

The chosen dispersant was Triton X-100 as it is stable in acid media and soluble in water. Methanol + water (50%, v/v) precursor spray solutions containing 0.02% and 0.04% (v/v) of the dispersant were prepared. One of the possible mayor drawbacks of using this dispersant is its carbon content.
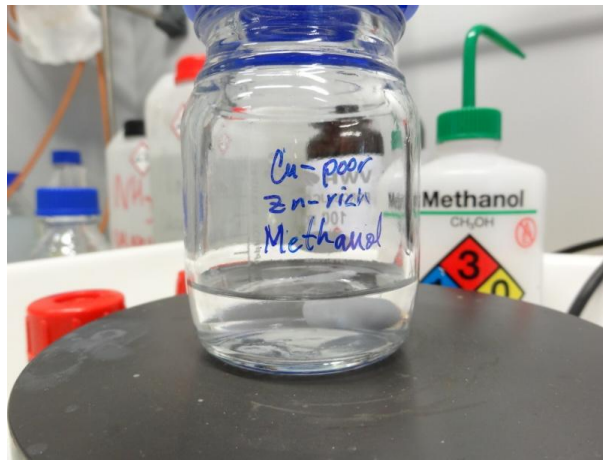
Figure 39. Stable spray precursor solution after 24 hours.

Figure 40 show a typical top view of as sprayed sample from a methanol-based precursor spray solution containing dispersant. For both of the dispersant concentration used, the as sprayed films showed long and apparently deep cracks. The cracks reveal a change in the plasticity of the films probably during cooling.
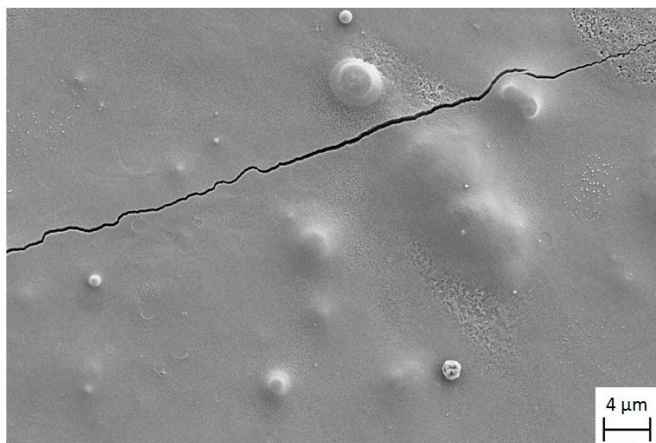
Figure 40. Top view of as sprayed sample with dispersant in the precursor solution.

In order to eliminate the possible carbon on the films coming from the precursors and mostly from the dispersant, half of the films were soft annealed 20 minutes in a hot plate in air conditions at 200°C and the other half was long annealed at the same temperature in Ar-H$_2$ at 1mbar. After soft annealing 10nm of NaF was evaporated to the samples previous a one-step annealing at 550°C (15 minutes, Se: 20mg), the results are shown in Figure 41.
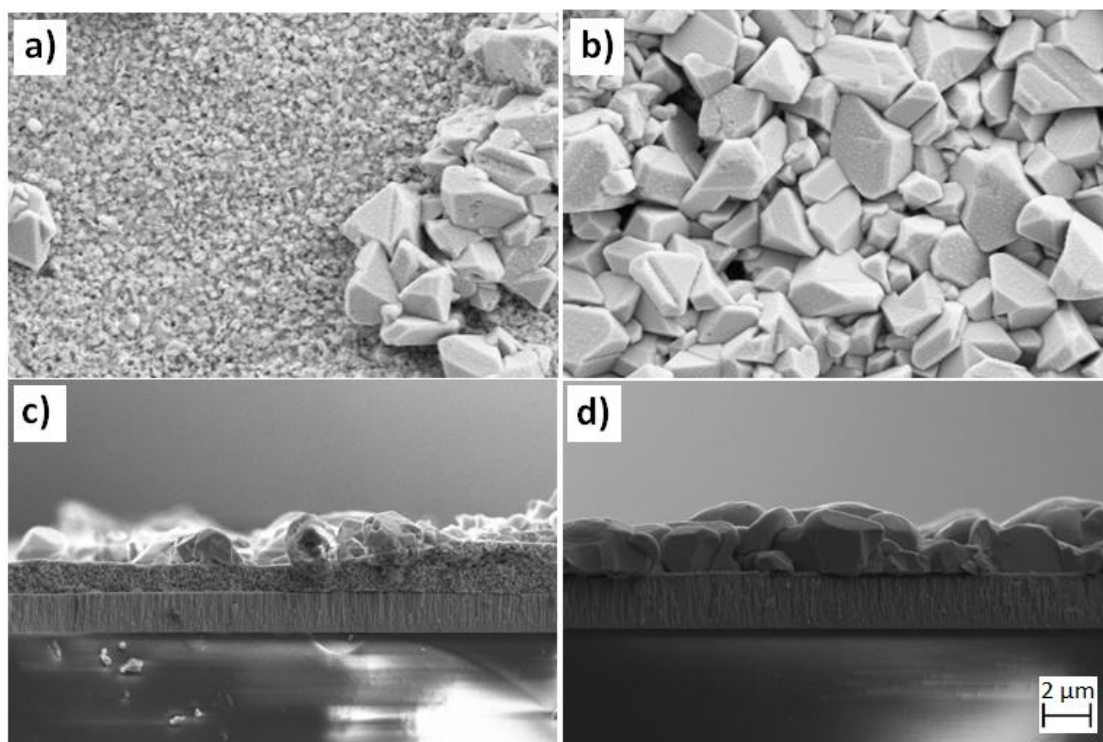
Figure 41. SEM images of samples annealed at 550°C after soft annealing in hot plate (a,c) and in Ar-H$_2$ (c,d).

The use of the selected temperatures, times and atmospheres for the soft annealing comes from the experience of IREC's solar group in the preparation of CZTSSe absorbers. Burning the samples in a hot plate result in a compact layer covered with randomly distributed big

grains. Soft anneal the samples in Ar-H$_2$ atmosphere produces equally big grains without the compact bottom layer nonetheless the film is not compact (Figure 41b). The observed big grains can indubitably be attributed to the use of NaF as dopant but no working devices were expected from any of the films.

No advantages were found with the use of a dispersing agent; on the contrary, the as sprayed films presented cracks; annealed films were not compact coupled with the over selenization of the Mo back contact. In the next no dispersant was used.

4.2.4 Carbon content

In the solution-based deposition techniques *the* ever rising question is about the quantity of carbon content on the films. The low weight of this element (atomic number 6), and its abundancee in normal room conditions, make it complicated, to be free of it and quantify it.

With the intention to estimate the carbon content on freshly sprayed films, elemental EDX quantification was used. Figure 42 shows the EDX area scan and SEM top view of the sprayed CZTS as sprayed sample in a typical area with a segregate on the top.

Table 19. EDX composition of as sprayed film from methanol-based solution.

EDX atm%						Metallic Ratios		
Cl	Cu	Zn	Sn	S	C	$\dfrac{Cu}{Zn+Sn}$	$\dfrac{Zn}{Sn}$	$\dfrac{Cu}{Sn}$
3.78	23.65	14.85	11.68	34.82	11.21	0.89	1.27	2.02
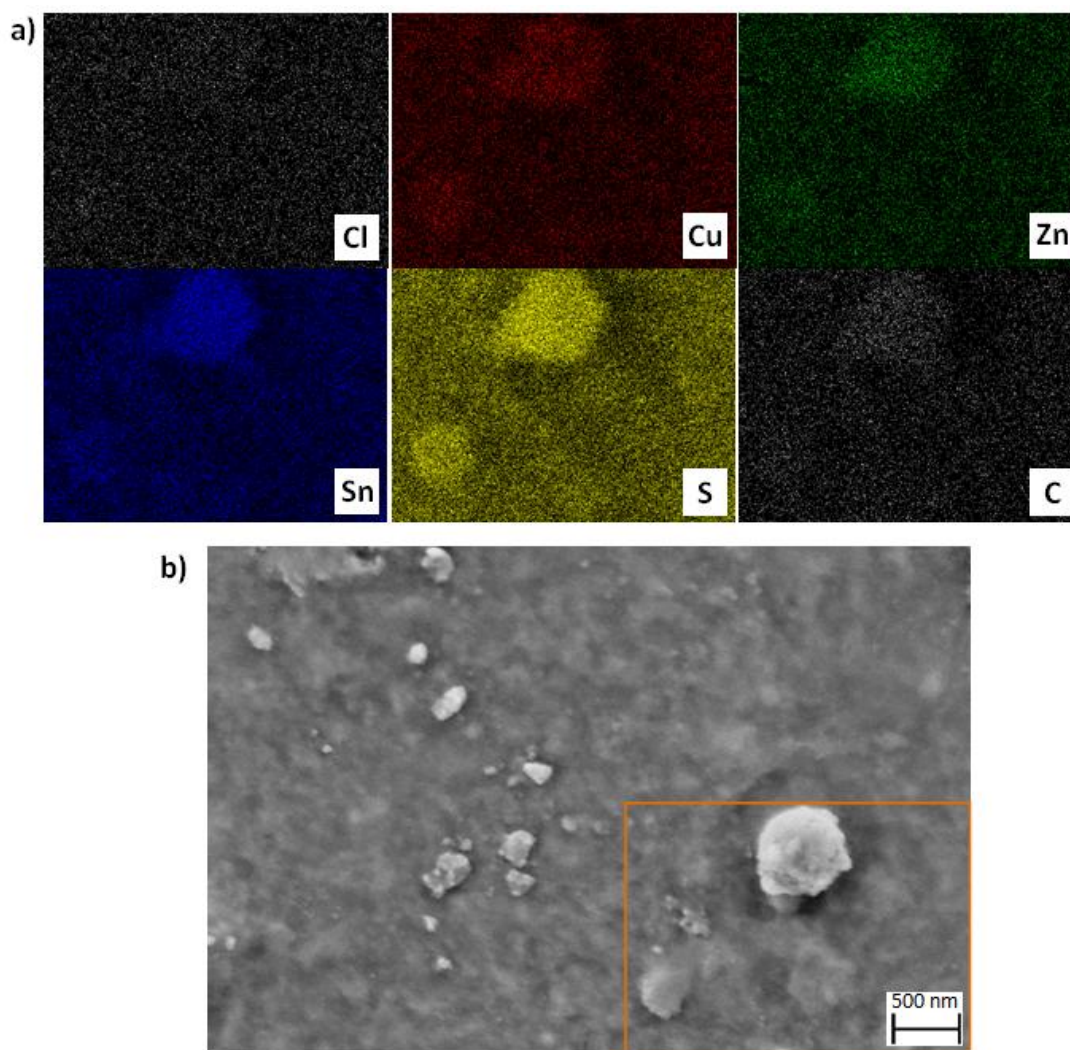
Figure 42. (a) EDX area scan of as sprayed film.
(b) shows the SEM top view area of scan

In figure Figure 42a the EDX area mapping integration of the different possible elements in a freshly sprayed CZTS film are shown. The possibility of finding Cl in the as sprayed samples comes from the use of metal chlorides as metal precursors. Figure 42a reveals no evidence at all of Cl on the as sprayed film neither in the segregate. As seen earlier in this chapter, the segregate is formed by the same elements of kesterite; possibly its carbon content is slightly higher but it could be also because they are more compact than the rest of the film. The quantitative analysis in atm% is shown in Table 19; relatively low carbon was found in the film.

4.2.5 One step selenization: CZTSSe-based solar cells

This section deals with the *selenization* of sprayed CZTS thin films. A selenization process should be understood as the process thought which a sprayed CZTS thin film gains structural crystallinity and is enriched in selenium to produce CZTSSe thin film absorbers for photovoltaic applications.

In a selenization process, the heating rate, the gas atmosphere and pressure, the selenium source and amount, the temperature and duration, are the general annealing parameters to control. Those variables can be said to describe an *annealing profile*; it can be as complex or as simple as the researcher wants, depending on the pursued goals.

In this thesis two fundamental annealing profiles for sprayed CZTS films were studied: one step and two step selenization. The name refers to the number of times in the same selenization run the sample is maintained at a certain temperature for a pre specified time and Ar pressure. It means that only temperature, duration, selenium amount and Ar pressure were the parameters under study rather in one step or two step selenization profiles.

In this section, CZTS thin films have been deposited by SP under Argon atmosphere followed by a one-step selenisation. This section focus in the study of two different annealing parameters: the variation of annealing temperature in the rage of 450 °C to 580 °C and the variation of Se partial vapor pressure aiming to obtain different Se contents. The result was films with systematic variation of the optical band gap energy and a corresponding shift in the Raman scattering and XRD peak positions. In depth GD-OES analysis was used to disclose the compositional profiles of our as sprayed and selenised films; finding that the films results to be Se-rich but not S-free. By employing our most promising experimental conditions, working devices were processed with efficiencies up to 1.9%.

The metallic ratios of the annealed samples when 150mg of elemental Se were placed in the graphite box are shown in Table 20. Only slight changes from the as sprayed to the annealed samples, are appreciated.

Table 20 XRF metallic ratios of the as sprayed and annealed samples. For the annealed samples, 150 mg of powder elemental Se was used.

Annealing themperature [°C]	Se: 100mg			Se: 150mg			Se: 200mg		
	$\frac{Cu}{Zn+Sn}$	$\frac{Zn}{Sn}$	$\frac{Cu}{Zn}$	$\frac{Cu}{Zn+Sn}$	$\frac{Zn}{Sn}$	$\frac{Cu}{Zn}$	$\frac{Cu}{Zn+Sn}$	$\frac{Zn}{Sn}$	$\frac{Cu}{Zn}$
As sprayed	0.82	1.25	1.51	0.82	1.24	1.48	0.84	1.28	1.52
450	0.82	1.18	1.51	0.86	1.18	1.59	0.86	1.29	1.53
500	0.82	1.21	1.50	0.82	1.24	1.47	0.86	1.27	1.53
550	0.81	1.21	1.49	0.83	1.26	1.49	0.84	1.24	1.52
580	0.81	1.20	1.49	0.80	1.19	1.48	0.84	1.21	1.54

Table 21 shows the [S]/([S]+[Se]) ratio measured by XRF of the different samples on this study. The ratio gets smaller with higher temperatures and bigger Se mass therefore; a better Se incorporation is achieved within those conditions.

Table 21. XRF [S]/([S]+[Se]) ratio of annealed films

Se mass [mg]	Annealing Temperature [°C]			
	450	500	550	580
100	0.35	0.30	0.29	0.32
150	0.38	0.30	0.30	0.28
200	0.29	0.28	0.22	0.24

In all samples, the ratio shown in Table 21 is between 0.2 and 0.4, it evidences that the replacement of S atoms by Se atoms at conditions is thermodynamically favourable. It is possible even with low annealing temperatures like 450°C. However as we will show later, this replacement is not enough for obtaining films with good crystallinity that results in not working devices. After selenization and linked with the S to Se content, the band gap of the films is modified towards the typical of Se-rich films [48, 97] as Figure 43a shows.

The optical energy band gaps was obtained by taking the spectral transmittance and reflectance of the samples and from them the absorption coefficient (α) as function of the photon energy $h\nu$ [97]. The optical band gap energy was estimated from the linear extrapolation of the plot $(\alpha h\nu)^2$ versus $h\nu$ with the $h\nu$-axis. This calculation is shown in the insert of Figure 43a for the sample annealed at 580°C with 200 mg of Se whose optical band gap energy results to be 1.13±0.02 eV. The same procedure were done for the other samples; the so obtained optical energy gaps *vs.* annealing temperature are plotted in Figure 43a.

Figure 43b shows the linear relation that exists at constant temperature between the band gap energy and the concentration of S and Se, as Vegard's law states [127]. In terms of the solid solution $Cu_2ZnSn(S_xSe_{1-x})_4$ this law can be written as follows.

$$Eg_{SSe} = xEg_S + (1-x)Eg_{Se} \qquad (1)$$

Where, Eg_S and Eg_{Se} are the band gap energy when x=1 (1.5eV) and x=0 (1eV) respectively. Taking room temperature as constant by the time of the experiments, the S content of the films respect to the Se content is shown in Figure 43b, it well matches the ratios obtained by XRF in Table 21.
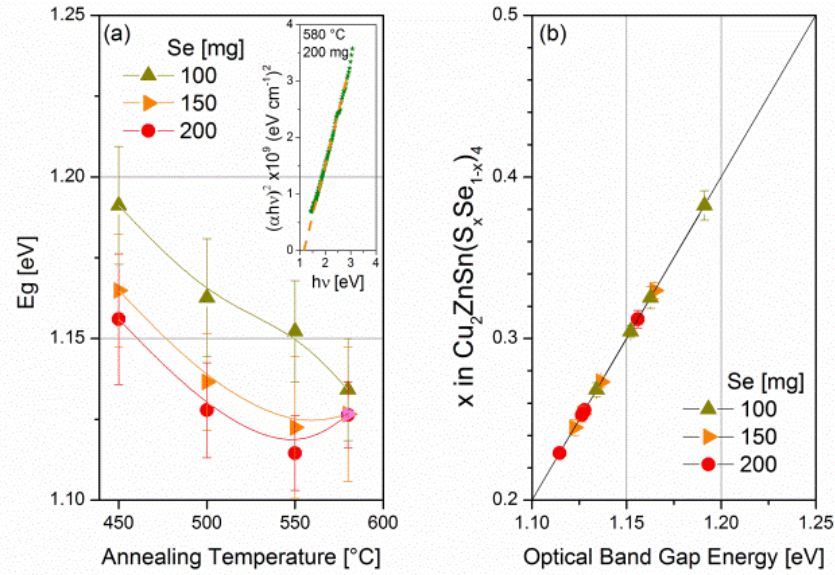
Figure 43. (a) Optical band gap energy of samples annealed under different conditions. The insert shows the linear extrapolation of the $(\alpha h\nu)^2$ curve vs. photon. (b) Chalcogen content of the samples calculated from its optical band gap energy by using Vegar's Law.

Concerning with the composition of the films, non equilibrium plasmas such as glow discharges are becoming a commonly used tool in direct surface analysis of solid materials, for analytical applications [128]. Here we have used a Glow discharge Optical Emission Spectrometer (GD-OES) HORIBA GD Profiler 2 powered with a radio frequency source (RF GD-OES) to fast track the surface and in-depth chemical composition profile of a set of samples. Figure 44 shows the in-depth profiles of the as sprayed and two annealed samples (at 450°C and 580°C both with 150mg of Se).
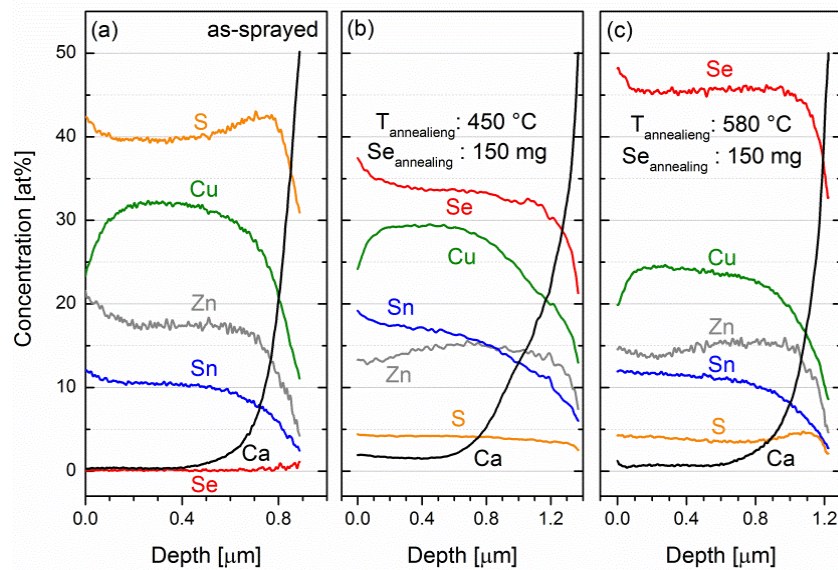
Figure 44. GD-OES analysis of as sprayed (a), annealed at 450 °C (b) and annealed at 580 °C (c) samples, both annealed with 150mg of Se.

In all the cases the Cu-poor and Zn-rich nature of the samples can be seen. For the sample annealed at higher temperature (Figure 44c), the Se profile is constant in-depth and also is globally higher than in the sample annealed at 450°C (Figure 44b). The in-depth concentration profiles of samples annealed at 500°C by using different amounts of elemental Se can be found in Figure 45
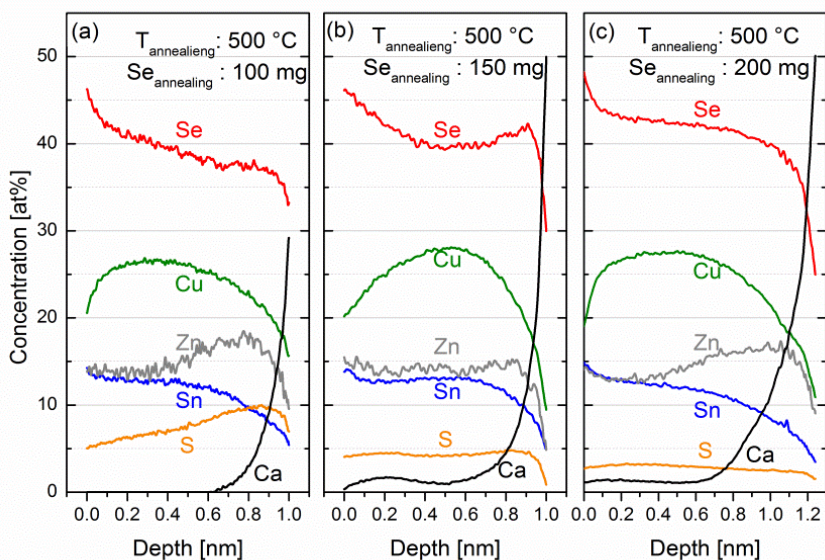
Figure 45. GD-OES analysis of samples annealed at 500°C by using different amounts of elemental Se; 10mg (a), 150mg (b) and 200mg (c).

Figure 46 shows the in depth Se concentration profiles of different samples annealed at different temperatures using 150mg of Se. In any case Se is able to completely replace the S atoms (Figure 44) but the concentration of Se increases with the annealing temperature (Figure 46). It is in well agreement with the optical measurements, the XRD and Raman spectroscopy results.
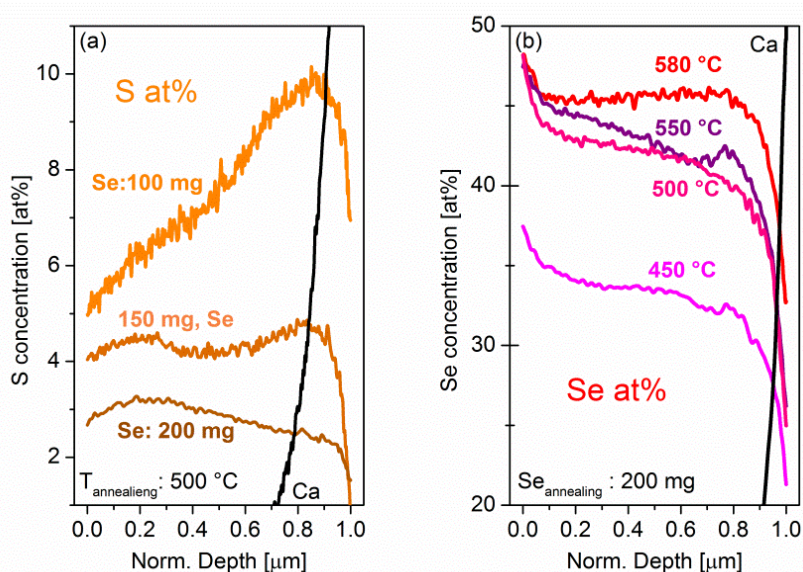
Figure 46. Detail of in-depth composition profiles of S (a) and Se (b) for different selenization conditions.

The size of the grains in a polycrystalline thin film has pronounced effects on many of its properties. Bigger grains in thin films for solar cells absorber are usually desired, as they represent a continuous media for the charge carriers. Is in the grain boundaries where high recombination probability exists due to the high trap density, result of structure defects and lattice discontinuities. However for kesterite as has been shown, bigger grains are not always the best choice in terms of device efficiencies[54].

The SEM cross section image of the as sprayed sample (Figure 47a) shows its amorphous-like structure, typical of the solution-based deposition techniques prior annealing. It can be also appreciated the high surface roughness of the films, characteristic of the thin films obtained by spray pyrolysis [61, 97] after Br_2-MeOH etching. After annealing at 450°C (Figure 47b), small kesterite grains (~200nm) are formed; when annealing at the higher temperature of 580°C (Figure 47c) thicker layers and bigger grains are obtained in agreement with the crystallite size in Table 22.
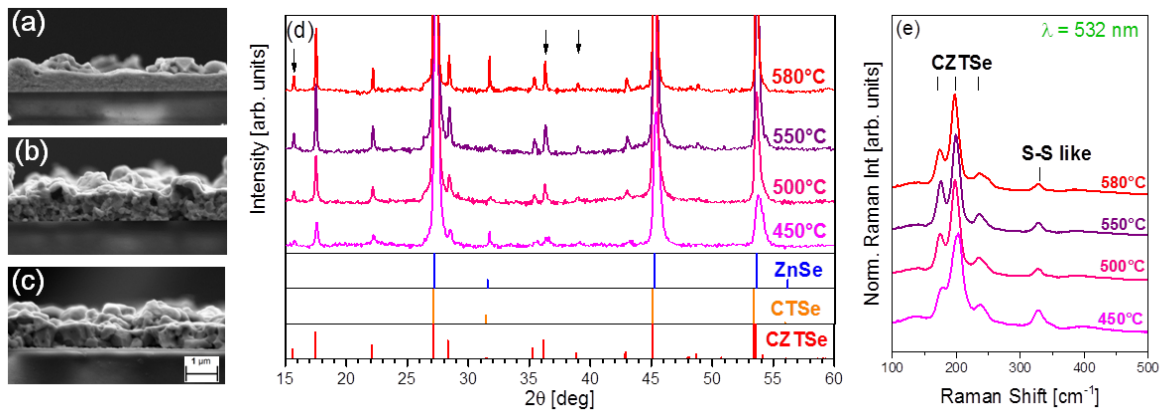
Figure 47. SEM images of as sprayed sample (a), 450°C annealed sample (b), 580°C annealed sample (c); X-ray diffractogram of annealed samples (d) and top Raman spectra (λ = 532nm) of annealed samples (e). All samples were annealed using 150mg of Se.

The X-ray diffractogram of sprayed kesterite samples selenized at different temperatures are shown in Figure 47d. As shown in the reference patterns, if we look only at the main lines of ZnSe (PDF: 00-037-1463), the ternary (PDF: 01-078-0600) or kesterite (PDF: 01-070-8930) it is not possible to distinguish one from other as was mentioned before. However, the minor reflections (002), (211) and (114) (at $2\theta \approx 15.6°$, $36.2°$ and $38.9°$ respectively) proof the presence of CZTSe given that those reflections are absent from the binary ZnSe and the CTSe ternary[129]. They appear in all the annealing temperatures under study and are denoted with an arrow in Figure 47d.

Figure 48 shows the $2\theta_{exp}$ -$2\theta_{teo}$ shift for (002) and (211) reflections; $2\theta_{exp}$ is the experimental position of the respective reflection and $2\theta_{teo}$ is the position of the reflection from the PDF files. In Figure 48 the position of both reflections are shifted to lower angles as the temperature increases, getting closer to the reference position as more Se is been incorporated on the structure as Figure 46 shows; this shift means that the films are been converted to rich selenium kesterite. It is the same trend seen in the optical measurements (Figure 43a).

Figure 48 also plots the intensity of each XRD peak; the intensity of the peaks increases constantly with the temperature from 450°C to 550°C. However with the highest temperature of 580°C the intensity of the peak decreases. It could be due to possible decomposition of the kesterite because of the high temperature and low pressure of chalcogen however, the remaining Kesterite in the respective crystallographic domains gains crystallinity as the FWHM is been reduced with temperature (Table 22).
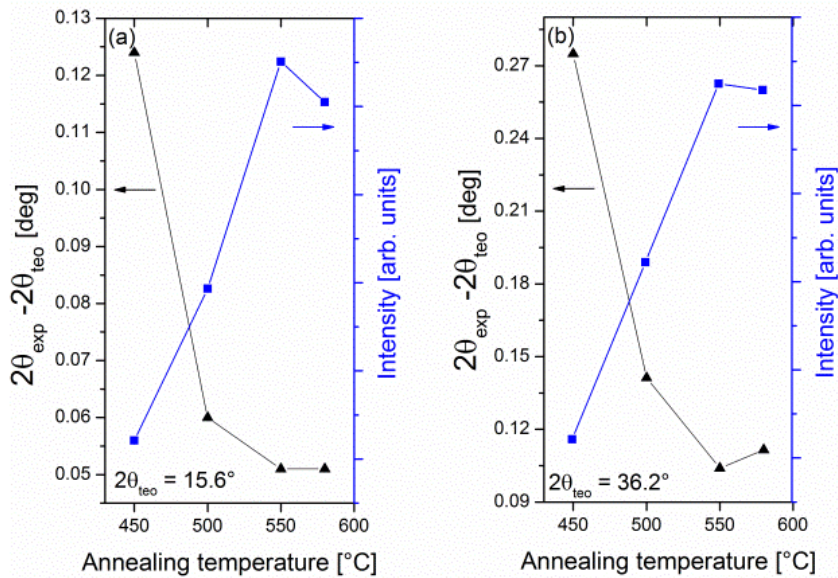
Figure 48. Temperature evolution of reflections (002) and (211) (at 2θ ≈ 15.6° and 36.2°).

The crystallographic orientation of each grain in a polycrystalline aggregate normally is different or each grain. If the orientation of all grains usually tends to cluster, to a greater or lesser degree about some particular orientation, in relation to some selected frame of reference, the films are said to have a preferred orientation to the [*uvw*] crystallographic direction. In the sprayed kesterite films is not possible to speak straight forward of a certain crystallographic orientation as many phases are present.

When metals or alloys are recrystallized by annealing, the new grain structure usually has a preferred orientation; this is called *annealing texture* or *recrystallization texture*. Preferred orientation exists in natural and artificially produced materials; is generally the rule not the exception. In the case of artificially produced materials may depend on the preparation technique. On the contrary, the preparation of an aggregate with a completely random crystal orientation is a difficult matter. Preferred orientation is only a crystallographic status of the films, and has nothing to do with grain shape. Therefore the presence or absence of preferred orientation cannot be disclosed by microscopic examination of the shape of a crystal depends of the interior arrangement of the atoms.

The crystallite size is determined using Scherer's formula:

$$t = \frac{0.9\lambda}{B\cos\theta}$$

Where λ is the wavelength of the x-ray, θ is the Bragg angle and B is the FWHM of the characteristic peak. Table 22 shows the FWHM of two minor reflections of samples annealed at different temperatures using 150mg of Se. The selected minor reflections reveal the improved kesterite crystallinity with the annealing temperature.

Table 22. Crystallite size for different annealing temperatures and Bragg angles.

Annealing temp. [°C]	15.6°		36.2°	
	FWHM [deg]	Crystallite size [nm]	FWHM [deg]	Crystallite size [nm]
450	0.27	29.28	0.57	14.62
500	0.22	36.40	0.25	33.79
550	0.15	52.81	0.24	35.00
580	0.14	55.79	0.14	59.94

Figure 47e shows the top Raman spectra using a wavelength of 523nm (green excitation) for the set of samples annealed with 150mg of Se. The main characteristic Raman modes of Se-rich kesterite are observed for all the annealing temperatures along with a S-S-like mode in all samples; including the ones annealed using 100mg and 200mg (Figure 49) of Se confirming a remain of S after selenization. The intensity of this mode decreases with temperature in agreement with the previous results.
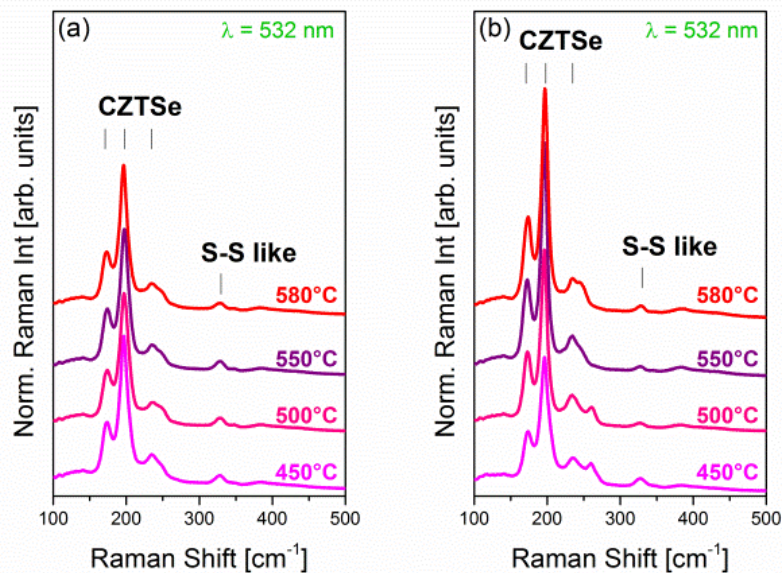
Figure 49. Top Raman spectra using green excitation wavelength of annealed samples using 100mg (a) and 200mg (b) of Se.

The intensity of the main A^1 mode increases with the temperature from 450°C to 550°C but decreases for 580°C; it is the same trend observed by XRD. Figure 50 shows the evolution detail of A^1 mode in position and intensity for different annealing runs using 150mg (Figure 50a) and 200mg (Figure 50b) of elemental Se.
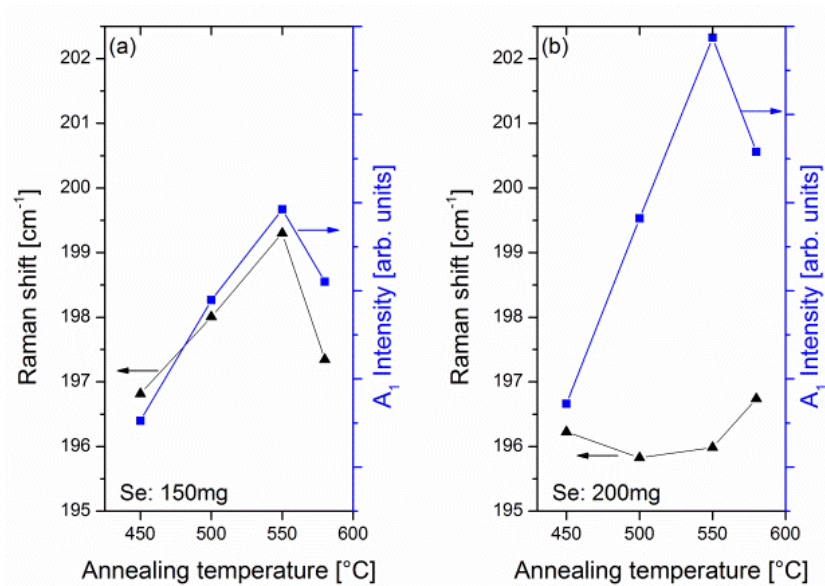
Figure 50. Temperature evolution of Raman shift and intensity of the main A^1 mode for two different set of samples one using 150mg of Se (a) and 200mg of Se (b).

The illuminated and dark J-V curves of the solar cells prepared with selenised absorbers using 150mg of Se are shown in Figure 51. The absorber annealed at 450°C resulted in a non working device; the one annealed at 580°C has a highly selenised molybdenum. Reduce the strong cross over and the high series resistance of the devices (Table 23) are one of the challenges of the solar cells processed by pneumatic spray pyrolysis from salt precursors[57, 73].
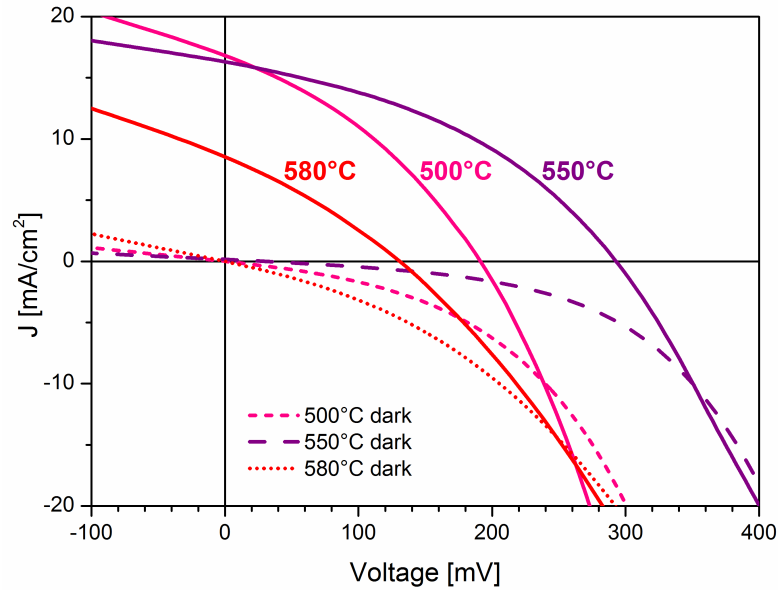
Figure 51. J-V characteristic of the selenised absorber at 500°C and 550°C using 150 mg of Se. Continuous lines are illuminated curves, dotted lines are dark curves.

Table 23 presents the short-circuit current (J_{sc}), open-circuit voltage (V_{oc}), fill factor (FF), power conversion efficiency, the shunt and series resistance (R_{sh}, R_s), ideality factor (A), and reverse saturation current (J_0).

Additionally, what pulls the efficiency down is the roughness of the sprayed films producing defects; this roughness is characteristic of the deposition technique and is affecting the junction formation allowing the transit of charge carriers in inverse voltage. Those results show the potential of our material to obtain higher efficiencies after ongoing improvements.

Table 23. Electrical characteristics of different devices. Each absorber was annealed using 150mg of Se.

Annealing Temp. [°C]	Jsc [mA/cm²]	Voc [mV]	FF [%]	Efficiency [%]	R_{sh} [Ωcm²]	R_s [Ωcm²]	A	J_0 [mA/cm²]
500	16.8	191.1	34.7	1.1	41.4	5.9	3.1	1.5
550	16.3	292.9	39.1	1.9	49.5	7.2	2.6	0.2
580	8.5	130.9	29.4	0.3	37.4	11.2	2.6	1.4

4.2.6 Two steps selenization: CZTSSe-based solar cells

This section is about the selenization process when it consists of two different steps at different temperature, each for certain duration. The idea behind a two step selenization

process is to follow a typical chemical reaction during annealing[26, 130]; starting from the chalcogenide binaries and ternaries to end up with high crystallinity kesterite. In all the cases, the annealing were preformed in a semi-closed graphite boxes where elemental Se and Sn where placed inside the box after been weight. The films presented in this section where made using $CuCl_2.2H_2O$, $Zn(CH_3CO_2)_2$, $SnCl_4.2H_2O$ and CH_4N_5S in a concentration of 7.2mM, 5.4mM, 4.95mM and 50mM respectively in a 50% H_2O+CH_3OH (v/v) solution to obtain the appropriate Cu-poor Zn-rich composition of as sprayed CZTS films.

In order to promote the formation of the binaries and ternaries, the first step is performed at relatively low temperature and low pressure, at this conditions the material is provided of enough energy to react in the presence of $Se_{(g)}$. During the second step at high temperature, the formation of highly crystalline kesterite is achieved, avoiding decomposition due to the high $Se_{(g)}$ overpressure. From the annealing parameters standpoint each step can be considered as nearly independent from the other. In this section, the main annealing parameters that were modified on each step are: duration, temperature and gas pressure. The partial pressure of chalcogen can also be modified but in separate annealing run at a time.

Different two step annealing was performed in order to:

    i.   Obtain CZTSSe absorbers,

    ii.   Explore the possibility of tune the S/(S+Se) ratio by means of the annealing parameters and

    iii.   Produce working solar cells from sprayed thin films with the better possible efficiency.

However in the middle way some difficulties were found such as the high ratio of sulfur left on the films and the over selenization of the molybdenum back contact. To overcome those issues different routes were followed as will be described.

In the first attempt of two step annealing, one of the most important parameters was studied; it is *the time of annealing*. As is shown in Figure 52, during the first step, the pressure and the temperature was kept constant in all the experiments to 1mbar and 400°C, respectively; the duration of this first step was chosen to be 5 or 15 minutes. For the second step, the pressure is increased to 1bar; before the temperature reaches the desired set value (550°C), the duration of this step was 15 or 30 min. The different annealing parameters (duration, pressure and temperature) are alike the ones have been reported in our group resulting in high efficiency devices from sputtered metallic stacks[24].
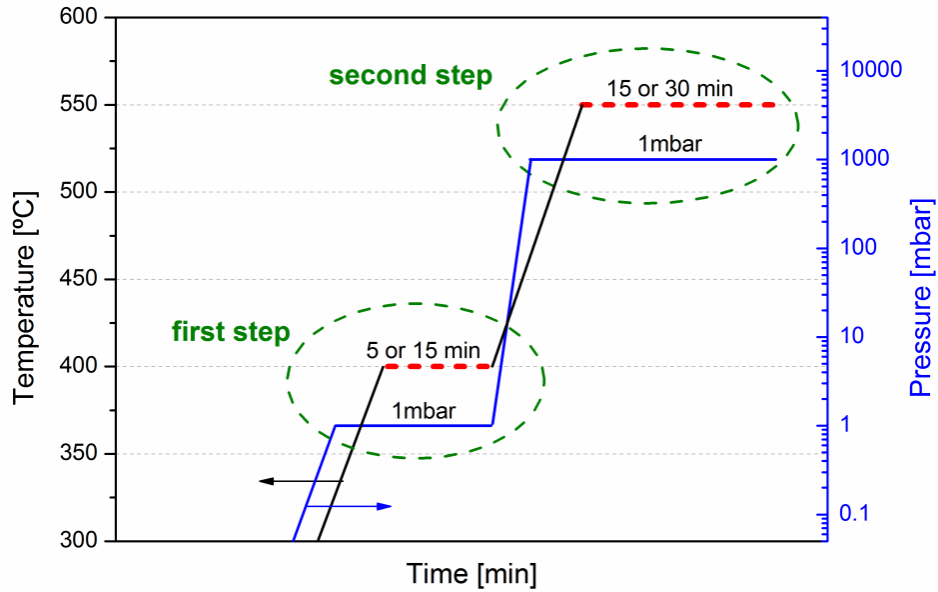
Figure 52. Two step annealing sketch of temperature (and pressure) vs. time. Only the duration of the steps is been changed.

The duration of each step, for each annealing run is shown in Figure 53. The green star shows the optimum S and Se content of the world record CZTSSe-based solar cell[9]. The dotted line represents the possible values for which S[atm%] + Se[atm%] = 50%.
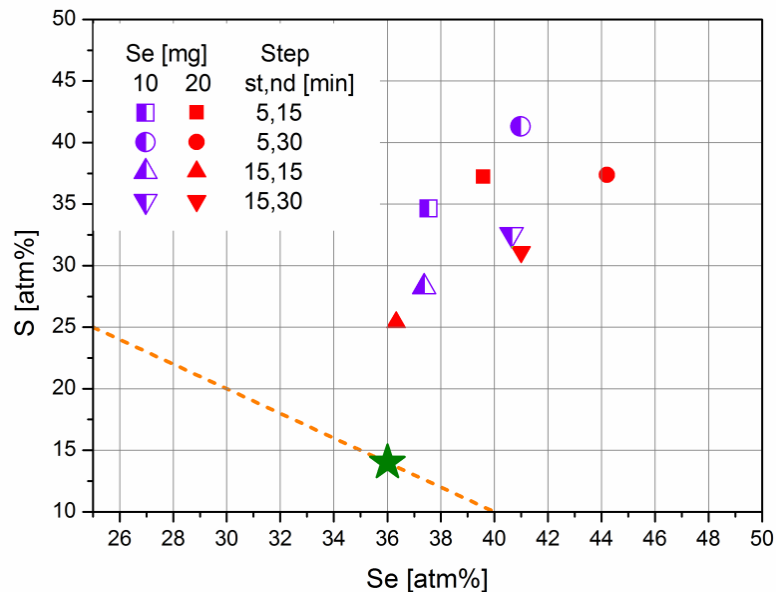
Figure 53. S and Se content on the films with different selenization times. The duration in minutes of the first (st) and the second (nd) step is shown.

In the first approach 10mg of Se were used, the results are showed in Figure 53 under half left figures. The duration of the first step is related with the decrease of S on the films. See for example 10mg of step (st,nd) = (5,15) and (15,15) where the Se content is more or less the same but the S content decreased after a long first step. Using the mentioned experimental conditions, the selenized films where still far from the S+Se content of the device record due to excess of S. However the best result (in terms of S+Se content) was obtained by a long first step and short second one, it is: (st,nd) = (15,15).

4. From Alcohol-Based Solution to Sprayed CZTSSe Solar Cells

In order to try to obtain films with lower S content our next strategy was to increase the Se amount used in the selenization. On this second part of the two step selenization experiments, we doubled the Se used. The results are shown in Figure 53 under solid figures. A general increase in Se content was observed and one more time the best result, with the lowest S content is for long first steps and short second steps. However, it seems that a content limit for both S and Se has been reached; it must be related with the sprayed solution history of the films.

At this point due to the high reactivity of Se at high temperature is not possible to use bigger amounts of Se to prevent the complete selenization of the Mo back contact which has been already strongly selenized by long duration annealing runs. Aside effect of the over selenization of the back contact is to have S[atm%] + Se[atm%] >50%, those are the S and Se values that lay in the upper part of the dotted line; it can also reflect the existence of multiple undesired phases.

To draw closer to the reduce the S atm% content and standing on the experience gained so far, long fist steps and short second steps was the strategy for the selenization of the next set of samples.

Figure 54 shows the experimental plan; this time first steps with fixed time to 30 min and second steps of 15 min were under study. The annealing temperature was varied around the values of the previous experiments as shown in Figure 54.
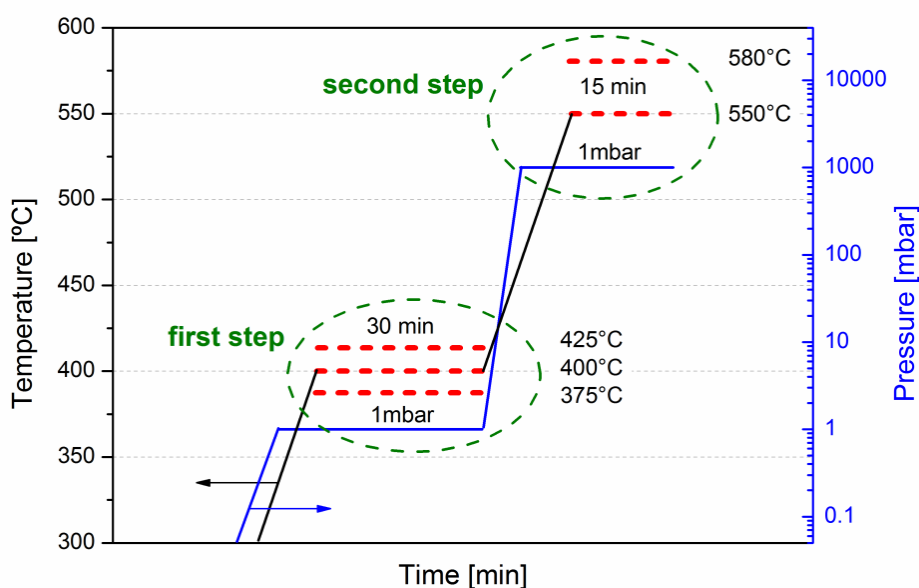
Figure 54. Two step annealing sketch of temperature (and pressure) vs. time. The temperature of the steps is under study, the time is fixed as shown.

The results of this new strategy are shown in Figure 55. The S and Se content of the world record device[9] is shown as green star; the upper red triangle is the same as in Figure 53. The direct effect of increasing the time of the first step and reducing it in the second one is the purple down triangle; the only change is in the slightly Se reduction.

Whit the temperature of the second step fixed to 550°C, and the temperature of the first step following the experimental plan, it was found that a higher temperature in the first

step modifies for better the S and Se content on the films as shows the left gray triangle in Figure 55.

It is the film that once finished the device, reported the best efficiency of the two step selenization samples with η=0.72% as Table 24 shows. Second step temperatures higher than 550°C are totally discarded due to total molybdenum selenization.
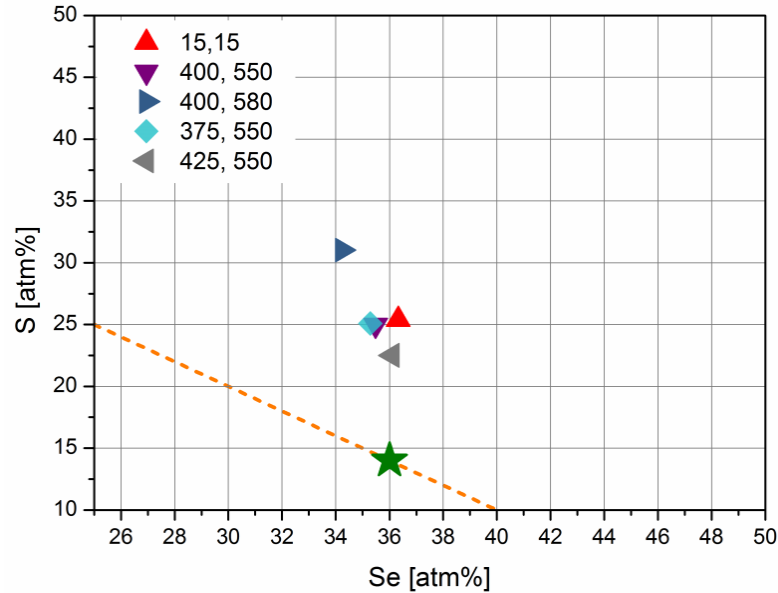
Figure 55. S and Se content on the films with different selenization temperatures.

Table 24 shows the short-circuit current (J_{sc}), open-circuit voltage (V_{oc}), fill factor (FF), power conversion efficiency, the shunt and series resistance (R_{sh}, R_s), ideality factor (A), and reverse saturation current (J_0) of the devices obtained by selenization of CZTS sprayed thin films in a two step selenization process. In order to complete the solar cells, the surface roughness of the samples was reduced by 2 minutes etching in 0.010% Br_2-MeOH solution at room temperature prior selenization. After annealing and just after the CdS buffer layer deposition, the films were 2 minutes etched in 10% HCl at 75°C. In Table 24, the first column shows the annealing parameters under study. Devices with short duration first step annealing and long second steps have smaller V_{oc} than those with long first step. The devices not shown in the table were piled off after the HCl etching previous the CdS deposition.

Table 24. Optoelectronic parameters of the two step selenization solar cells

Param.	J_{sc} [mA/cm²]	V_{oc} [mV]	FF [%]	Efficiency [%]	R_{sh} [Ωcm²]	R_s [Ωcm²]	A	J_0 [mA/cm²]
375, 550 [°C]	8.5	82.6	26.5	0.2	12.4	20.72	1.9	0.92
400, 550 [°C]	4.8	220.1	30.3	0.3	68.1	16.53	2.6	0.12
425, 550[°C]	10.2	242.0	29.0	0.7	31.0	10.70	1.9	0.14

Among the films annealed in long first steps (Figure 56), the one the first step at higher temperature (425°C), shows also the higher Jsc and Voc with consequently, the highest efficiency of this study. High first step temperature improves collection of charges and helps in the formation of a better p-n junction.
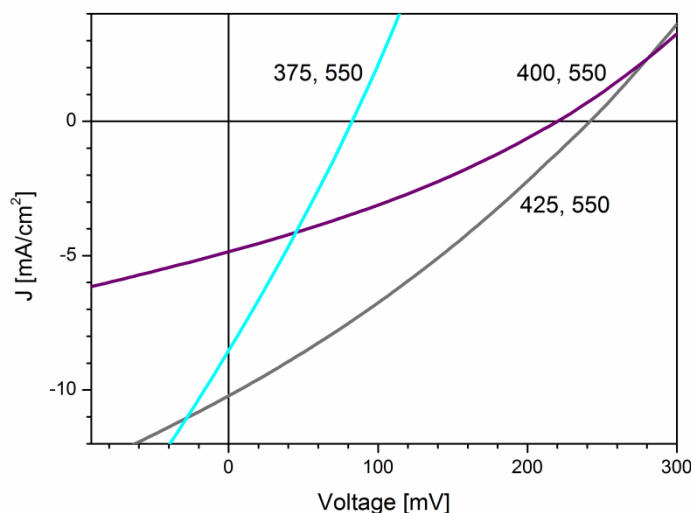
Figure 56. J-V curves of long time first steps annealing.

The most representative devices of this section are shown in Figure 57 in a SEM cross section view. In both cases compact films can be observed, formed by small grains (~100nm) equal sized thought the depth of the films. In Figure 57a the space in the back contact/absorber could have been produced during cutting the sample. Mo back contact has been partially selenized in both cases.
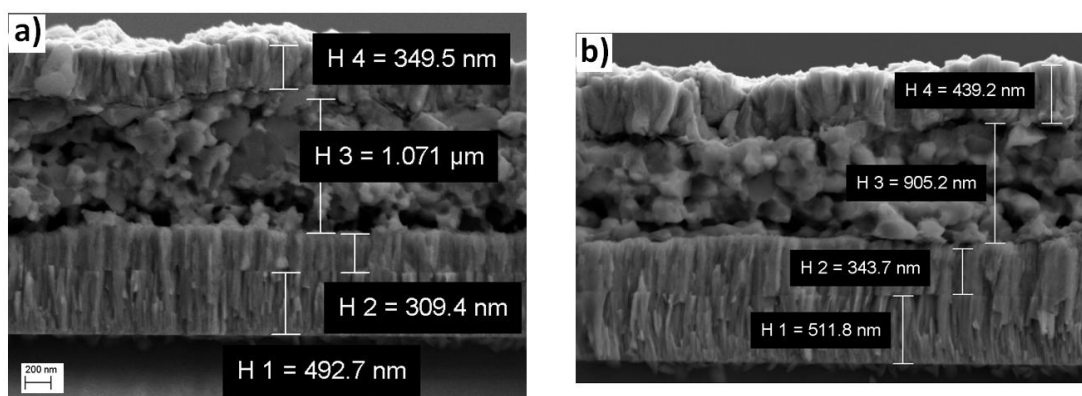
Figure 57. SEM cross section images of solar cell devices annealed in separate two step process: (a) 400, 500 and (b) 425, 550.

Long first steps and short second steps work well compared with the opposite, however the chalcogen content in our best sample (left gray triangle in Figure 55) is S/(S+Se) = 0.38 ±0.09 which is still high if compared with the world record device[9] with S/(S+Se) = 0.28. Our number is high not due to low Se content but because of high S content.

Those results confirm what has been earlier stated:

> *In the selenization of sprayed CZTS thin films, given the explored annealing conditions, there exists a limit within the S and Se content on the annealed films.*

The limit resides on the experimentally proved fact that it is a difficult matter to reduce by selenization the S content on the films without kesterite decomposition. Here we found two conjugated variables:

x.   Selenization

xi.   Remain of sulfur content after selenization

It could have been possible and experimentally feasible to design and perform many other selenization experimental plans in the direction of first steps with increased temperature and duration. However it was decided to rethink the selenization of sprayed CZTS thin films from alcohol-based solutions, as it seems we were facing a strong boundary limit related with the precursor solution itself.

4.2.6.1 Precursor solution reformulation

As we have explore in a moderately ample way the first variable (selenization), the next action plan was in the direction of the source of the problem; the concentration of sulfur in the precursor solution. For this reason, the reformulation of the precursor solution was proposed in order to decrease the sulfur content on the as-sprayed films by the diminution of thiourea in the precursor solution as thiourea is, in this entire thesis the source of sulfur to the as sprayed CZTS films. Different sulfur concentrations were used as shown in Table 25

The first, 50mM is the standard concentration of thiourea; it is a thiourea excess, used to compensate the loss of sulfur during the spray deposition. For these experiments, the concentration of metals in a methanol + water (50%, v/v) solution was kept constant to 7.2mM, 5.4mM and 4.95mM for $CuCl_2.2H_2O$, $Zn(CH_3CO_2)_2$ and $SnCl_4.2H_2O$ respectively.

As was earlier mentioned, thiourea acts as a complexing agent in the solution and is the last precursor to be added to the solution. When it is added to the metal ions in solution, an exothermic chemical reaction is experienced by the species in solution; as a result the solution temperature increases ~4°C. The reduction of thiourea concentration down to 35mM was discarded due to the fast precipitation of metallic species (<3 minutes) as a result of the high proportion of uncomplexed metallic species.

The kinetic of precipitation was reduced by the use of a thermostatic water bath to keep the temperature of the solution equal to 20±2°C. The solution was prepared by first dissolving the metallic salts in the solvent. After that, a water-based solution containing thiourea was added drop by drop as the solution was continuously stirred. At this step the colour of the solution was red-brown becoming transparent whit the continuous addition of thiourea. It was only helpful in gaining time before a slow precipitation of the solution after about 10 minutes (TU = 40mM). This time with transparent solution is not enough to set the spray system ready and to perform a full spray deposition process. For the precursor solution prepared whit low sulfur concentrations, the solution moved from red-brown to dense white as result of precipitates.

One other possible way to avoid the precipitation of the solution is to prepare it in a more acid media. The standard starting solution has a pH ≈ 3, this pH value is need to maintain the metals in solution. It is mainly the Sn precursor that rapidly precipitates with temperature or in basic medias.

Solutions with different pH values in the range 1-3 were prepared, the change in the pH value was carried out by adding HCl (37% w/v) previous to the incorporation of thiourea. The results are shown in Table 24, precursor solutions with the highest thiourea concentration (40mM and 50mM) showed to be stable over all the pH range under investigation; they remained stable over almost two days. Precursor solutions with thiourea concentrations of 35mM showed a slow precipitation formation (3-1.5 pH) and a considerable good stability for pH ≈ 1 however, it is a too acid solution to work with using a metallic spray nozzle. Precursor solutions with the lowest thiourea concentration (30-10mM) precipitate immediately after adding thiourea going from liquid-like brownish precipitates to semi-solid white precipitates.

Table 25. Summary of precursor solution stability by changing pH and thiourea concentration.

Solution pH	Sulfur concentration [mM]					
	50	40	35	30	20	10
3	stable	stable	slow	precipitate	precipitate	precipitate
2.5	stable	stable	slow	precipitate	precipitate	precipitate
2	stable	stable	slow	precipitate	precipitate	precipitate
1.5	stable	stable	slow	precipitate	precipitate	precipitate
1	stable	stable	stable	precipitate	precipitate	precipitate

The use of solutions with low pH values corrodes the nozzle after some spray runs thus the use of them was avoided; from the system and user point of view, a neutral solution is preferred for spraying. From the results above, a minimum concentration of thiourea is needed to maintain a stable solution.

Fresh precursor solutions with pH ≈ 3 and with thiourea concentrations of 40mM, 30mM and 20mM were sprayed to measure the composition of the films. The 10mM thiourea concentration was not used for the well preservation of the system.

Table 26 shows composition and thickness of the as sprayed films by using different thiourea concentrations. The strong variation in the composition is related first, to the reduced sulfur content on the films (samples B, C and D) that changes the atm% of the other elements and, second to the relative increase in Sn content in the films.

Table 26. Composition of as sprayed films as function of thiourea concentration.

Sample	Thiourea [mM]	$\dfrac{Cu}{Zn+Sn}$	$\dfrac{Zn}{Sn}$	$\dfrac{Cu}{Zn}$	$\dfrac{Cu}{Sn}$	$\dfrac{S}{M}$	Thickness [µm]
A	50	0.75	1.17	1.42	1.62	0.80	1.1
B	40	0.60	1.29	1.08	1.36	0.72	0.56
C	30	0.49	1.35	0.88	1.14	0.52	0.39
D	20	0.34	0.52	1.00	0.53	0.25	0.22

From Table 26 it is clear the effect thiourea has not only on the S content of in the films but also in the final thickness and average composition of the as sprayed films. Sample A is the result of a long optimization road of as sprayed films; it means that using Ar as carrier gas and Mo coated SLG, the gas pressure, heating profile, substrate temperature, precursor solution, precursor solution flow, inner chamber pressure and post spray cooling process was optimized as described in Chapter 2.

Figure 58 shows the effect of reducing the thiourea content on the S/M ratio and film thickness. It is a well example of the strong link that the spray parameters have on each other. In this case only the concentration of one of the precursors was changed but this change affected the two main properties of the spray films: thickness and composition.
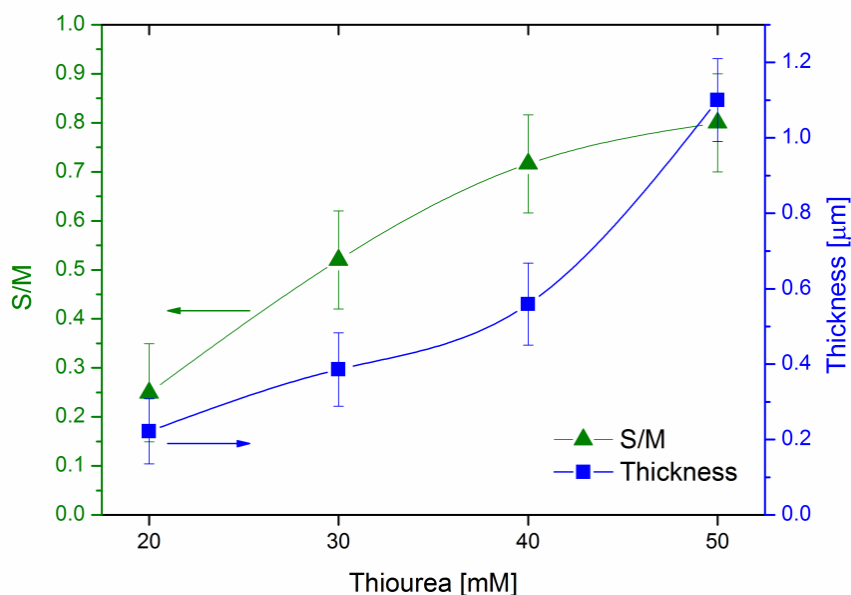
Figure 58. Sulfur on metals (S/M) ratio and thickness of as sprayed films using different thiourea concentrations on the precursor solution.

The point of reducing the thiourea concentration in the precursor solution is to obtain as-sprayed films with reduced sulfur content. Those films after been selenized should have even lower sulfur content which would allow to obtain S/(S+Se) < 0.38.

The only starting solution with reduced thiourea concentration that was stable and transparent the enough time to finish a deposition process is the one with -20% in thiourea content (TU = 40mM). However, the composition of as sprayed films using this

thiourea composition in the precursor solution needs to be optimized (sample B, Table 26) The optimization of the metal rations using the mentioned thiourea concentration (with pH ≈ 3) is shown in Table 27. In order to obtain films with ~1μm in thickness the spraying time was set to 20min.

Table 27. Optimization of the metallic ratios for a reduced TU concentration in the precursor solution.

Sample	*Precursor solution concentration*					*Ratios on as sprayed films*				
	$\dfrac{Cu}{Zn+Sn}$	$\dfrac{Zn}{Sn}$	$\dfrac{Cu}{Zn}$	$\dfrac{Cu}{Sn}$	$\dfrac{S}{M}$	$\dfrac{Cu}{Zn+Sn}$	$\dfrac{Zn}{Sn}$	$\dfrac{Cu}{Zn}$	$\dfrac{Cu}{Sn}$	$\dfrac{S}{M}$
B	0.70	1.09	1.33	1.45	2.29	0.60	1.29	1.08	1.36	0.72
E	1.01	1.16	1.89	2.20	1.99	0.87	1.66	1.40	1.78	0.75
F	1.00	1.20	1.82	2.20	1.97	0.99	1.41	1.71	1.50	0.87
G	0.96	1.12	1.82	2.04	2.00	0.75	0.99	1.52	1.49	0.89
H	0.98	1.08	1.89	2.04	1.95	0.83	1.12	1.59	1.23	0.86

Table 27 shows the iterative process to obtain films with the pursued composition; sample H is a good example of a sprayed film with the appropriate composition. After using a reduced concentration of thiourea in the starting solution, a lower concentration of metals was need too. However, the concentration of metals (or thiourea) is not an issue in the spray systems, they come from salts (chlorides in this case) and its price is much lower than that of the pure metals used in the vacuum techniques. However the spraying time was doubled which in a first approximation represents twice the usage of resources (solvents, precursors, compressed gas, electrical power and time). From the resources perspective, it is not worthy to reduce the thiourea content if the other resources ought to be doubled.

On the other hand, the final aim of reduced the thiourea content in the solution neither was nor achieved; the film with optimized composition has more or less the same S/M content (sample H) than the films with not reduced thiourea content in the precursor solution (sample A). The deposition of CZTS by SP is then, a compositional self adjusting process for the range of metallic ratios we are interested in. In summary, we were looped to the starting compositional point; it really brings an end to the composition and parameters optimization of the SP.

4.3 Application to novel photovoltaic architectures

This section is partially based on the publication: *Espindola-Rodriguez, M. et al. Cu$_2$ZnSnS$_4$ absorber layers deposited by spray pyrolysis for advanced photovoltaic technology. Physica Status Solidi (a) (2014).*

4.3.1 Glass/ZnO nanorods/Sprayed Kesterite

Once demonstrated the potentiality of SP for the fabrication of standard substrate configuration thin film solar cells, in this section SP is demonstrated as an effective thin film absorber deposition technique to coat metal oxide nanostructures, particularly ZnO nanorods arrays (ZnO NRA). Up to date, the only available publication dealing with the coating of metallic oxide nanostructures by SP for advanced photovoltaic technology belongs to IREC's solar group and is the current section of this thesis[74]. The combination of cost-effective technologies and nanostructures leads to a new knowledge frontiers in photovoltaic technologies which makes of it a very interesting research area.

The use of metal oxide nanostructures in solar cells opens a wide range of new device applications. Such as excitonic solar cell systems[131, 132], inorganic extremely thin absorber concept devices[133] and anti-reflective-coatings for thin film chalcopyrite solar cells[134, 135].

These ordered nanostructures increase light capture via diffused reflections between nanostructure arrays, enhancing the charge separation and transport thanks to their unique inherent morphological, electrical, and optoelectronic properties (e.g., their high surface-to-volume ratio).

The use ZnO NRA allows new solar cell architectures in thin film devices. Figure 59 presents schematically different solar cell configurations incorporating ZnO NRA. A standard substrate configuration CZTS-based device is shown in Figure 59(a). Some of the possible new nanorod architectures are, namely, a substrate device with an anti-reflective coating of ZnO NRA (Figure 59 (b)), a superstrate device (Figure 59 (c)) using ZnO NRA to reduce the thickness of the absorber and a bifacial device (Figure 59 (d)).

This section focuses on the combination of ZnO NRA and sprayed CZTS for superstrate and future bifacial applications. Some attempts of bifacial CZTS-based solar cells with flat layers have been reported[136-138]. The bifacial solar cell is useful in specific situations such as building integrated applications (façades, roofs, etc.) which receive direct or reflected sunlight from both sides. In principle, a bifacial solar cell can also be used as a top cell in tandem devices when combined with a bottom photovoltaic solar cell with a smaller band gap or a solar thermal cell, which utilizes the infra-red part of the spectrum. Optical losses are reduced, and thereby solar cell performance is enhanced due to the antireflective effect derived from ZnO nanorod at the TCO interface. The nanorods may also increase the carrier extraction as they penetrate into the absorber and thus decrease the path of the carriers to the electrode.
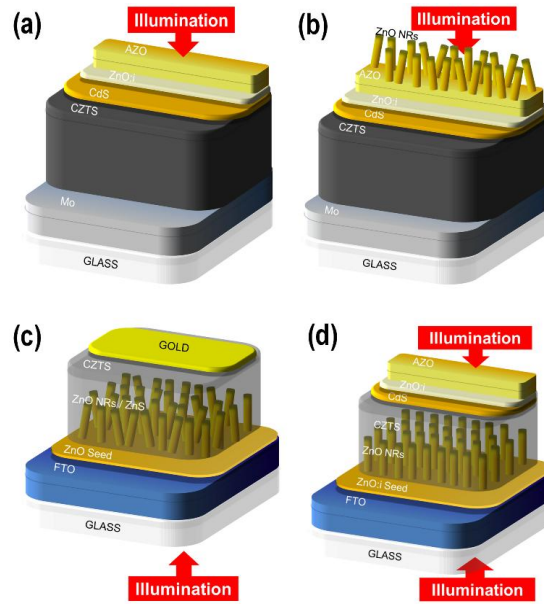
Figure 59. Scheme of (a) Standard CZTS substrate solar cell stack, (b) substrate device with a nanorod array anti-reflection coating, (c) ZnO NRA superstrate device and (d) nanorod array bifacial solar cell.

CZTS thin films were sprayed on ZnO NRA electrochemically grown[139] on 2.5x2.5cm^2 RF-sputtered SnO$_2$:F (FTO) coated soda lime glass substrates (SLG). The as grown ZnO NRA are shown in the Figure 60, they are ~400nm in length and ~60nm in diameter.
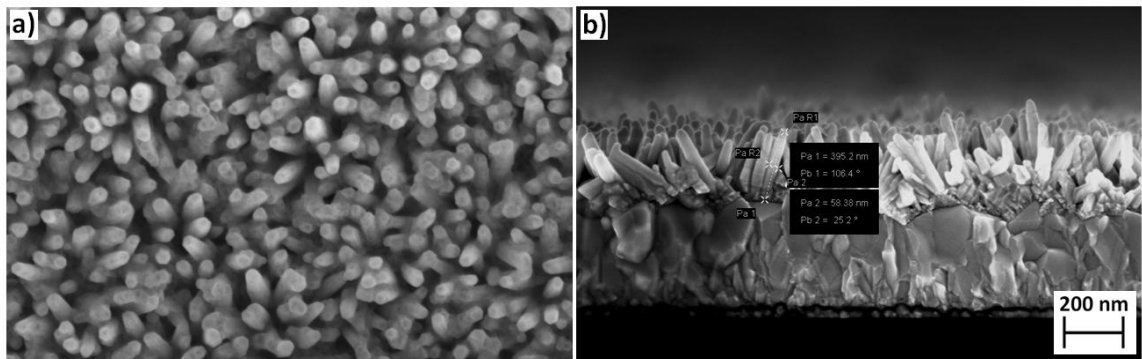
Figure 60 (a) top and (b) cross section SEM views of as grown FTO/ZnO NRA

Fresh precursor spray solutions were prepared for each sample with 50% H$_2$O + CH$_3$-OH (v/v) using: C^{II}C, ZAc, T^{IV}C and TU (7.2mM, 5.4mM, 4.955mM and 50mM, respectively).

In order to facilitate the formation of a sprayed thin film of CZTS on the nanorods, the carrier gas pressure, the solution flow and growing time were optimized to 1.5 bar, 2ml/min and 2 minutes respectively, the substrate temperature was held at 235 °C using Ar as carrier gas following the optimized temperature profile earlier described. The reason to use a slow solution flow of 2 ml/min, is to preserve the orientation of the nanorods perpendicular to the substrate.

Figure 61 shows coated nanorods after 30 seconds of spraying using the optimized conditions. It is clearly seen how the ZnO NRA are completely covered by ~50nm of CZTS, preserving its orientation if compared with Figure 60b. It demonstrates that SP is a suitable technique for the deposition of thin films layers of CZTS in nanostructured substrates, in contrast with PVD techniques that does not allow absorber materials to penetrate the ZnO nanorod structure.
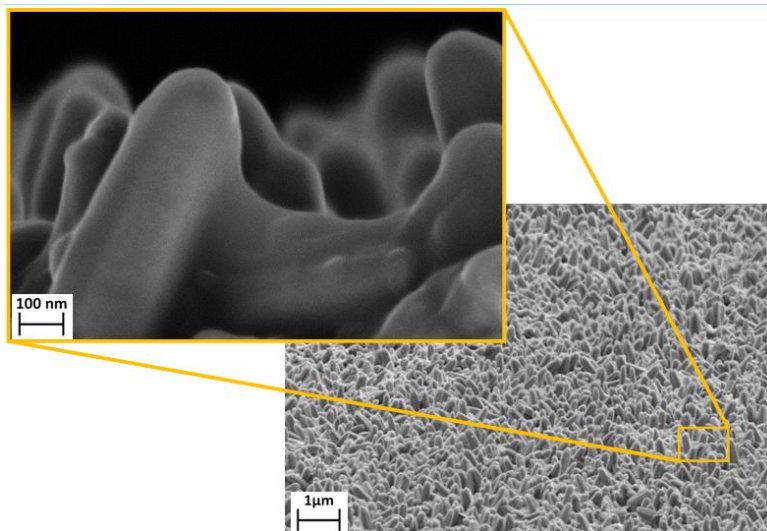
Figure 61. Top SEM images of ZnO NRA spray-coated after 30s.

After 2 minutes of deposition, as it will be latter supported by Raman spectroscopy a ~100nm CZTS layer is formed in the top of the ZnO NRA after filling the space between them as seen in Figure 62. Some of the longer nanorods are fully embedded in the film although their peaks are covered by only a thin layer of the sprayed film; this correlates with the presence of the ZnO characteristic peaks in the top Raman scattering with UV excitation wavelength. Longer deposition times indeed produce ticker films but modify the orientation of the nanorods.
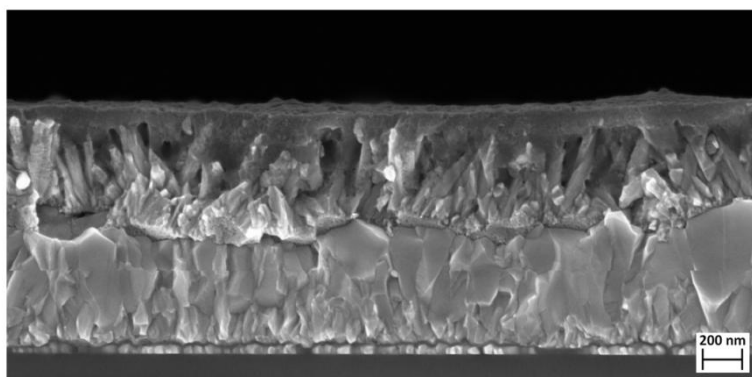
Figure 62. SEM cross section of ZnO NRA spray-coated after 2 minutes.
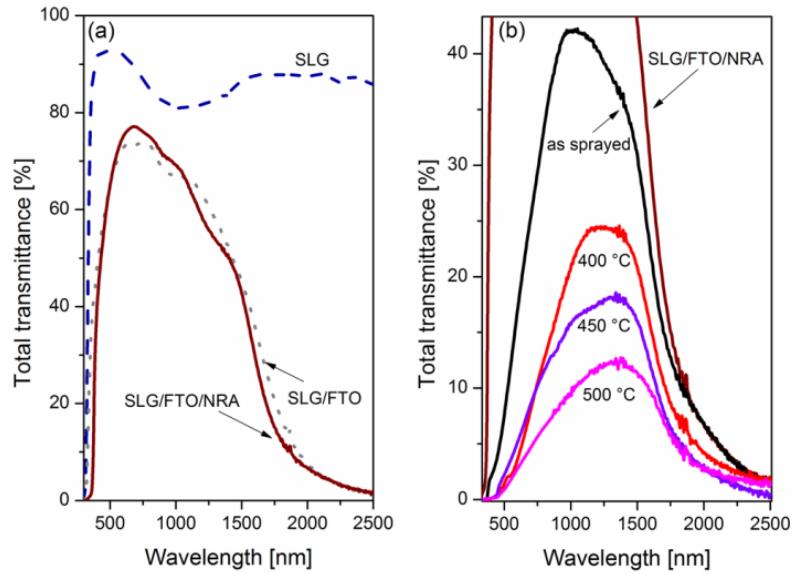
Figure 63. Optical transmission of the different layers on the nanostructured substrates. (a) reference SLG/FTO/NRA, (b) as sprayed and annealed samples at different temperatures.

After deposition, the samples were submitted to a reactive one-step thermal annealing, at 400°C, 450°C and 500°C for 20 minutes. Figure 63a shows the optical transmittance (air as reference) of the SLG substrate, SLG/FTO window and SLG/FTO/NRA structure. Figure 63b shows the transmission of SLG/FTO/NRA/CZT(S,Se) as grown and annealed samples. The transmission of the annealed films decreases as both, the film thickness and the absorption increases. This shows that it is possible to use SP as a deposition technique to obtain semi-transparent sprayed kesterite thin films on nanostructured window layers.

After 20 min selenization at 400 °C, CZT(S,Se) grains are formed above the NRA (Figure 64a), as revealed by XRD and Raman. After selenization at 500 °C, the NRA disappears (Figure 64c) but still ZnO is detected on the films as well as ZnSe.
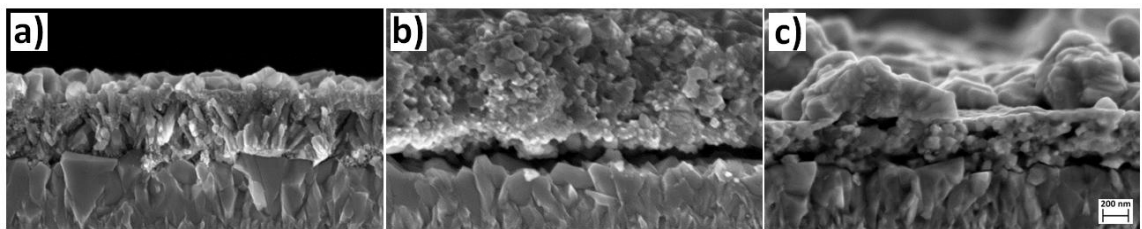
Figure 64. Cross-sectional SEM view of annealed samples 400°C (a), 450°C (b) and 500°C (c).

Figure 65 shows the XRD pattern of as sprayed and annealed samples at three annealing temperatures. The as sprayed film shows ZnO peaks at $2\theta = 34.5°$, $36.3°$ and $47.3°$ corresponding to the (002), (101) and (102) planes respectively, as well as the main SnO_2 peaks of the tetragonal crystalline system. After the selenization at 400°C, a new intense ZnO peak appears at $2\theta = 31.7°$ ((100) plane) indicating a change in the ZnO NRA. At this annealing temperature, we also found the presence of SnSe at $2\theta = 31.3°$ and $37.7°$, its

presence could be linked to condensation from the atmosphere. SnSe is still present after the 450°C annealing treatment but not after annealing at 500°C. However the diffraction peak at 31.3° can also be attributed to Cu_2SnS_3 as well as the ones observed at 42.4° and 46.2°. After annealing at 450 °C and 500 °C characteristic peaks related with the formation of CZT(S,Se) appear as it can be seen in figure 10. Additionally an intense peak at about $2\theta = 45.3°$ can be attributed to CT(S,Se) or ZnSe. Annealing at higher temperatures promotes the decomposition of the NRA[140] demonstrating that a temperature between 450 °C and 500 °C is the upper thermal limit for this technology, in order to preserve the ZnO NRA morphology.
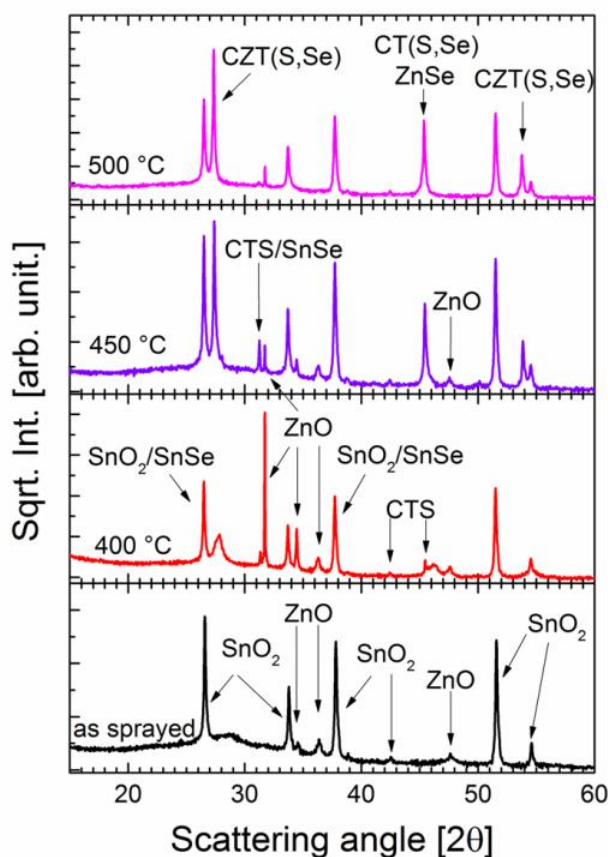
Figure 65. XRD pattern of the as sprayed SLG/FTO/NRA/Kesterite sample (bottom) and after annealing at three different temperatures.

In Figure 66 the Raman spectra of the SLG/FTO/NRA/Kesterite samples are shown. The peaks in the as sprayed sample (sprayed at 235 °C) show a typical spectrum corresponding to a CZTS films with a low crystalline quality. After thermal annealing of each sample, Se was incorporated in the films resulting in the appearance of the corresponding CZT(S,Se) selenium-rich spectrum. However broad peaks are observed that could be related to chemical disorder induced for the S-Se alloy, and/or crystal disorder effects. A red shift is also observed from 204.8 cm⁻¹ to 196.8 cm⁻¹ and also a remarkable reduction in the intensity of the CZT(S,Se) peak in the 300-400 cm⁻¹ range after increasing the annealing temperature. This change is due to a better selenization of the absorber.
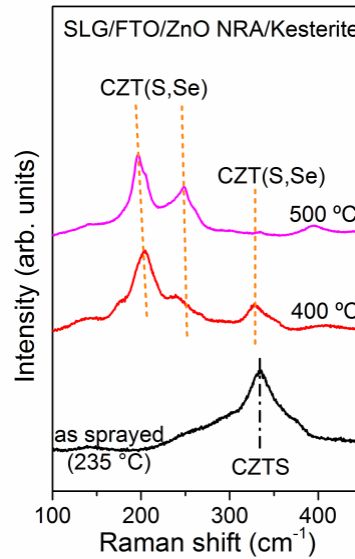
Figure 66. Top Raman spectra using 532 nm excitation wavelength of as sprayed selenized samples.

The Raman surface spectra using 325 nm excitation wavelength for the as-sprayed and selenised samples are shown in Figure 67. Additionally, two reference spectra are presented, one corresponding to a sputtered i:ZnO compact film and the other to ZnO NRA. All Raman measurements show the characteristic peaks of ZnO but in the case of the sprayed samples, it is an indication that some ZnO nanorods have not been totally covered by the sprayed film (due to protruding peaks of longer nanorods, as explained above).

In Figure 67 the first and second order vibrational modes of ZnO are present in all the spectra, the evolution of the modes in the NR shadowed region reveals the recrystallization of the NRA as the annealing temperature increases. With the annealing process, ZnSe is formed from the Zn excess as a result of the decomposition of the NRA as confirmed by the presence of the mode at 250 cm^{-1} characteristic of this binary phase. The 2θ peaks position from XRD of this binary, matches well with the ones of kesterite and ZnSe. However by using this resonant Raman conditions we can confirm the presence of the binary compound. Also at 203 cm^{-1} the presence of a CZT(S,Se) characteristic peak is observed, showing that the annealing conditions need to be optimized for this specific substrate configuration. The results in this section demonstrate the feasibility of spray pyrolysis technique for advanced nanostructured PV devices concepts.
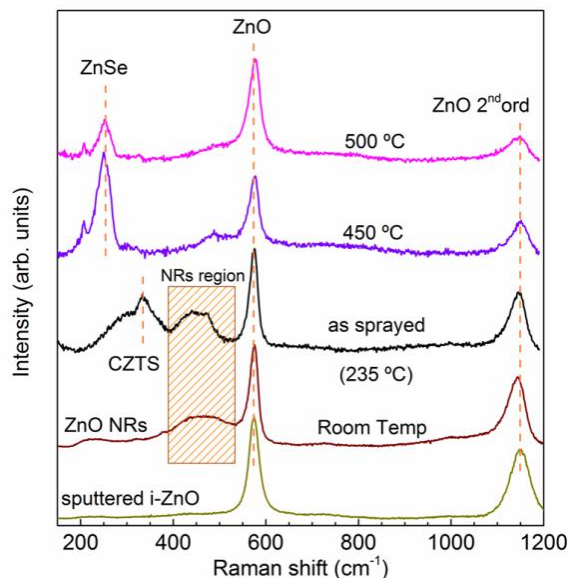
Figure 67. Top Raman of the SLG/FTO/ZnO NRA/Kesterite samples using 325 nm excitation wavelength. The spectra of the as sprayed and samples selenized at different temperatures are shown. Also as a reference the spectra of a i-ZnO layer.

In this study 450°C seems to be the upper temperature. The possibility of working in the optimization selenization process of nanostructures substrates is now open to obtain high quality CZT(S,Se) absorbers to be used as semitransparent solar cells with novel architectures. It sets new frontiers to the applicability of SP as cost-effective deposition technique of nanostructurated devices.

4.4 Summary

Two different alcohols were used in mixture with water as alternative solvents with them, a systematic study of two main selenisation variables was presented; the selenisation profile, temperature and Se amount during annealing time was additionally investigated. We demonstrate that after applying different selenization conditions, the CZTS sprayed films are an all cases Se-rich but not S-free. High annealing temperatures are mandatory to obtain highly crystalline CZTSe films as revealed by the minor X-ray diffraction reflections and the identified Raman modes. However, a too high annealing temperature promotes kesterite decomposition due to both the time and temperature.

The Selenisation of CZTS-spray precursors opens a new alternative to obtain high efficiency devices, the deposition technique has demonstrated to be cost effective with increasing values of power conversion efficiency capable to be use as coating technique of nanostructurated substrates. Here we report a device with η = 1.9%. This conversion efficiency value is encouraging to continue working on the direction to improve it.

5 CONCLUSIONS AND FUTURE WORK

In this thesis the capabilities of a *cool-wall vertical pneumatic spray pyrolysis* (SP) system were shown as a synthesis technique of Cu_2ZnSnS_4 (CZTS) based materials, called kesterite. The main advantage of this system is that it is capable of working in a controlled atmosphere, and in this thesis the results of spraying in air, Ar and $Ar-H_2$ are explored and discussed. Different solvents and metal salts were used to obtain as-sprayed films with the appropriate properties, to be used, after a high temperature thermal annealing, as absorber materials for thin film solar cells. Those solar cells were obtained without the use of any toxic or explosive regents and process gases. Films obtained by SP offer a cost effective solution-based alternative to the high-vacuum deposition techniques.

The central idea of this thesis was to produce novel materials in a classical cost effective system by equipping the system with modern and unique capabilities with the final objective of produce efficient thin film solar cells. Thought the pages of this thesis the objective is fulfilled by the study of two different kesterite materials: CZTS and $Cu_2ZnSn(S_xSe_{1-x})_4$ (CZTSSe). The former was studied by spraying aqueous precursor solutions using air or Ar as carrier gases and the latter by using alcohol-based precursor solutions using Ar or $Ar-H_2$ as carrier gas.

Kesterite materials are narrowly composition sensitive; in addition to that, the formation of unwanted binary or ternary phases is hard to avoid. In sprayed kesterite films, ZnO is easily formed during the spray process; this oxide along with the small crystal size of the films and its high surface roughness hinders the performance of the solar cells from sprayed absorbers. It was found by UV Raman (325nm) measurements that when using Ar or $Ar-H_2$ as carrier gas instead of air, no more evidence of ZnO was detected after sulfurization, with bigger grains resulting in an overall improvement in the optoelectronic parameters of the CZTS-based solar cells. Improved power conversion efficiency of 1.4% and 0.65% for Ar and $Ar-H_2$ sprayed films, compared with the best power conversion efficiency of air sprayed CZTS-based solar cells of 0.49% are obtained in this thesis

demonstrating the potentiality of the developed methodology. It was the ultimate motivation of keep using Ar as carrier.

After the encouraging results of the CZTS-based solar cells it was decided to produce CZTSSe-based solar cells from the selenization of as-sprayed CZTS films. Some variations were here included like the use of alcohol-based precursor solutions and the use of a pre annealing Br_2-MeOH etching to reduce the roughness of the films. Due to the reduced surface tension of the alcohol-based solutions, the formation of smaller spray drops is facilitated; from that drops the solvent can be easily and faster evaporated producing more compact films. The best power conversion efficiency of the devices presented in this thesis is from a CZTSSe-based solar cell with 1.9%.

Inside the margins of a cost-effective route to synthesize CZTSSe materials, this thesis also shows the beneficial impact of Na doping, by dipping the samples in NaCl (1M); a fast, affordable and easy to do doping technique. The best results, in terms of power conversion efficiency were obtained on the samples that were dipped in NaCl (1M) after etching the surface with Br_2-MeOH previous to the annealing step. It traces the way for other dopants and doping approaches.

This thesis shows the possibilities of kesterite materials obtained by SP for photovoltaic applications but many research topics are still open. The key to improve resides in both SP system and precursor solution. The relative nozzle-to-substrate movement will highly improve the film thickness homogeneity covering bigger areas, as desired in an industrial perspective. Additionally a reformulation of the precursor solution will also guide to higher efficiencies by using for example out stoichiometry colloidal Cu-Zn-Sn-S solutions as recently showed.

THIS THESIS WORK CONTRIBUTIONS

This thesis oral contributions

1. **M. Espindola-Rodriguez**, M. Placidi, V. Izquierdo-Roca, X. Fontané, A. Fairbrother, D. Sylla, O. Vigil-Galán, E. Saucedo, A. Pérez-Rodríguez. *"Optimización de las propiedades de películas de Cu_2ZnSnS_4 obtenidas por spray pirolisis neumático para ser usadas en celdas solares".* Oral, Solid State Physics Group Seminars, June 2012, México, México.

2. **M. Espindola-Rodriguez**, E. Saucedo. *"Review of the spray pyrolysis technique: application to the synthesis of Kesterite".* Oral, KESTCELLS Seminars: Chemical routes for the synthesis of Kesterites, July 2013, Barcelona, Spain.

3. **M. Espindola-Rodriguez**, D. Sylla, S. López-Marino, Y. Sánchez, M. Placidi, X. Fontané, A. Fairbrother, J. López-Garcia, V. Izquierdo-Roca, E. Saucedo, O. Vigil-Galán and A. Pérez-Rodríguez. *"Characteristics of spray-deposited Cu_2ZnSnS_4 thin films under inert atmosphere and its use in photovoltaic devices".* Oral EUROMAT September 2013, Seville, Spain.

4. **M. Espindola-Rodriguez**, S. López-Marino, A. Fairbrother, D. Sylla, Y. Sánchez, M. Placidi, H. Xie, X. Fontané, J. López-Garcia, V. Izquierdo-Roca, O. Vigil-Galán, E. Saucedo, and A. Pérez-Rodríguez. *"Tecnologías fotovoltaicas sostenibles de capa fina basadas en calcogenuros emergentes formados por elementos abundantes en la corteza terrestre: retos y perspectivas".* Oral, XIII Congreso Nacional de Materiales, June 2014, Barcelona, Spain.

5. **M. Espindola-Rodriguez**, Y. Sánchez, D. Sylla, S. López-Marino, M. Placidi, X. Fontané, V. Izquierdo-Roca, W. Ohm, S. Gledhill, A. Pérez-Rodríguez, O. Vigil-Galán, and E. Saucedo. *"Selenisation study of sprayed Cu_2ZnSnS_4 thin films for photovoltaic applications".* Invited Oral, XXIII I-MRS, August 2014, Cancun, México.

This thesis poster contributions

1. O. Vigil-Galán, **M. Espindola-Rodriguez**, D. Olarte-Jiménez *"CZTS contacts for CdS/CZTS solar cells: effect of different metals on specific contact resistance".* Poster, 2nd European Kesterite Workshop, November 2011, Barcelona, Spain.

2. **M. Espindola-Rodriguez**, O. Vigil-Galán, V. Izquierdo-Roca, X. Fontané, F.A. Pulgarín, D. Sylla, A. Fairbrother, E. Saucedo, A. Pérez-Rodríguez. *"On the optimization of the composition of photovoltaic grade Cu_2ZnSnS_4 layers grown by pneumatic spray pyrolysis".* Poster, E-MRS Spring Meeting, May 2012, Strasburg, France.

3. **M. Espindola-Rodriguez**, O. Vigil-Galán, X. Fontané, D. Sylla, A. Fairbrother, E. Saucedo, A. Pérez-Rodríguez. *"Influence of starting-solution precursors concentration on the properties of spray-deposited CZTS thin films".* Poster, XXI I-MRS, August 2012, Cancun, México.

4. **M. Espindola-Rodriguez**, D. Sylla, X. Fontané, M. Placidi, A. Fairbrother, S. López, V. Izquierdo-Roca, E. Saucedo, O. Vigil-Galán, A. Pérez-Rodríguez. *"On the*

compositional issues in the preparation of Cu₂ZnSnS₄ films by spray pyrolysis technique under inert atmosphere". Poster 3ʳᵈ European Kesterite Workshop, November 2012, Luxemburg, Luxemburg.

5. <u>M. Couriel-Pedriahita,</u> **M. Espindola-Rodriguez,** O. Vigil-Galán, "Dependencia de la formación de fases secundarias con la composición química en películas delgadas de Cu2ZnSnS4 depositadas por rocío químico neumático", VI Taller de Física de la Materia Condensada y Molecular, January 2013, Sciences Faculty of Morelos University, Morelos, México.

6. M. Guc, **M. Espindola-Rodriguez,** L. I. Bruc, K. G. Lisunov, L. Dermenji, N. Curmei, D. A.Sherban, A. V.Simashkevich, E. Saucedo, A. Perez-Rodriguez and E. K. Arushanov. *"Transport properties of kesterite thin films of Cu₂ZnSnS₄ obtained by spray pyrolysis".* Poster, 28ᵗʰ EU PVSEC, October 2013, Paris, France.

7. **M. Espindola-Rodriguez,** D. Sylla, Y. Sanchez, S. López-Marino, O. Rogee, J. López-García, M. Placidi, O. Vigil-Galán, A. Perez-Rodriguez, E. Saucedo. "*Selenisation study of sprayed Cu₂ZnSnS₄ thin films obtained by spray pyrolysis".* Poster 29ᵗʰ EU PVSEC, September 2014, Amsterdam, Nederland.

This thesis published articles

1. **M. Espindola-Rodriguez,** M. Placidi, O. Vigil-Galán, V. Izquierdo-Roca, X. Fontane, A. Fairbrother, D. Sylla, E. Saucedo, A. Pérez-Rodríguez, *"Compositional optimization of photovoltaic grade Cu2ZnSnS4 films grown by pneumatic spray pyrolysis",* Thin Solid Films, 535 (2013) 67-72.

2. **M. Espindola-Rodriguez,** J. López-García, D. Sylla, X. Fontané, Y. Sánchez, S. López-Marino, V. Izquierdo-Roca, W. Riedel, W. Ohm, S. Gledhill, O. Vigil-Galán, E. Saucedo, *"Cu₂ZnSnS₄ absorber layers deposited by spray pyrolysis for advanced photovoltaic technology",* Physica Status Solidi (a), (2014).

3. **M. Espindola-Rodriguez,** D. Sylla, Y. Sanchez, S. López-Marino, X. Fontané, J. López-García, M. Placidi, A. Pérez-Rodríguez, O. Vigil-Galán, E. Saucedo, *"Pneumatically sprayed Cu₂ZnSnS₄ films under Ar and Ar–H₂ atmosphere",* Journal of Physics D: Applied Physics, 47 (2014) 245101.

4. O. Vigil-Galán, **M. Espindola-Rodriguez,** M. Courel, X. Fontané, D. Sylla, V. Izquierdo-Roca, A. Fairbrother, E. Saucedo, A. Pérez-Rodríguez, *"Secondary phases dependence on composition ratio in sprayed Cu2ZnSnS4 thin films and its impact on the high power conversion efficiency",* Solar Energy Materials and Solar Cells, 117 (2013) 246-250.

5. O. Vigil-Galán, M. Courel, **M. Espindola-Rodriguez,** V. Izquierdo-Roca, E. Saucedo, A. Fairbrother, *"Toward a high CZTS solar cell efficiency processed by spray pyrolysis method",* Journal of Renewable and Sustainable Energy, 5 (2013).

6. M. Courel, O. Vigil-Galán, D. Jiménez-Olarte, **M. Espindola-Rodriguez,** E. Saucedo, *"Trap and recombination centers study in sprayed Cu2ZnSnS4 thin films"*, Journal of Applied Physics, 116 (2014).

7. O. Vigil-Galán, M. Courel, J.A. Andrade-Arvizu, Y. Sánchez, **M. Espindola-Rodriguez,** E. Saucedo, D. Seuret-Jiménez, M. Titsworth, *"Route towards low cost-high efficiency second generation solar cells: current status and perspectives",* J Mater Sci: Mater Electron, (2014) 1-12.

8. O. Vigil-Galán, M. Courel, **M. Espindola-Rodriguez,** D. Jiménez-Olarte, M. Aguilar-Frutis, E. Saucedo, *"Electrical properties of sprayed Cu2ZnSnS4 thin films and its relation with secondary phase formation and solar cell performance"*, Solar Energy Materials and Solar Cells, 132 (2015) 557-562

OTHER CONTRIBUTIONS

Other oral contributions

1. **M. Espindola-Rodriguez,** O.Vigil-Galán, M. Tufiño-Velázquez, F. Cruz-Gandarilla and G. Contreras-Puente. *"Physical properties of Cu_xTe films compounds on CdTe films formed by the deposition of Te and Cu".* Oral, XXX Reunión anual de la Sociedad Mexicana de Ciencia y Tecnologia de Superficies y Materiales, Septiembre 2010, Quintana Roo, México.

2. **M. Espindola-Rodriguez,** O.Vigil-Galán, J.-Santoyo, M. Tufiño-Velázquez, F.Cruz-Gandarilla y G. Contreras-Puente, *"Desarrollo de contactos posteriores de Cu_xTe en celdas solares de CdS/CdTe formados por depósito de Te y Cu",* Oral, 4to Taller de Física de la Materia Condensada y Molecular, Enero 2011, Facultad de Ciencias, Cuernavaca, Universidad Autónoma del Estadio de Morelos, México.

3. J. Santoyo, O.Vigil-Galán, **M. Espindola-Rodriguez,** E. Marín, "Depósito de películas delgadas por la técnica modificada de evaporación en espacio cerrado en paredes calientes usando pastillas de materiales sinterizados: aplicación en la fabricación de celdas solares de CdS/CdTe", 4to Taller de Física de la Materia Condensada y Molecular, Enero de 2011, Facultad de Ciencias, Cuernavaca, Universidad Autónoma del Estadio de Morelos, México.

4. J. Santoyo, O.Vigil-Galán, E. Franco, **M. Espindola-Rodriguez,** E. Marin "Procesamiento y caracterización de celdas solares del tipo CdS/CdTe mediante materiales sinterizados en forma de pastillas como paso previo de escalamiento industrial", 5to Taller de Física de la Materia Condensada y Molecular, Enero de 2012, Facultad de Ciencias, Cuernavaca, Universidad Autónoma del Estadio de Morelos, México.

5. A. Fairbrother, E. García-Hemme, V. Izquierdo-Roca, X. Fontané, A. Pulgarín-Agudelo, D. Sylla, L. Calvo-Barrio, **M. Espindola-Rodriguez,** O. Vigil-Galán, A. Pérez-Rodríguez, E. Saucedo. *"Development of a new selective hydrochloric acid based etching for the improvement of the conversion efficiency of Zn-rich Cu2ZnSnS4 solar cells".* Oral, E-MRS Spring Meeting, May 2012, Strasburg, France.

6. A. Fairbrother, E. Saucedo, X. Fontané, V. Izquierdo, **M. Espindola-Rodriguez,** A. Perez-Rodríguez, J.R. Morante. *"$Cu_2ZnSn(S_ySe_{1-y})_4$ based solar cells via a two-step process using various annealing atmospheres".* Oral, 27th European Photovoltaic Specialist Conference EUPVSEC, September 2012, Frankfurt, Germany.

7. E. Saucedo, V. Izquierdo-Roca, X. Fontané, A. Fairbrother, **M. Espindola-Rodriguez,** S. López, D. Sylla, M. Placidi, A. Pérez-Rodríguez. *"Towards cost-effective processes and earth abundant materials for next generation thin films photovoltaic technologies".* Oral Invited, 6th International Conference on Materials Science and Condensed Matter Physics, September 2012, Chisinau, Republic of Moldova.

8. E. Saucedo, A. Fairbrother, X. Fontané, **M. Espindola-Rodriguez,** V. Izquierdo-Roca, A. Pérez-Rodríguez. *"Development of sustainable PV technologies based on*

earth abundant chalcogenides: challenges and perspectives". Oral Invited, New Energy Forum-2012 (NEF-2012), October 2012, Guangzhou, China.

9. S. López-Mariño, M. Placidi, V. Izquierdo-Roca, X. Fontané, A. Pérez-Tomás, J. Llobet, A. Fairbrother, **M. Espindola-Rodriguez,** F. Pulgarín, D. Sylla, E. Saucedo, A. Pérez-Rodríguez. *"Role of an interfacial ZnO layer between the Mo back contact and the absorber layer on the characteristics of $Cu_2ZnSnSe_4$ based solar cells".* Oral, 3rd European Kesterite Workshop, November 2012, Luxemburg, Luxemburg.

10. S. López-Mariño, M. Placidi, A. Pérez-Tomás, J. Llobet, V. Izquierdo-Roca, X. Fontané, A. Fairbrother **M. Espindola-Rodriguez,** D. Sylla, A. Pérez-Rodríguez, E. Saucedo. *"Improvement of $Cu_2ZnSnSe_4$ based solar cells back contact with an interficial ZnO nanolayer: impact on devices efficiency".* Oral, MRS Spring Meeting, April 2013, San Francisco, USA.

11. S. López-Marino, A. Fairbrother, **M. Espindola-Rodriguez,** X. Fontané, M. Placidi, J. López-García, V. Izquierdo-Roca, A. Pérez-Rodríguez, E. Saucedo. *"New kesterite PVD based technologies: development of a two stage process".* Oral EUROMAT September 2013, Seville, Spain.

12. Y. Sánchez, M. Neuschitzer, M. Dimitrievska, **M. Espindola-Rodriguez,** J. López-García, V. Izquierdo-Roca, O. Vigil-Galán, E. Saucedo. *"High VOC $Cu_2ZnSnS_e4/CdS:Cu$ based solar cell: evidences of a Metal-Insulator-Semiconductor (MIS) type hetero-junction".* Oral, 40th IEEE Photovoltaic Specialists conference, June 2014, Denver, Colorado (USA).

13. H. Xie, Y. Sánchez, S. López-Marino, **M. Espindola-Rodriguez,** J. López-García, A. Fairbrother, A. Pérez-Rodríguez, E. Saucedo. "Impact of Sn(S,Se) secondary phases in $Cu_2ZnSn(S,Se)_4$ solar cells: Development of a simple chemical route for their selective removal and absorber surface passivation". Oral, MRS-Spring Meeting, April 2014, San Francisco, USA.

14. S. López-Marino, **M. Espindola-Rodriguez,** Y. Sánchez, M. Neuschitzer, H. Xie, M. Placidi, V. Izquierdo-Roca, E. Saucedo. "The importance of back contact modification in high efficiency $Cu_2ZnSnSe_4$ solar cells: the role of a thin MoO_2 layer". Oral, NEXGEN NANO PV, April 2015, Menorca, Spain.

15. M. Neuschitzer, T. Olar, F. Oliva, Y. Sánchez, S. López-Marino, **M. Espindola-Rodriguez,** M. Placidi, V. Izquierdo-Roca, I. Lauermann, A. Perez-Rodriguez, E. Saucedo. *"The complex surface chemistry of kesterites: Cu/Zn re-ordering after low temperature re-annealing and its role in high performance devices".* Oral, NEXGEN NANO PV, April 2015, Menorca, Spain.

Other poster Contributions

1. **M. Espindola-Rodriguez,** M.L.Albor Aguilera**,** O.Vigil-Galán, C. Mejía García, E. Sánchez-Meza, J.Fandiño, J.Sastré-Hernández and G. Contreras-Puente, "Some physical properties of Te/CdTe thin films deposited by CSVT-HW technique". Poster, XVIII I-MRS, August 2009, Cancun, México.

Other contributions

2. <u>M.L. Albor Aguilera,</u> **M. Espindola-Rodriguez,** I.D. Sandoval González, O. Vigil Galán, C. Mejía García, A. Cruz Orea, *"Propiedades ópticas de películas delgadas de Te/ CdTe depositadas por CSVT".* Poster, XVI Reunión Nacional Academia de Física y Matemáticas, Noviembre 2009 ESFM-IPN, México D.F.,México.

3. <u>M. L. Albor Aguilera,</u> **M. Espindola-Rodriguez,** O. Vigil Galán, M.A. González Trujillo, Y. Masutmuto Kuwahara, *"Propiedades eléctricas, morfológicas y estructrurales de películas delgadas de Te/ CdTe y CdTe:Te",* Poster, XVI Reunión Nacional Academia de Física y Matemáticas, November 2009, ESFM-IPN, México D.F., México.

4. **M. Espindola-Rodriguez,** O. Vigíl-Galán, J. Santoyo-Moralez, M. Tufiño-Velázquez, F. Cruz-Gandarilla and G. Contreras-Puente. *"Propiedades físicas de películas delegadas del compuesto CuxTe formado por deposito de Te y Cu sobre CdTe".* XV Reunión Nacional Académica de Física y Matemáticas, November 2010, ESFM-IPN, México D.F., México.

5. **M. Espindola-Rodriguez,** O.Vigil-Galán, M. Tufiño-Velázquez, F. Cruz-Gandarilla and G. Contreras-Puente. "Physical properties of Cu_xTe films compounds on CdTe films formed by the deposition of Te and Cu". Poster, XIX I-MRS August 2010, Cancún, México.

6. <u>O. Vigil Galán,</u> **M. Espindola-Rodriguez,** A. Arce Plaza, J. Sastré, Hernández, G. Contreras Puente, F. Cruz Gandarilla "Evaluation of Bi_2Te_3 and Sb_2Te_3 layers deposited by CSVT method as back contacts to p-CdTe films". Poster, XIX I-MRS August 2010, Cancún, México.

7. <u>O. Vigil Galán,</u> D. Jiménez Olarte, E. Saucedo, J. Sastré Hernández, **M. Espindola-Rodriguez,** G. Contreras Puente. *"Contact resistance study on Cu2ZnSnS4 used as absorber material in Thin-Films Solar Cells".* Poster, XX I-MRS, August 2011, Cancún, México.

8. <u>A. Fairbrother,</u> E. Saucedo, X. Fontané, V. Izquierdo, D. Sylla, **M. Espindola-Rodriguez,** F.A. Pulgarín, O. Vigil-Galán, A. Pérez-Rodríguez. *"Preparation of 4.8% efficiency Cu2ZnSnSe4 based solar cell by a two step process".* Poster (Nominated Best Poster), IEEE Photovoltaic Specialist Conference, June 2012, Austin, Texas, USA.

9. <u>A. Fairbrother,</u> X. Fontané, V. Izquierdo-Roca, **M. Espindola-Rodriguez,** S. López, M. Placidi, L. Calvo-Barrio, A. Pérez-Rodríguez, E. Saucedo. *"On the formation mechanisms of Zn-rich CZTS films prepared by sulfurization of metallic stacks".* Poster, 3rd European Kesterite Workshop, November 2012, Luxemburg, Luxemburg.

10. S. López-Mariño, M. Placidi, V. Izquierdo-Roca, X. Fontané, A. Pérez-Tomás, J. Llobet, A. Fairbrother, **M. Espindola-Rodriguez,** F. Pulgarín, D. Sylla, <u>E. Saucedo,</u> A. Pérez-Rodríguez. "Preparation of $CuInSe_2$ based solar cells by selenization of electrodeposited Cu-In multilayers: influence of the electrochemical conditions". Poster, MRS Spring Meeting, April 2013, San Francisco, USA.

11. X. Fontané, V. Izquierdo-Roca, <u>A. Fairbrother,</u> **M. Espindola-Rodriguez,** S. López-Marino, M. Placidi, T. Jawhari, E. Saucedo, A. Pérez-Rodríguez. "Selective detection

of secondary phases in Cu2ZnSn(S,Se)4 based absorbers by pre-resonant Raman spectroscopy". Poster, 39th IEEE Photovoltaic Specialists Conference, June 2013, Florida, USA.

12. <u>S. Lopez-Marino,</u> Y. Sánchez, M. Placidi, A. Fairbrother, **M. Espindola-Rodriguez,** X. Fontané, V. Izquierdo-Roca, J. López-García, L. Calvo-Barrio, A. Perez-Rodríguez, E. Saucedo. *"Selective removal of ZnSe in Zn-rich Cu2ZnSnSe4 films: a new oxidizing approach".* Poster, 28th EU PVSEC, October 2013, Paris, France.

13. <u>J. López-García,</u> H. Xie, D. Sylla, X. Fontané, M. Blanes-Guardia, F. Ramos, **M. Espindola-Rodriguez,** S. López-Marino, V. Izquierdo-Roca, E. Saucedo, A. Pérez-Rodriguez. *"Influence of the sulfurization-selenization process on CuIn(S,Se)$_2$ thin film solar cells from screen printing of oxide nanoparticle based inks".* Poster, 28th EU PVSEC, October 2013, Paris, France.

14. <u>S. Lopez-Marino,</u> M. Neuschitzer, Y. Sánchez, A. Fairbrother, **M. Espindola-Rodriguez,** J. López-García, M. Placidi, L. Calvo-Barrio, A. Pérez-Rodríguez, E. Saucedo. *"Extension of Cu$_2$ZnSnSe$_4$ based solar cells to low weight stainless steel substrates".* Poster, 4th European Workshop on Kesterites, November 2013, Berlin, Germany.

15. <u>S. Lopez-Marino,</u> M. Neuschitzer, Y. Sánchez, A. Fairbrother, **M. Espindola-Rodriguez,** J. López-García, M. Placidi, L. Calvo-Barrio, A. Pérez-Rodríguez, E. Saucedo. *"Development of Cu$_2$ZnSnSe$_4$ based solar cells onto low weight stainless steel substrates".* Poster, MRS-Spring Meeting, April 2014, San Francisco, USA.

16. **<u>M. Espindola-Rodriguez,</u>** M. Placidi, Y. Sánchez, D. Sylla, S. López-Merino, M. Neuschitzer,O. Vigil-Galán, A. Pérez-Rodríguez, E. Saucedo. *"Transparent conducting back contacts for bifacial Cu$_2$ZnSnSe$_4$ solar cells".* Poster, NEXGEN NANO PV, April 2015, Menorca, Spain.

17. **<u>M. Espindola-Rodriguez,</u>** S. López-Mariño, A. Carreté, C. Insignares-Cuello, Y. Sánchez, M. Placidi, E. Saucedo, A. Pérez-Rodríguez, V. Izquierdo-Roca, S. Jaime-Ferrer, P.-P. Grand, C. Broussillou. *"Raman scattering based strategies for process monitoring in thin film chalcogenide technologies: Example of application in CIGS industrial electrodeposition based processes".* Poster, NEXGEN NANO PV, April 2015, Menorca, Spain.

18. <u>Y. Sánchez,</u> **M. Espindola-Rodriguez,** S. López-Marino, M. Neuschitzer, S. Giraldo, M. Dimitrievska, V. Izquierdo-Roca, F.A. Pulgarín-Agudelo, O. Vigil-Galán, E. Saucedo. "Ultra-thin CdS for highly performing chalcogenides thin film based solar cells". Poster, NEXGEN NANO PV, April 2015, Menorca, Spain.

19. <u>S. Giraldo,</u> C.M. Ruiz, **M. Espindola-Rodriguez,** Y. Sánchez, M. Placidi, D. Barakel, L. Escoubas, A. Pérez-Rodríguez, E. Saucedo. "Optical and electrical properties of In-doped Cu$_2$ZnSnSe$_4$". Poster, NEXGEN NANO PV, April 2015, Menorca, Spain.

20. <u>H. Xie,</u> Y. Sánchez, M. Dimitrievska, X. Fontané, S. López-Marino, M. Neuschitzer, **M. Espindola-Rodriguez,** V. Izquierdo-Roca, A. Pérez-Rodríguez, E. Saucedo. *"Preparation of high efficiency Cu$_2$ZnSn(S$_{1-y}$Se$_y$)$_4$ solar cells based on a single-step sulfo-selenization process".* Poster, NEXGEN NANO PV, April 2015, Menorca, Spain.

21. **M. Espindola-Rodriguez,** M. Placidi, Y. Sánchez, <u>S. López-Marino,</u> D. Sylla, M. Neuschitzer, V. Izquierdo-Roca, O. Vigil-Galán, A. Pérez-Rodríguez, E. Saucedo. "B*ifacial Cu2ZnSnSe4 Solar Cells".* Poster, E-MRS Spring Meeting, May 2015, Lille, France.

22. <u>S. Giraldo,</u> C.M. Ruiz, **M. Espindola-Rodriguez,** Y. Sánchez, M. Placidi, D. Barakel, L. Escoubas, A. Pérez-Rodríguez, E. Saucedo. *"Effect of In-doping on Cu$_2$ZnSnSe$_4$ based solar cells properties".* Poster, E-MRS Spring Meeting, May 2015, Lille, France.

23. <u>S. López-Marino,</u> Y. Sánchez, **M. Espindola-Rodriguez,** M. Neuschitzer, H. Xie, M. Placidi, M. Dimitrievska, V. Izquierdo-Roca, L. Fourdrinier, and E. Saucedo. "Alkali doping strategies for flexible and light-weight CZTSe solar cells". Poster, E-MRS Spring Meeting, May 2015, Lille, France.

24. **M. Espindola-Rodriguez,** Y. Sánchez, S. López-Marino, V. Izquierdo-Roca, D. Sylla, M. Neuschitzer, O. Vigil-Galán, <u>E. Saucedo,</u> M. Placidi. *"Efficient Bifacial Cu2ZnSnSe4 Solar Cells".* Poster, 42th IEEE Photovoltaic Specialists Conference, June 2015, New Orleans, LA (USA).

25. <u>M. Placidi,</u> **M. Espindola-Rodriguez,,** S. Lopez-Marino, Y. Sanchez, M. Neuschitzer, V. Izquierdo Roca, X. Fontané, X. Alcobé, A. Pérez-Rodríguez, E. Saucedo. *"Cu$_2$ZnSnSe$_4$ based solar cells prepared at high temperatures on Si/SiO$_2$ sodium-free substrate".* Poster, 42th IEEE Photovoltaic Specialists Conference, June 2015, New Orleans, LA (USA).

26. **M. Espindola-Rodriguez,** Y. Sanchez, <u>S. López-Marino,</u> H. Xie, D. Sylla, V. Izquierdo-Roca, O. Vigil-Galán, P. Pistor, E. Saucedo, M. Placidi. *"Cu$_2$ZnSn(S,Se)$_4$ absorbers onto transparent conducting back contacts for bifacial solar cells concepts".* Poster, 31st EU PVSEC, September 2015, Hamburg, Germany.

27. <u>M. Placidi,</u> **M. Espindola-Rodriguez,,** S. Lopez-Marino, Y. Sanchez, M. Neuschitzer, V. Izquierdo Roca, X. Fontané, X. Alcobé, A. Pérez-Rodríguez, E. Saucedo. *"Cu$_2$ZnSnSe$_4$ based solar cells prepared at high temperatures on Si/SiO$_2$ sodium-free substrate".* Poster, 31st EU PVSEC, September 2015, Hamburg, Germany.

28. <u>S. López-Marino,</u> Y. Sánchez, **M. Espindola-Rodriguez,** M. Neuschitzer, H. Xie1, M. Placidi, M. Dimitrievska, S. Giraldo, V. Izquierdo-Roca, L. Fourdrinier, E. Saucedo. *"A comparison between alkali doping methods forCu$_2$ZnSnSe$_4$ solar cells fabricated onto flexible steel substrates".* Poster, 31st EU PVSEC, September 2015, Hamburg, Germany.

Other published articles

1. W. Steffen, **M. Espíndola,** S. Martínez, N. Koning, *"The 3D velocity structure of the planetary nebula NGC 7009",* Revista mexicana de astronomía y astrofísica, 45 (2009) 143-154.

2. A. Fairbrother, E. Saucedo, X. Fontane, V. Izquierdo-Roca, D. Sylla, **M. Espindola-Rodriguez,** F.A. Pulgarin-Agudelo, O. Vigil-Galan, A. Perez-Rodriguez, *"Preparation*

of 4.8% efficiency Cu2ZnSnSe4based solar cell by a two step process", Photovoltaic Specialists Conference (PVSC), 2012 38th IEEE, 2012, pp. 002679-002684.

3. A. Fairbrother, X. Fontané, V. Izquierdo-Roca, **M. Espindola-Rodriguez,** S. López-Marino, M. Placidi, L. Calvo-Barrio, A. Pérez-Rodríguez, E. Saucedo, *"On the formation mechanisms of Zn-rich Cu2ZnSnS4 films prepared by sulfurization of metallic stacks",* Solar Energy Materials and Solar Cells, 112 (2013) 97-105.

4. A. Fairbrother, X. Fontané, V. Izquierdo-Roca, **M. Espindola-Rodriguez,** S. López-Marino, M. Placidi, J. López-García, A. Pérez-Rodríguez, E. Saucedo, "Single-Step Sulfo-Selenization Method to Synthesize $Cu_2ZnSn(S_ySe_{1-y})_4$ Absorbers from Metallic Stack Precursors", ChemPhysChem, 14 (2013) 1836-1843.

5. X. Fontane, V. Izquierdo-Roca, A. Fairbrother, **M. Espindola-Rodriguez,** S. Lopez-Marino, M. Placidi, T. Jawhari, E. Saucedo, A. Perez-Rodriguez, *"Selective detection of secondary phases in $Cu_2ZnSn(S,Se)_4$ based absorbers by pre-resonant Raman spectroscopy",* Photovoltaic Specialists Conference (PVSC), 2013 IEEE 39th, 2013, pp. 2581-2584.

6. S. Lopez-Marino, M. Placidi, A. Perez-Tomas, J. Llobet, V. Izquierdo-Roca, X. Fontane, A. Fairbrother, **M. Espindola-Rodriguez,** D. Sylla, A. Perez-Rodriguez, E. Saucedo, *"Inhibiting the absorber/Mo-back contact decomposition reaction in Cu2ZnSnSe4 solar cells: the role of a ZnO intermediate nanolayer",* Journal of Materials Chemistry A, (2013) 8338-8343.

7. S. López-Marino, Y. Sánchez, M. Placidi, A. Fairbrother, **M. Espindola-Rodriguez,** X. Fontané, V. Izquierdo-Roca, J. López-García, L. Calvo-Barrio, A. Pérez-Rodríguez, E. Saucedo, *"ZnSe Etching of Zn-Rich $Cu_2ZnSnSe_4$: An Oxidation Route for Improved Solar-Cell Efficiency",* Chemistry – A European Journal, 19 (2013) 14814-14822.

8. A. Fairbrother, X. Fontané, V. Izquierdo-Roca, M. Placidi, D. Sylla, **M. Espindola-Rodriguez,** S. López-Mariño, F.A. Pulgarín, O. Vigil-Galán, A. Pérez-Rodríguez, E. Saucedo, *"Secondary phase formation in Zn-rich $Cu_2ZnSnSe_4$-based solar cells annealed in low pressure and temperature conditions",* Progress in Photovoltaics: Research and Applications, 22 (2014) 479-487.

9. S. López-Marino, M. Neuschitzer, Y. Sánchez, A. Fairbrother, **M. Espindola-Rodriguez,** J. López-García, M. Placidi, L. Calvo-Barrio, A. Pérez-Rodríguez, E. Saucedo, *"Earth-abundant absorber based solar cells onto low weight stainless steel substrate",* Solar Energy Materials and Solar Cells, 130 (2014) 347-353.

10. Y. Sanchez, M. Neuschitzer, M. Dimitrievska, **M. Espindola-Rodriguez,** J. Lopez-Garcia, V. Izquierdo-Roca, O. Vigil-Galan, E. Saucedo, *"High VOC Cu2ZnSnSe4/CdS:Cu based solar cell: Evidences of a metal-insulator-semiconductor (MIS) type hetero-junction",* Photovoltaic Specialist Conference (PVSC), 2014 IEEE 40th, 2014, pp. 0417-0420.

11. J. López-García, M. Placidi, X. Fontané, V. Izquierdo-Roca, **M. Espindola**, E. Saucedo, C. Guillén, J. Herrero, A. Pérez-Rodriguez, *"$CuIn_{1-x}Al_xSe_2$ thin film solar cells with depth gradient composition prepared by selenization of evaporated metallic precursors",* Solar Energy Materials and Solar Cells, 132 (2015) 245-251.

12. J. López-García, H. Xie, V. Izquierdo-Roca, D. Sylla, X. Fontané, M. Blanes-Guardia, F. Ramos, **M. Espindola-Rodriguez,** S. López-Marino, E. Saucedo, A. Pérez-Rodriguez, *"Synthesis of CuIn(S,Se)$_2$ quaternary alloys by screen printing and selenization-sulfurization sequential steps: Development of composition graded absorbers for low cost photovoltaic devices",* Materials Chemistry and Physics, (2015).

References

1. Renewables Global Status Report 2014 (Renewable Energy Policy Network for the 21st Century, Paris).

2. Shockley, W. & Queisser, H.J. Detailed Balance Limit of Efficiency of p-n Junction Solar Cells. *Journal of Applied Physics* **32**, 510 (1961).

3. Green, M.A., Emery, K., Hishikawa, Y., Warta, W. & Dunlop, E.D. Solar cell efficiency tables (Version 38). *Progress in Photovoltaics: Research and Applications* **19**, 565-572 (2011).

4. Todorov, T.K., Reuter, K.B. & Mitzi, D.B. High-Efficiency Solar Cell with Earth-Abundant Liquid-Processed Absorber. *Advanced Materials* **22**, E156-E159 (2010).

5. Green, M.A., Emery, K., Hishikawa, Y., Warta, W. & Dunlop, E.D. Solar cell efficiency tables (version 40). *Progress in Photovoltaics: Research and Applications* **20**, 606-614 (2012).

6. Green, M.A., Emery, K., Hishikawa, Y., Warta, W. & Dunlop, E.D. Solar cell efficiency tables (version 41). *Progress in Photovoltaics: Research and Applications* **21**, 1-11 (2013).

7. Shin, B. et al. Thin film solar cell with 8.4% power conversion efficiency using an earth-abundant Cu2ZnSnS4 absorber. *Progress in Photovoltaics: Research and Applications* **21**, 72-76 (2013).

8. Green, M.A., Emery, K., Hishikawa, Y., Warta, W. & Dunlop, E.D. Solar cell efficiency tables (Version 45). *Progress in Photovoltaics: Research and Applications* **23**, 1-9 (2015).

9. Wang, W. et al. Device Characteristics of CZTSSe Thin-Film Solar Cells with 12.6% Efficiency. *Advanced Energy Materials* **4** (2014).

10. Schorr, S. The crystal structure of kesterite type compounds: A neutron and X-ray diffraction study. *Solar Energy Materials and Solar Cells* **95**, 1482-1488 (2011).

11. Unold, T. & Schock, H.W. Nonconventional (Non-Silicon-Based) Photovoltaic Materials. *Annual Review of Materials Research* **41**, 297-321 (2011).

12. Mitzi, D.B., Gunawan, O., Todorov, T.K., Wang, K. & Guha, S. The path towards a high-performance solution-processed kesterite solar cell. *Solar Energy Materials and Solar Cells* **95**, 1421-1436.

13. Abermann, S. Non-vacuum processed next generation thin film photovoltaics: Towards marketable efficiency and production of CZTS based solar cells. *Solar Energy* **94**, 37-70 (2013).

14. Siebentritt, S. & Schorr, S. Kesterites—a challenging material for solar cells. *Progress in Photovoltaics: Research and Applications* **20**, 512-519 (2012).

15. Kodigala, S.R. in Thin Film Solar Cells from Earth Abundant Materials (ed. Kodigala, S.R.) 1-13 (Elsevier, Oxford, 2014).

16. Metzger, W.K., Repins, I.L. & Contreras, M.A. Long lifetimes in high-efficiency Cu(In,Ga)Se2 solar cells. *Applied Physics Letters* **93**, 022110 (2008).

17. Repins, I. et al. Co-evaporated Cu2ZnSnSe4 films and devices. *Solar Energy Materials and Solar Cells* **101**, 154-159 (2012).

18. Schwarz, T. et al. Atom probe study of Cu2ZnSnSe4 thin-films prepared by co-evaporation and post-deposition annealing. *Applied Physics Letters* **102**, 042101 (2013).

19. Fairbrother, A. et al. Development of a Selective Chemical Etch To Improve the Conversion Efficiency of Zn-Rich Cu2ZnSnS4 Solar Cells. *Journal of the American Chemical Society* **134**, 8018-8021 (2012).

20. López-Marino, S. et al. ZnSe Etching of Zn-Rich Cu2ZnSnSe4: An Oxidation Route for Improved Solar-Cell Efficiency. *Chemistry – A European Journal* **19**, 14814-14822 (2013).

21. Chen, S., Walsh, A., Gong, X.-G. & Wei, S.-H. Classification of Lattice Defects in the Kesterite Cu2ZnSnS4 and Cu2ZnSnSe4 Earth-Abundant Solar Cell Absorbers. *Advanced Materials* **25**, 1522-1539 (2013).

22. Siebentritt, S. Why are kesterite solar cells not 20% efficient? *Thin Solid Films* **535**, 1-4 (2013).

23. Tajima, S. et al. Atom-probe tomographic study of interfaces of Cu2ZnSnS4 photovoltaic cells. *Applied Physics Letters* **105**, 093901 (2014).

24. Neuschitzer, M. et al. Optimization of CdS buffer layer for high-performance Cu2ZnSnSe4solar cells and the effects of light soaking: elimination of crossover and red kink. *Progress in Photovoltaics: Research and Applications*, n/a-n/a (2015).

25. Katagiri, H. et al. Development of CZTS-based thin film solar cells. *Thin Solid Films* **517**, 2455-2460 (2009).

26. Scragg, J.J. et al. A Detrimental Reaction at the Molybdenum Back Contact in Cu2ZnSn(S,Se)4 Thin-Film Solar Cells. *Journal of the American Chemical Society* **134**, 19330-19333 (2012).

27. Wang, K. et al. Structural and elemental characterization of high efficiency Cu2ZnSnS4 solar cells. *Applied Physics Letters* **98**, 051912 (2011).

28. Shin, B., Zhu, Y., Bojarczuk, N.A., Jay Chey, S. & Guha, S. Control of an interfacial MoSe2 layer in Cu2ZnSnSe4 thin film solar cells: 8.9% power conversion efficiency with a TiN diffusion barrier. *Applied Physics Letters* **101**, 053903 (2012).

29. Wang, K. et al. Thermally evaporated Cu2ZnSnS4 solar cells. *Applied Physics Letters* **97**, 143508 (2010).

30. Todorov, T.K. et al. Beyond 11% Efficiency: Characteristics of State-of-the-Art Cu2ZnSn(S,Se)4 Solar Cells. *Advanced Energy Materials* **3**, 34-38 (2013).

31. Ennaoui, A. et al. Cu2ZnSnS4 thin film solar cells from electroplated precursors: Novel low-cost perspective. *Thin Solid Films* **517**, 2511-2514 (2009).

32. Liu, F. et al. Enhancing the Cu2ZnSnS4 solar cell efficiency by back contact modification: Inserting a thin TiB2 intermediate layer at Cu2ZnSnS4/Mo interface. *Applied Physics Letters* **104**, 051105 (2014).

33. Altamura, G. et al. Alternative back contacts in kesterite Cu2ZnSn(S1-xSex)4 thin film solar cells. *Journal of Renewable and Sustainable Energy* **6** (2014).

34. Lopez-Marino, S. et al. Inhibiting the absorber/Mo-back contact decomposition reaction in Cu2ZnSnSe4 solar cells: the role of a ZnO intermediate nanolayer. *Journal of Materials Chemistry A*, 8338-8343 (2013).

35. Todorov, T. et al. Progress towards marketable earth-abundant chalcogenide solar cells. *Thin Solid Films* **519**, 7378-7381 (2011).

36.	Barkhouse, D.A.R., Gunawan, O., Gokmen, T., Todorov, T.K. & Mitzi, D.B. Device characteristics of a 10.1% hydrazine-processed Cu2ZnSn(Se,S)4 solar cell. *Progress in Photovoltaics: Research and Applications* **20**, 6-11 (2012).

37.	Siebentritt, S. What limits the efficiency of chalcopyrite solar cells? *Solar Energy Materials and Solar Cells* **95**, 1471-1476 (2011).

38.	Price, K.J., Grecu, D., Shvydka, D. & Compaan, A.D. in Photovoltaic Specialists Conference, 2000. Conference Record of the Twenty-Eighth IEEE 658-661 (2000).

39.	Chirilă, A. et al. Potassium-induced surface modification of Cu(In,Ga)Se2 thin films for high-efficiency solar cells. *Nat Mater* **12**, 1107-1111 (2013).

40.	Collord, A.D., Xin, H. & Hillhouse, H.W. Combinatorial Exploration of the Effects of Intrinsic and Extrinsic Defects. *Photovoltaics, IEEE Journal of* **5**, 288-298 (2015).

41.	Guo, Q. et al. Fabrication of 7.2% Efficient CZTSSe Solar Cells Using CZTS Nanocrystals. *Journal of the American Chemical Society* **132**, 17384-17386 (2010).

42.	Ki, W. & Hillhouse, H.W. Earth-Abundant Element Photovoltaics Directly from Soluble Precursors with High Yield Using a Non-Toxic Solvent. *Advanced Energy Materials* **1**, 732-735 (2011).

43.	Kim, J. et al. High Efficiency Cu2ZnSn(S,Se)4 Solar Cells by Applying a Double In2S3/CdS Emitter. *Advanced Materials* **26**, 7427-7431 (2014).

44.	Kato, T., Sakai, N. & Sugimoto, H. in Photovoltaic Specialist Conference (PVSC), 2014 IEEE 40th 0844-0846 (2014).

45.	Werner, M. et al. Enhanced carrier collection from CdS passivated grains in solution processed Cu2ZnSn(S,Se)4 solar cells. *ACS Applied Materials & Interfaces* (2015).

46.	Schnabel, T., Abzieher, T., Friedlmeier, T.M. & Ahlswede, E. Solution-Based Preparation of CZTSSe for Solar Cells-Comparison of SnSe2 and Elemental Se as Chalcogen Source. *Photovoltaics, IEEE Journal of* **5**, 670-675 (2015).

47.	Miskin, C.K. et al. 9.0% efficient Cu2ZnSn(S,Se)4 solar cells from selenized nanoparticle inks. *Progress in Photovoltaics: Research and Applications* **23**, 654-659 (2015).

48.	Lee, Y.S. et al. Cu2ZnSnSe4 Thin-Film Solar Cells by Thermal Co-evaporation with 11.6% Efficiency and Improved Minority Carrier Diffusion Length. *Advanced Energy Materials* (2014).

49.	Oueslati, S. et al. Physical and electrical characterization of high-performance Cu2ZnSnSe4 based thin film solar cells. *Thin Solid Films* **582**, 224-228 (2015).

50.	*To be published*.

51.	Choi, S.G. et al. Temperature dependent band-gap energy for Cu2ZnSnSe4: A spectroscopic ellipsometric study. *Solar Energy Materials and Solar Cells* **130**, 375-379 (2014).

52.	Hiroi, H., Sakai, N., Kato, T. & Sugimoto, H. in Photovoltaic Specialists Conference (PVSC), 2013 IEEE 39th 0863-0866 (2013).

53.	Larramona, G. et al. Efficient Cu2ZnSnS4 solar cells spray coated from a hydro-alcoholic colloid synthesized by instantaneous reaction. *RSC Advances* **4**, 14655-14662 (2014).

54.	Sutter-Fella, C.M. et al. Sodium Assisted Sintering of Chalcogenides and Its Application to Solution Processed Cu2ZnSn(S,Se)4 Thin Film Solar Cells. *Chemistry of Materials* **26**, 1420-1425 (2014).

55. Rajeshmon, V.G., Poornima, N., Sudha Kartha, C. & Vijayakumar, K.P. Modification of the optoelectronic properties of sprayed In2S3 thin films by indium diffusion for application as buffer layer in CZTS based solar cell. *Journal of Alloys and Compounds* **553**, 239-244 (2013).

56. Vigil-Galán, O. et al. Electrical properties of sprayed Cu2ZnSnS4 thin films and its relation with secondary phase formation and solar cell performance. *Solar Energy Materials and Solar Cells* **132**, 557-562 (2015).

57. Espindola-Rodriguez, M. et al. Pneumatically sprayed Cu_2ZnSnS_4 films under Ar and Ar–H_2 atmosphere. *Journal of Physics D: Applied Physics* **47**, 245101 (2014).

58. Vigil-Galán, O. et al. Route towards low cost-high efficiency second generation solar cells: current status and perspectives. *Journal of Materials Science: Materials in Electronics*, 1-12 (2014).

59. Vigil-Galán, O. et al. Toward a high CZTS solar cell efficiency processed by spray pyrolysis method. *Journal of Renewable and Sustainable Energy* **5** (2013).

60. Tanaka, K., Kurokawa, M., Moriya, K. & Uchiki, H. Surface morphology improvement of three-dimensional solar cell with CuZnSnS absorber. *Journal of Alloys and Compounds* **571**, 98-102 (2013).

61. Espindola-Rodriguez, M. et al. Compositional optimization of photovoltaic grade Cu2ZnSnS4 films grown by pneumatic spray pyrolysis. *Thin Solid Films* **535**, 67-72 (2013).

62. Agrawal, R. & Fidkowski, Z.T. Thermodynamically Efficient Systems for Ternary Distillation. *Industrial & Engineering Chemistry Research* **38**, 2065-2074 (1999).

63. Agrawal, R. & Fidkowski, Z.T. Are Thermally Coupled Distillation Columns Always Thermodynamically More Efficient for Ternary Distillations? *Industrial & Engineering Chemistry Research* **37**, 3444-3454 (1998).

64. Hurt, M.R. et al. On-Line Mass Spectrometric Methods for the Determination of the Primary Products of Fast Pyrolysis of Carbohydrates and for Their Gas-Phase Manipulation. *Analytical Chemistry* **85**, 10927-10934 (2013).

65. Bucherl, C.N., Oleson, K.R. & Hillhouse, H.W. Thin film solar cells from sintered nanocrystals. *Current Opinion in Chemical Engineering* **2**, 168-177 (2013).

66. Guo, Q., Ford, G.M., Agrawal, R. & Hillhouse, H.W. Ink formulation and low-temperature incorporation of sodium to yield 12% efficient Cu(In,Ga)(S,Se)2 solar cells from sulfide nanocrystal inks. *Progress in Photovoltaics: Research and Applications* **21**, 64-71 (2013).

67. Guo, Q. et al. Development of CuInSe2 Nanocrystal and Nanoring Inks for Low-Cost Solar Cells. *Nano Letters* **8**, 2982-2987 (2008).

68. Kar, M., Agrawal, R. & Hillhouse, H.W. Formation Pathway of CuInSe2 Nanocrystals for Solar Cells. *Journal of the American Chemical Society* **133**, 17239-17247 (2011).

69. Yang, W.-C., Miskin, C.K., Carter, N.J., Agrawal, R. & Stach, E.A. Compositional Inhomogeneity of Multinary Semiconductor Nanoparticles: A Case Study of Cu2ZnSnS4. *Chemistry of Materials* **26**, 6955-6962 (2014).

70. Yang, W.-C. et al. Kesterite Cu2ZnSn(S,Se)4 Absorbers Converted from Metastable, Wurtzite-Derived Cu2ZnSnS4 Nanoparticles. *Chemistry of Materials* **26**, 3530-3534 (2014).

71. Salvador, M. et al. Nanoscale Surface Potential Variation Correlates with Local S/Se Ratio in Solution-Processed CZTSSe Solar Cells. *Nano Letters* **14**, 6926-6930 (2014).

72. Larramona, G. et al. 8.6% Efficient CZTSSe Solar Cells Sprayed from Water–Ethanol CZTS Colloidal Solutions. *The Journal of Physical Chemistry Letters* **5**, 3763-3767 (2014).

73. Kim, S. & Kim, J. Effect of selenization on sprayed Cu2ZnSnSe4 thin film solar cell. *Thin Solid Films* **547**, 178-180 (2013).

74. Espindola-Rodriguez, M. et al. Cu₂ZnSnS₄ absorber layers deposited by spray pyrolysis for advanced photovoltaic technology. *Physica Status Solidi (a)* (2014).

75. M. Werner, C.M.F., C. Gretener, Y.E. Romanyuk, A.N. Tiwari. CZTS Solar Cell Absorbers Deposited by Sequential Ultrasonic Spray Pyrolysis. *28th European Photovoltaic Solar Energy Conference and Exhibition*, 2455 - 2458.

76. Krebs, F.C. Fabrication and processing of polymer solar cells: A review of printing and coating techniques. *Solar Energy Materials and Solar Cells* **93**, 394-412 (2009).

77. Patil, P.S. Versatility of chemical spray pyrolysis technique. *Materials Chemistry and Physics* **59**, 185-198 (1999).

78. Chamberlin, R.R. & Skarman, J.S. Chemically sprayed thin film photovoltaic converters. *Solid-State Electronics* **9**, 819-823 (1966).

79. Nakayama, N. & Ito, K. Sprayed films of stannite Cu2ZnSnS4. *Applied Surface Science* **92**, 171-175 (1996).

80. Vigil-Galán, O. et al. Secondary phases dependence on composition ratio in sprayed Cu2ZnSnS4 thin films and its impact on the high power conversion efficiency. *Solar Energy Materials and Solar Cells* **117**, 246-250 (2013).

81. Daranfed, W., Aida, M.S., Attaf, N., Bougdira, J. & Rinnert, H. Cu2ZnSnS4 thin films deposition by ultrasonic spray pyrolysis. *Journal of Alloys and Compounds* **542**, 22-27 (2012).

82. Rothwarf, A. & Böer, K.W. Direct conversion of solar energy through photovoltaic cells. *Progress in Solid State Chemistry* **10, Part 2**, 71-102 (1975).

83. Tomar, M.S. & Garcia, F.J. Spray pyrolysis in solar cells and gas sensors. *Progress in Crystal Growth and Characterization* **4**, 221-248 (1981).

84. Usha Rajalakshmi, P., Oommen, R., Sanjeeviraja, C. & Ganesan, V. Effect of composition on structural and optical characteristics of nebulised spray pyrolysed (Bi1−xSbx)2S3 thin films. *Superlattices and Microstructures* **57**, 158-165 (2013).

85. Siefert, W. Corona spray pyrolysis: A new coating technique with an extremely enhanced deposition efficiency. *Thin Solid Films* **120**, 267-274 (1984).

86. Liu, J.P. et al. Fabrication and characterization of kesterite Cu2ZnSnS4thin films deposited by electrostatic spray assisted vapour deposition method. *physica status solidi (a)* **212**, 135-139 (2015).

87. Joshi, B.N., Yoon, H., Na, S.-H., Choi, J.-Y. & Yoon, S.S. Enhanced photocatalytic performance of graphene–ZnO nanoplatelet composite thin films prepared by electrostatic spray deposition. *Ceramics International* **40**, 3647-3654 (2014).

88. Denayer, J. et al. Improved coloration contrast and electrochromic efficiency of tungsten oxide films thanks to a surfactant-assisted ultrasonic spray pyrolysis process. *Solar Energy Materials and Solar Cells* **130**, 623-628 (2014).

89. García-Hipólito, M., Martínez, R., Alvarez-Fregoso, O., Martínez, E. & Falcony, C. Cathodoluminescent and photoluminescent properties of terbium doped ZrO2

films prepared by pneumatic spray pyrolysis technique. *Journal of Luminescence* **93**, 9-15 (2001).

90. Perednis, D. & Gauckler, L. Thin Film Deposition Using Spray Pyrolysis. *Journal of Electroceramics* **14**, 103-111 (2005).

91. Filipovic, L. et al. Methods of simulating thin film deposition using spray pyrolysis techniques. *Microelectronic Engineering* **117**, 57-66 (2014).

92. WordReference. in Random House Learner's Dictionary of American English (2015).

93. Viguié, J.C. & Spitz, J. Chemical Vapor Deposition at Low Temperatures. *Journal of The Electrochemical Society* **122**, 585-588 (1975).

94. Chamberlin, R.R. & Skarman, J.S. Chemical Spray Deposition Process for Inorganic Films. *Journal of The Electrochemical Society* **113**, 86-89 (1966).

95. Kishore Kumar, Y.B., Suresh Babu, G., Uday Bhaskar, P. & Sundara Raja, V. Preparation and characterization of spray-deposited Cu2ZnSnS4 thin films. *Solar Energy Materials and Solar Cells* **93**, 1230-1237 (2009).

96. Madarász, J., Bombicz, P., Okuya, M. & Kaneko, S. Thermal decomposition of thiourea complexes of Cu(I), Zn(II), and Sn(II) chlorides as precursors for the spray pyrolysis deposition of sulfide thin films. *Solid State Ionics* **141–142**, 439-446 (2001).

97. Patel, M., Mukhopadhyay, I. & Ray, A. Structural, optical and electrical properties of spray-deposited CZTS thin films under a non-equilibrium growth condition. *Journal of Physics D: Applied Physics* **45**, 445103 (2012).

98. Mitzi, D.B. Solution processing of inorganic materials (John Wiley & Sons, Inc., Hoboken., New Jersey, 2009).

99. Ho, J.C.W. et al. Spray Pyrolysis of CuIn(S,Se)2 Solar Cells with 5.9% Efficiency: A Method to Prevent Mo Oxidation in Ambient Atmosphere. *ACS Applied Materials & Interfaces* **6**, 6638-6643 (2014).

100. Hironori, K. et al. Enhanced Conversion Efficiencies of Cu 2 ZnSnS 4 -Based Thin Film Solar Cells by Using Preferential Etching Technique. *Applied Physics Express* **1**, 041201 (2008).

101. Kodigala, S.R. Thin Film Solar Cells from Earth Abundant Materials (Elsevier, 2014).

102. Brimblecombe, P. Air, Composition and Chemistry. *Cambridge environmental chemistry series-6* **2nd Ed.** (1996).

103. Kumar, Y.B.K., Babu, G.S., Bhaskar, P.U. & Raja, V.S. Effect of starting-solution pH on the growth of Cu2ZnSnS4 thin films deposited by spray pyrolysis. *physica status solidi (a)* **206**, 1525-1530 (2009).

104. Redinger, A., Berg, D.M., Dale, P.J. & Siebentritt, S. The Consequences of Kesterite Equilibria for Efficient Solar Cells. *Journal of the American Chemical Society* **133**, 3320-3323 (2011).

105. Chen, S., Yang, J.-H., Gong, X.G., Walsh, A. & Wei, S.-H. Intrinsic point defects and complexes in the quaternary kesterite semiconductor CZTS. *Physical Review B* **81**, 245204 (2010).

106. Fontané, X. et al. In-depth resolved Raman scattering analysis for the identification of secondary phases: Characterization of Cu2ZnSnS4 layers for solar cell applications. *Applied Physics Letters* **98**, 181905 (2011).

107. Fontané, X. et al. Vibrational properties of stannite and kesterite type compounds: Raman scattering analysis of Cu2(Fe,Zn)SnS4. *Journal of Alloys and Compounds* **539**, 190-194 (2012).

108. Platzer-Björkman, C., Scragg, J., Flammersberger, H., Kubart, T. & Edoff, M. Influence of precursor sulfur content on film formation and compositional changes in Cu2ZnSnS4 films and solar cells. *Solar Energy Materials and Solar Cells* **98**, 110-117 (2012).

109. Kumar, B., Gong, H., Vicknesh, S., Chua, S.J. & Tripathy, S. Luminescence properties of ZnO layers grown on Si-on-insulator substrates. *Applied Physics Letters* **89**, 141901 (2006).

110. Liu, H.F., Tripathy, S., Hu, G.X. & Gong, H. Surface optical phonon and A1(LO) in ZnO submicron crystals probed by Raman scattering: Effects of morphology and dielectric coating. *Journal of Applied Physics* **105**, 053507 (2009).

111. Insignares-Cuello, C. et al. Non-destructive assessment of ZnO:Al window layers in advanced Cu(In,Ga)Se2 photovoltaic technologies. *physica status solidi (a)* **212**, 56-60 (2015).

112. Pankove, J.I. Optical Processes in Semiconductors. *Dover Inc., New York*, 36 (1975).

113. Kumar, Y.B.K., Bhaskar, P.U., Babu, G.S. & Raja, V.S. Effect of copper salt and thiourea concentrations on the formation of Cu2ZnSnS4 thin films by spray pyrolysis. *physica status solidi (a)* **207**, 149-156 (2010).

114. Berg, D.M. et al. Discrimination and detection limits of secondary phases in Cu2ZnSnS4 using X-ray diffraction and Raman spectroscopy. *Thin Solid Films* **569**, 113-123 (2014).

115. Ishii, M., Shibata, K. & Nozaki, H. Anion Distributions and Phase Transitions in CuS1-xSex(x = 0-1) Studied by Raman Spectroscopy. *Journal of Solid State Chemistry* **105**, 504-511 (1993).

116. Fernandes, P.A., Salomé, P.M.P. & da Cunha, A.F. Study of polycrystalline Cu2ZnSnS4 films by Raman scattering. *Journal of Alloys and Compounds* **509**, 7600-7606 (2011).

117. González, B., Calvar, N., Gómez, E. & Domínguez, Á. Density, dynamic viscosity, and derived properties of binary mixtures of methanol or ethanol with water, ethyl acetate, and methyl acetate. *The Journal of Chemical Thermodynamics* **39**, 1578-1588 (2007).

118. www.surface-tension.de.

119. Nie, L., Liu, S., Chai, Y. & Yuan, R. Spray pyrolysis deposition and photoresponse of Cu2CdSnS4 thin films. *Journal of Analytical and Applied Pyrolysis* **112**, 363-368 (2015).

120. Bhosale, S.M. et al. Influence of growth temperatures on the properties of photoactive CZTS thin films using a spray pyrolysis technique. *Materials Letters* **129**, 153-155 (2014).

121. Malkeshkumar, P., Indrajit, M. & Abhijit, R. Study of the junction and carrier lifetime properties of a spray-deposited CZTS thin-film solar cell. *Semiconductor Science and Technology* **28**, 055001 (2013).

122. Valdés, M., Santoro, G. & Vázquez, M. Spray deposition of Cu2ZnSnS4 thin films. *Journal of Alloys and Compounds* **585**, 776-782 (2014).

123. Mousel, M. et al. HCl and Br2-MeOH etching of Cu2ZnSnSe4 polycrystalline absorbers. *Thin Solid Films* **535**, 83-87.

124.   Bouttemy, M. et al. Thinning of CIGS solar cells: Part I: Chemical processing in acidic bromine solutions. *Thin Solid Films* **519**, 7207-7211 (2011).

125.   Jehl, Z. et al. Thinning of CIGS solar cells: Part II: Cell characterizations. *Thin Solid Films* **519**, 7212-7215 (2011).

126.   Cha, J.-H. & Jung, D.-Y. CuGaS2 hollow spheres from Ga–CuS core–shell nanoparticles. *Ultrasonics Sonochemistry* **21**, 1194-1199 (2014).

127.   Vegard, L. Die Konstitution der Mischkristalle und die Raumfüllung der Atome. *Zeitschrift für Physik* **5**, 17-26 (1921).

128.   Belenguer, P., Ganciu, M., Guillot, P. & Nelis, T. Pulsed glow discharges for analytical applications. *Spectrochimica Acta Part B: Atomic Spectroscopy* **64**, 623-641 (2009).

129.   Fella, C.M. et al. Formation mechanism of Cu2ZnSnSe4 absorber layers during selenization of solution deposited metal precursors. *Journal of Alloys and Compounds* **567**, 102-106 (2013).

130.   Weber, A., Mainz, R. & Schock, H.W. On the Sn loss from thin films of the material system Cu–Zn–Sn–S in high vacuum. *Journal of Applied Physics* **107**, 013516 (2010).

131.   Gonzalez-Valls, I. & Lira-Cantu, M. Vertically-aligned nanostructures of ZnO for excitonic solar cells: a review. *Energy & Environmental Science* **2**, 19-34 (2009).

132.   Fei, T. et al. Flexible organic/inorganic hybrid solar cells based on conjugated polymer and ZnO nanorod array. *Semiconductor Science and Technology* **27**, 105005 (2012).

133.   Belaidi, A. et al. ZnO-nanorod arrays for solar cells with extremely thin sulfidic absorber. *Solar Energy Materials and Solar Cells* **93**, 1033-1036 (2009).

134.   Shin, B.-K. et al. Bottom-up grown ZnO nanorods for an antireflective moth-eye structure on CuInGaSe2 solar cells. *Solar Energy Materials and Solar Cells* **95**, 2650-2654 (2011).

135.   Chen, J. et al. Tapered aluminum-doped vertical zinc oxide nanorod arrays as light coupling layer for solar energy applications. *Solar Energy Materials and Solar Cells* **95**, 1437-1440 (2011).

136.   Ge, J., Chu, J., Jiang, J., Yan, Y. & Yang, P. Characteristics of In-Substituted CZTS Thin Film and Bifacial Solar Cell. *ACS Applied Materials & Interfaces* **6**, 21118-21130 (2014).

137.   Moon, S.H. et al. Printable, wide band-gap chalcopyrite thin films for power generating window applications. *Sci. Rep.* **4** (2014).

138.   Sarswat, P.K. & Free, M.L. Demonstration of a sol–gel synthesized bifacial CZTS photoelectrochemical cell. *physica status solidi (a)* **208**, 2861-2864 (2011).

139.   Ludwig, W. et al. Electrodeposition parameters for ZnO nanorod arrays for photovoltaic applications. *physica status solidi (a)* **210**, 1557-1563 (2013).

140.   Kavalakkatt, J. et al. Cu2ZnSn(S,Se)4 from CuxSnSy nanoparticle precursors on ZnO nanorod arrays. *Thin Solid Films* **535**, 380-383 (2013).